December 2015

Addressing Potential Risks and Challenges of CO2 Geologic Sequestration

Ethan Guyant
University of Wisconsin-Milwaukee

ADDRESSING POTENTIAL RISKS AND CHALLENGES OF CO_2 GEOLOGIC SEQUESTRATION

by

Ethan Guyant

A Thesis Submitted in

Partial Fulfillment of the

Requirements for the Degree of

Master of Science

in Geosciences

at

The University of Wisconsin-Milwaukee

December 2015

ABSTRACT

ADDRESSING POTENTIAL RISKS AND CHALLENGES OF CO_2 GEOLOGIC SEQUESTRATION

by

Ethan Guyant

The University of Wisconsin-Milwaukee, 2015
Under the Supervision of Professor Weon Shik Han

Carbon Capture and Geologic Storage is a viable technology to reduce the concentration of CO_2 emitted to the atmosphere, however there remains challenges and risks associated with implementing this technology. One of the challenges, and the focus of Chapter 2, is maintaining the injectivity of the reservoir throughout the entire injection period of a project. While potential risks include the pressurization of the reservoir and the leakage of CO_2 and/or brine out of the storage reservoir which is the focus of Chapter 3. A consequence of injecting dry-supercritical CO_2 is that it results in salt precipitation in the near well region of the reservoir which consequently reduces the permeability of this region; having adverse effects on the well injecitivity and pressure build-up. This work evaluated the salt precipitation, brine flux patterns, and pressure build-up for two well constructions, (1) a partially perforated (4 injection intervals) and (2) fully perforated throughout the storage reservoir. Both well designs showed non-localized salt precipitation in low-k formations and localized precipitation in high-k formations. It was also found that two distinct brine flux patterns occurred; under low-k conditions the brine flux was outward and parallel to CO_2 migration and precipitation became limited. However, under high-k conditions there developed back flow of the brine which amplified salt

precipitation. When this process occurred the permeability reduction was orders of magnitude greater than when non-localized salt precipitation occurred. This reduction resulted in pressure build-up in the near well region. Optimal injection conditions were found to be in reservoirs of mid-range permeability; which allowed for adequate pressure dissipation and minimized salt precipitation.

Once the injection is initiated there is a corresponding injection-induced pressurization of the reservoir which is typically monitored by an array of pressure sensors located within the storage reservoir as well as the surrounding formations. The monitoring of pressure build-up can provide explicit information on the reservoir security and integrity. Chapter 3 within this work evaluated pressurization of a CO_2 reservoir system in the presence of leakage pathways as well as exploring the effects of compartmentalization of the reservoir utilizing surrogate modeling techniques (e.g. Design of Experiments (DoE) and Response Surface Methodology (RSM)). Two simulation models were developed (1) an idealized scenario for the evaluation of multiple DoE methods, and (2) a complex scenario implementing the best performing DoE method to investigate pressurization of the reservoir system. The evaluation of scenario 1, determined that the Central Composite design would be implemented in the complex scenario. The complex scenario evaluated 5 uncertain factors: the permeabilities of the reservoir, seal, leakage pathway and fault, and the location of the pathway. A total of 36 response surface equations (RSEs) were developed for the complex scenario with an average R^2 of 0.94 and a NRMSE of 0.060. Sensitivity to the input factors were dynamic through space and time. At the earliest time the impact of the reservoir permeability was dominant, whereas the fault permeability became dominant for later times (>0.5 years). The RSEs were implemented in a Monte Carlo Analysis to analyze leakage and pressurization risks. At the earliest time the permeability of the leakage

pathway had a sufficiently high influence on the above-zone pressure allowing for adequate determination of leakage risk. At later times (>0.5 years) that fault permeability became dominate inhibiting the determination of leakage risk while allowing for sufficient determination of pressurization risk.

TABLE OF CONTENTS

ABSTRACT ii
LIST OF FIGURES vii
ACKNOWLEDGMENTS ix

Chapter 1 1

Chapter 2 6
2.1 Introduction 6
2.2 Study Area 8
2.2.1 Aquistore Pilot CO_2 Injection Project 8
2.2.2 Geological Description 8
2.2.2.1 Regional Geology of the Williston Basin 8
2.2.2.2 Site-Specific Geology at Aquistore Storage Site 10
2.3 Modeling Description 12
2.3.1 Numerical Simulator 12
2.3.2 Conceptual Model Description 14
2.3.3 Simulation Scenarios 17
2.4 Characteristics on Implementing Partially Perforated and Fully Perforated Well 18
2.4.1 Patterns of Near Well Salt Precipitation 18
2.4.2 Brine flux pattern and CO_2 migration 19
2.4.3 Reservoir permeability reduction 22
2.4.3.1 Influence of Reservoir Permeability on k/k_0 Reduction 22
2.4.3.2 Influence of injection rate on k/k_0 Reduction 24
2.4.4 Effects of Salt Precipitation on Pressure Build-Up 25
2.4.5 Salt Precipitation Configuration Sensitivities 27
2.4.5.1 Critical Porosity 27
2.4.5.2 Isotropic vs Anisotropic Conditions 29
2.5 Discussion and Conclusions 31

Chapter 3 37
3.1 Introduction 37
3.2 Background: Statistical Techniques 41
3.2.1 Design of Experiments (DoE) 41
3.2.2 Response Surface Methodology (RSM) 44
3.3 Methodology 45
3.3.1 Generalized Workflow 45
3.3.2 Statistical and Numerical Simulators 48
3.4 Idealized Scenario: Design Evaluation 49
3.4.1 Conceptual Model Description 49
3.4.2 Utilizing the Validation Dataset to Assess the RSE Fit 52
3.4.3 Assessment of RSE's Predictability via Test Dataset 55

3.4.4 Selection of Suitable DoE Design for Complex Geologic CO_2 Sequestration Simulations 57
3.5 Complex injection Scenario: Pressurization Evaluation 60
3.5.1 Conceptual Model Description 60
3.5.2 Description of the Central Composite Design (CCD) 61
3.5.3 Assessment of RSM Fit 62
3.5.4 Sensitivity Analysis 65
3.5.5 Uncertainty Analysis 68
3.5.5.1 T1: 0.05 Year Monitoring Time 69
3.5.5.2 T2: 0.5 Year Monitoring Time 71
3.5.5.3 T3: 5.0 Year Monitoring Time 72
3.5.6 Risk Assessment Associate with Leakage and Pressurization Due to Compartmentalization 73
3.6 Discussion and Conclusions 76

Chapter 4 83

Appendix A: Idealized Scenario Data 86

Appendix B: Complex Scenario Data 91

LIST OF FIGURES

Figure 1. Regional map of study area near Estevan in Saskatchewan, Canada. 9
Figure 2. Williston Basin stratigraphy and hydrostratigraphy 11
Figure 3. Permeability reduction conceptual diagram 14
Figure 4. Schematic view of the developed model domain 15
Figure 5. Near well salt precipitation configurations 18
Figure 6. Solid saturation, brine flux, and 0.3 CO2-saturation front 21
Figure 7. Reservoir permeability reduction and areal extent of precipitated salt 23
Figure 8. Pressure profile of injection and maximum salt saturation of near well region 26
Figure 9. Sensitivity of salt saturation, reservoir permeability, and pressure build-up to critical porosity values 28
Figure 10. Sensitivity of salt saturation and brine flux to assumed reservoir conditions 30
Figure 11. 3-factor DoE designs that were evaluated 43
Figure 12. A generalized workflow for experiment design and analysis (EDA). 46
Figure 13. Schematic diagrams of the two considered injection scenarios 49
Figure 14. Simulated ΔP vs. RSE-predicted ΔP 53
Figure 15. Comparison statistics considered for design evaluation 58
Figure 16. Visualization of the RSE fit at times T1, T2, and T3 and diagnostic statistics 64
Figure 17. Tornado diagram displaying the top 5 most influential factors 66
Figure 18. Monte Carlo simulation results for the above-zone region 70
Figure 19. Conditional and unconditional *cdf's* of leakage pathway and fault permeability with calculated conditional probabilities for the three risk levels 74

LIST OF TABLES

Table 1. Model parameters and transport parameters 16
Table 2. Three Factor Box-Behnken DoE table 41
Table 3. Model parameters and transport parameters 50
Table 4. DoE factors for the idealized and complex scenario 51
Table 5. Number of conducted simulation for the training, validate and test datasets for both the idealized and complex scenarios. 52
Table 6. Comparison statistics for the four-evaluated DoE designs 54
Table 7. Coded CCD design table used in the complex scenario 62

ACKNOWLEDGMENTS

First and foremost I express my greatest gratitude to my advisor professor Dr. Weon Shik Han for his encouragement and guidance throughout my graduate career, without which this work would not have been possible.

I would also like to thank my thesis committee members, Dr. Kue-Young Kim and Dr. Shangping Xu for their guidance and feedback throughout the development of this work.

I must extend a great level of appreciation to the NSF, the R&D Project on Environmental Management of Geologic CO_2 Storage offered by the Korea Environmental Industry & Technology Institute as well as the Advanced Opportunity Program Fellowship provided by the University of Wisconsin-Milwaukee, all of which help financially support the work conducted throughout my graduate career.

Finally, I must thank my family and closest friends who have had confidence in me and surrounded me with encouragement.

Chapter 1

Introduction

Historically human activity has influenced carbon dioxide (CO_2) concentration in the atmosphere dramatically, and the continuing energy demand expects to augment CO_2 emissions spurring global climate change throughout the 21st century [*Intergovernmental Panel on Climate Change*, 2005]. Emission of total anthropogenic greenhouse gas (GHG) has persistently increased between 1970 and 2010. From 2000 to 2010, in spite of a growing number of climate change mitigation polices, annual GHG emissions grew by 2.2%, per year on average, with approximately 78% of the total GHG emissions attributed to CO_2 emissions [*Pachauri and Meyers*, 2014]. In 2015, the atmospheric CO_2 concentration is expected to reach 400 parts per million, with this concentration representing an increase of approximately 45% since the industrial revolution [*Celia et al.*, 2015]. The increase in atmospheric CO_2 concentration is expected to continue if no corrective action is taken. The International Energy Agency (IEA) has projected that the energy demand will experience an increase of 35% by 2035, with 76% of the energy demand expected to be achieved from the burning of fossil fuels despite efforts to increase the use of renewable [*IEA*, 2013]. Of main concern, if current carbon emission rates persist, is how much and how fast the earth will warm; with the answer to both concerns being products of complex global feedback systems which are not yet fully understood. However, the potential consequences of warming include significant water-related impacts (e.g. rising sea levels, loss of ice cover, and extreme storms and droughts) [*Celia et al.*, 2015].

Discussions on the management and reduction of carbon emissions have been occurring for over a decade, however little large-scale actions have been implemented to significantly reduce the anthropogenic atmospheric carbon footprint. *Pacala and Socolow* [2004] were able to

recognize a number of existing technologies that have the potential to reduce carbon emissions; including: wind, solar, and natural gas, each substituting coal for heat and power generation; increased automotive efficiency, implementation of biofuels; and Carbon Capture and Storage for large stationary CO_2 sources [*Celia et al.*, 2015]. Of the identified technologies CCS is the only currently available technology that allows for the continued combustion of fossil fuels. Consequently, in order to satisfy the global energy demand while reducing the concentration of anthropogenic atmospheric CO_2, CCS equipped fossil fuel power generation facilities are expected to be a significant portion of new power generation [*Intergovernmental Panel on Climate Change*, 2005].

CCS is a process that involves all the technologies utilized in the capturing, separating, compressing, transporting, injecting, and long-term monitoring of injected anthropogenic CO_2. The CCS technologies have been implemented on a variety of scales across various geographic regions [*Litynski et al.*, 2008; *Michael et al.*, 2010]. These include projects ranging from industrial- to pilot-scale injections; with the oldest operation dating back to 1996 when the injection of 1 million tonnes (Mt) of CO_2 per year into the Utsira formation (Sleipner oil and gas field) began [*Korbøl and Kaddour*, 1995]. This project has been followed by many others across the world; including: the In Salah injection in Algeria (2004-2011), the Ketzin project in Germany (2008-2009), Snohvit gas project (2008) under the North Sea, the Weyburn-Midale project in Saskatchewan, Canada (2000), and the Decatur project in Illinois (2011-2015). Although each of the projects have been beneficial in furthering our understanding of CO_2 storage processes and potential consequences it should be noted that the joint annual injection rate of all currently operational projects is still less than the output from one large coal-fired power plant; highlighting the immense scale of the problem [*Celia et al.*, 2015].

The large-scale deployment of CCS technologies has been inhibited due to the fact there still remains significant barriers. *Celia et al.* [2015] identified two major barriers linked to CCS: (1) the high energy demand (i.e. high cost) associated with the capturing of CO_2 and (2) the execution of injecting large volumes of CO_2 into the subsurface and the potential unintended environmental impacts. The focus of this work is on the second barrier; which within itself has three main components. In order for a subsurface formation to be considered it must first meet three basic conditions: (1) the storage formation needs to have sufficient capacity to store the volume of CO_2 that's expected to be injected, (2) the storage formation must have sufficiently high permeability to receive the injected CO_2 at the rate supplied from the source, and (3) the storage formation must be able to isolate the injected CO_2 from overlying units, protected groundwater, soil, and/or the atmosphere [*Celia et al.*, 2015]. Of the three basic conditions this work is concerned with the second (i.e. injectivity of the reservoir) and the third (i.e. containment of the injected CO_2 volume)

The primary geologic media that are attractive to CCS are deep saline aquifers and depleted oil and gas reservoirs. These typically consist of sedimentary rocks which provide porosities and permeabilities that allow for sufficient injectivity. However, of the two, deep saline aquifers are more advantageous for large-scale injection projects as they are estimated to have significantly larger storage capacity [*Intergovernmental Panel on Climate Change*, 2005], and are thus the focus of Chapter 2 in this work. Chapter 2 addresses the injectivity of the storage reservoir by evaluating near well salt precipitation which can have adverse effects on the injectivity of the reservoir.

Another favorable attribute of deep saline aquifers is they can be found at depth within a greater sedimentary basin characterized by layer-type successions of high-permeability rocks

(i.e. sandstones and carbonates) topped by low-permeability rocks (i.e. shales, anhydrites, and salt beds) which work to inhibit the upward migration of the buoyant injected CO_2 volume. Prohibiting the upward migration of the injected CO_2 out of the storage reservoir is of main concern when addressing the containment condition of the storage reservoir. Chapter 3 within this work addresses this issue through the evaluation of the injection-induced pressure response within the reservoir as well as the surrounding formation in order to assess the likelihood of the presence of leakage pathways.

Chapter 1 References

Celia, M.A., Bachu, S., Nordbotten, J.M., and Bandilla, K.W. (2015), Status of CO2 storage in deep saline aquifers with emphasis on modeling approaches and practical simulations, *Water Resources Research*, *51*(The 50th Anniversary of Water Resources Research), doi:http://dx.doi.org/10.1002/2015WR017609.

IEA (2013), World Energy Outlook 2012*Rep.*, International Energy Agency.

Intergovernmental Panel on Climate Change, I. (2005), IPCC Special report on carbon dioxide capture and storage*Rep.*, Cambridge University Press, Cambridge.

Korbøl, R., and Kaddour, A. (1995), Sleipner vest CO_2 disposal - injection of removed CO_2 into the Utsira Formation, *Energy Conversion & Management*, *36*(6-9), 508-512, doi:http://dx.doi.org/10.1016/0196-8904(95)00055-I.

Litynski, J.T., Plasynski, S., Micllvried, H.G., Mahoney, C., and Srivastava, R.D. (2008), The United States Department of Energy's regional carbon sequestration partnerships program validation phase, *Environment International*, *34*(1), 127-138, doi:http://dx.doi.org/10.1016/j.envirt.2007.07.005.

Michael, K., Golab, A., Shulakova, V., Ennis-King, J., Allinson, G., Sharma, S., and Aiken, T. (2010), Geological storage of CO_2 in saline aquifers - A review of the experience from existing storage operations, *International Journal of Greenhouse Gas Control*, *4*, 659-667, doi:http://dx.doi.org/10.1016/j.ijggc.2009.12.011.

Pacala, S., and Socolow, R. (2004), Stabilization Wedges: Solving the Climate Problem for the Next 50 Years with Current Technologies, *Science*, *305*, 968-972, doi:http://dx.doi.org/10.1126/science.1100103.

Pachauri, R.K., and Meyers, L. (2014), Climate Change 2014: Synthesis Report*Rep.*, 155 pp, IPCC, Geneva, Switzerland.

Chapter 2

Salt Precipitation and CO_2/Brine Flow Distribution under Different Injection Well Completions

This chapter published as:

Guyant, E., Han, W.S., Kim, K.-Y., Park, M.-H., and Kim, B.-Y., (2015), Salt precipitation and CO_2/brine flow distribution under different injection well completions, *International Journal of Greenhouse Gas Control*, *37*, 299-310, doi:http://dx.doi/org/10.1016/j.ijggc.2015.03.020

2.1 Introduction

In order for CCS to be a successful mitigation process, well injectivity must remain sufficiently high in order to maintain high injection rates of CO_2 throughout the life of the CCS project. Previous experimental studies [*Bacci et al.*, 2011; *Burton et al.*, 2008; *Oh et al.*, 2013; *Peysson et al.*, 2014] as well as modeling studies [*Alkan et al.*, 2010; *Andre et al.*, 2007; *Kim et al.*, 2012; *Pruess and Müller*, 2009] have predicted that salt precipitation will occur when dry supercritical CO_2 ($scCO_2$) is injected into a brine-saturated core or saline aquifer. This salt precipitation can have adverse effects on well injectivity due to the significant reduction of the formation permeability adjacent to the injection well [*Giorgis et al.*, 2007]. *Oh et al.* [2013] conducted core-flooding experiments to investigate the impact of fractures on CO_2 transport, capillary pressure, and storage capacity. X-ray imaging techniques allowed for the observation of salt precipitation during the $scCO_2$-flooding test and revealed that CO_2 saturation at the inlet showed a progressive decrease in CO_2 saturation while the saturation increased throughout the rest of the core. The observed salt-precipitation during both laboratory and numerical experiments highlights the potential for pressure build-up and the decline of well injectivity in the field-scale CO_2 injection test. The role of the fluid dynamics responsible for this salt-precipitation in the field was investigated by *Pruess and Müller* [2009] who identified that at lower injection rates the

buoyancy force acting on the CO_2 plume as well as the role of capillary pressure becomes more prominent resulting in larger solid salt-saturation adjacent to the well. The similar trend was also observed by *Giorgis et al.* [2007] and *Kim et al.* [2012]. Here, *Giorgis et al.* [2007] arrived at similar conclusions that the salt-precipitation and the related reduction in formation permeability caused the blockage of the injection well and halted CO_2 injection. Interestingly, *Kim et al.* [2012] revealed two different salt-precipitation configurations defining the uniform and localized salt-precipitation, which were selectively developed dependent on the conditions of both injection rate and the permeability of storage formation; the localized salt-precipitation, which results in significant build-up of the bottom-hole pressure and deteriorates well injectivity, preferentially developed at high-permeability storage formation and under low injection rate scheme. These conditions can be met during pilot scale CCS projects where the injection rates can be relatively low and the storage formation tends to have high permeability.

The current study aims to investigate conditions for the localized salt-precipitation development and its adverse effects on the bottom-hole pressure by implementing the geologic formations and operating designs from the Aquistore project, located near Estevan, Canada. In the previous studies associated with the salt-precipitation, $scCO_2$ injection through a fully perforated well was primary concern [*Burton et al.*, 2008; *Han et al.*, 2013; *Kim et al.*, 2012; *Pruess and Müller*, 2009; *Zeidouni et al.*, 2009]. Nevertheless, a fully perforated well through the entire injection formation is frequently not an economically favorable option due to perforating cost and the occurrence of interbedded low permeability facies within the target formation. Due to this reason, for the Aquistore project, four injection zones with different lengths were perforated to improve $scCO_2$ injection within the designated high permeability zones. The goal of this study is

to investigate salt precipitation, brine flux patterns and pressure build-up for these two different well designs.

2.2 Study Area

2.2.1 Aquistore Pilot CO_2 Injection Project

The Aquistore CO_2 injection demonstration project was initiated and is led by the Petroleum Technology Research Centre and involves a consortium of industry, government, and research organizations. The Aquistore/Boundary Dam project aims to demonstrate the effectiveness of CO_2 capture, transportation, and storage and in doing so further support that CCS is a viable solution for the reduction of anthropogenic CO_2 emissions [*Whittaker and Worth*, 2011]. The project investigates the feasibility of capturing approximately 3,100 tonnes per day of CO_2 from SaskPower's Boundary Dam electrical generation facility located near Estevan in southern Saskatchewan, Canada (Figure 1). The Estevan area has economic and social ties to the power plant as well as the oil and gas industry (e.g., Weyburn field), and thus support for CCS is due to the view that this technology will prolong the economic viability of the Boundary Dam facility. Of the captured CO_2 amount, approximately 1,000 tonnes per day of CO_2 is planned to be transferred to SaskPower property approximately 3 km from the Boundary Dam Power Station and then will be stored in the basal units of the Williston Basin, which consists of the Winnipeg and Deadwood Formations at approximately 3,400 m depth.

2.2.2 Geological Description

2.2.2.1 Regional Geology of the Williston Basin

The Williston Basin is a large sedimentary basin composed of Phanerozoic sedimentary rocks overlying Precambrian crystalline rocks, which expands across portions of southwestern Manitoba, southern Saskatchewan, North and South Dakota, and eastern Montana and covers an

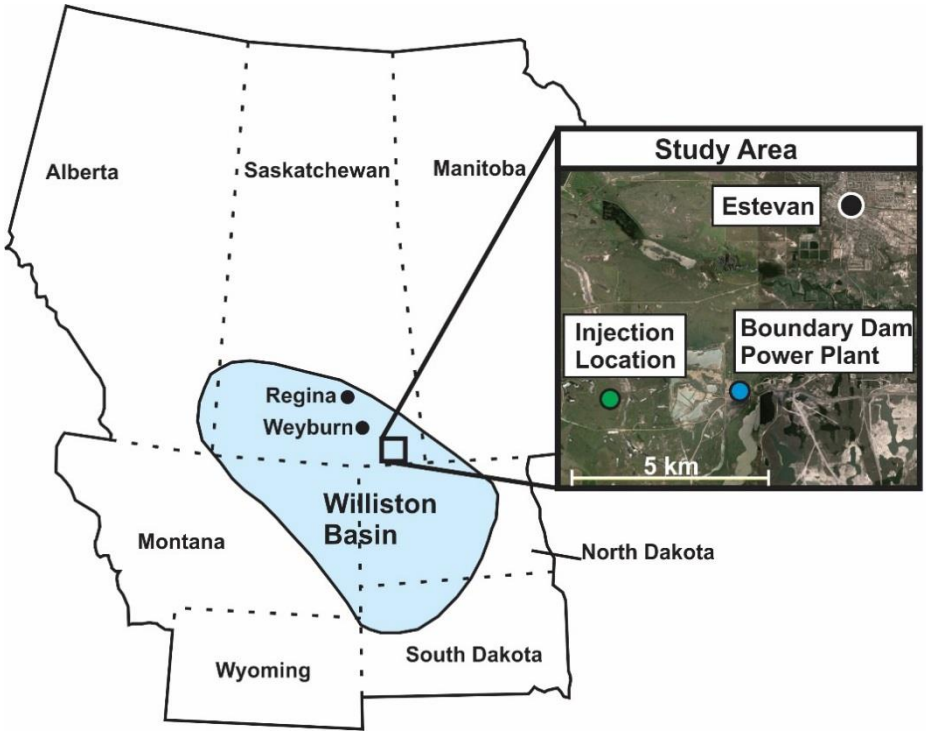

Figure 1. Regional map displaying the geographical location of the Williston Basin with the zoomed in panel displaying the location of the Aquistore injection site, Boundary Dam Power Plant and the town of Estevan in Saskatchewan, Canada.

area of 250,000 km^2 (Figure 1) [*Kent and Christopher,* 1994]. The basin has been characterized over the past 50-60 years due to its history of hydrocarbon exploration and, this has revealed that the basin has only a few major fault systems. Consequently, the lack of faults and history of hydrocarbon exploration within the basin makes it desirable for carbon sequestration activities [*Gorecki et al.,* 2009]. The fault information available suggest that major faults within the Williston Basin are susceptible to offsets of 15 m or less in the Ordovician portions of the stratigraphy and this offset decreases moving upward [*Houseworth*, 2011].

The base of the sedimentary basin is comprised of a Cambro-Ordovician aquifer system (Winnipeg and Deadwood Formations) that overlay Precambrian crystalline basement (Figure 2). The stratigraphic sequence above this Cambro-Ordovician system is made up of Middle

Ordovician-Mississippian carbonates and evaporates, including the 100 m thick Prairie Evaporite Formation. This sequence is overlain by the Bakken formation, a regional seal, which is overlain by Pennsylvanian-Quaternary units consisting of mainly shale and sandstone, which make up the remainder of the sequence [*Houseworth*, 2011]. The geologic units that overlie the Deadwood formation provide plentiful units that could act as a seal preventing upward migration of injected CO_2 and provide additional confidence in the success of long-term storage of anthropogenic CO_2.

2.2.2.2 Site-Specific Geology at Aquistore Storage Site

The major formations that overlie the Precambrian basement are the Deadwood formation and the Winnipeg Formation; these sediments were deposited in a marine to shallow-marine environment [*Sorensen et al.*, 2009]. The Deadwood formation is the bottom most unit of the basin and lays uncomformably on top of the Precambrain surface and is a predominately sandstone unit but also includes siltstones and mudstones (Figure 2). The sandstone within the Deadwood formation is medium to coarse grained, with cross-bedding and moderately cemented with silica. Specifically, the lower Deadwood formation consists of interbedded mudstones that are grey to green shales, transitioning upward to white, grey, green and red claystone and silty claystone. The depositional environment of the Deadwood formation is considered to be shallow epeiric sea with water depths no greater than 20 m [*Greggs and Hein*, 2000]. Above the Deadwood formation lies the Winnipeg formation which consists of sandstones and shales that were deposited under marine conditions in the Middle to Late Ordovician [*Ferguson et al.*, 2007]. The Winnipeg formation is comprised of two units; the lower unit is the Black Island member, a continuous, poorly consolidated, quartz-rich sandstone sheet [*Nicolas and Barchyn*, 2008]. Variations in the Black Island are seen in the lower part, which is medium grained and well sorted, and fines upward and becomes slightly muddy. The upper unit is the Icebox member, which is made up of mostly shale with some interbedded sandstone, and the Icebox member is thought to have good potential for

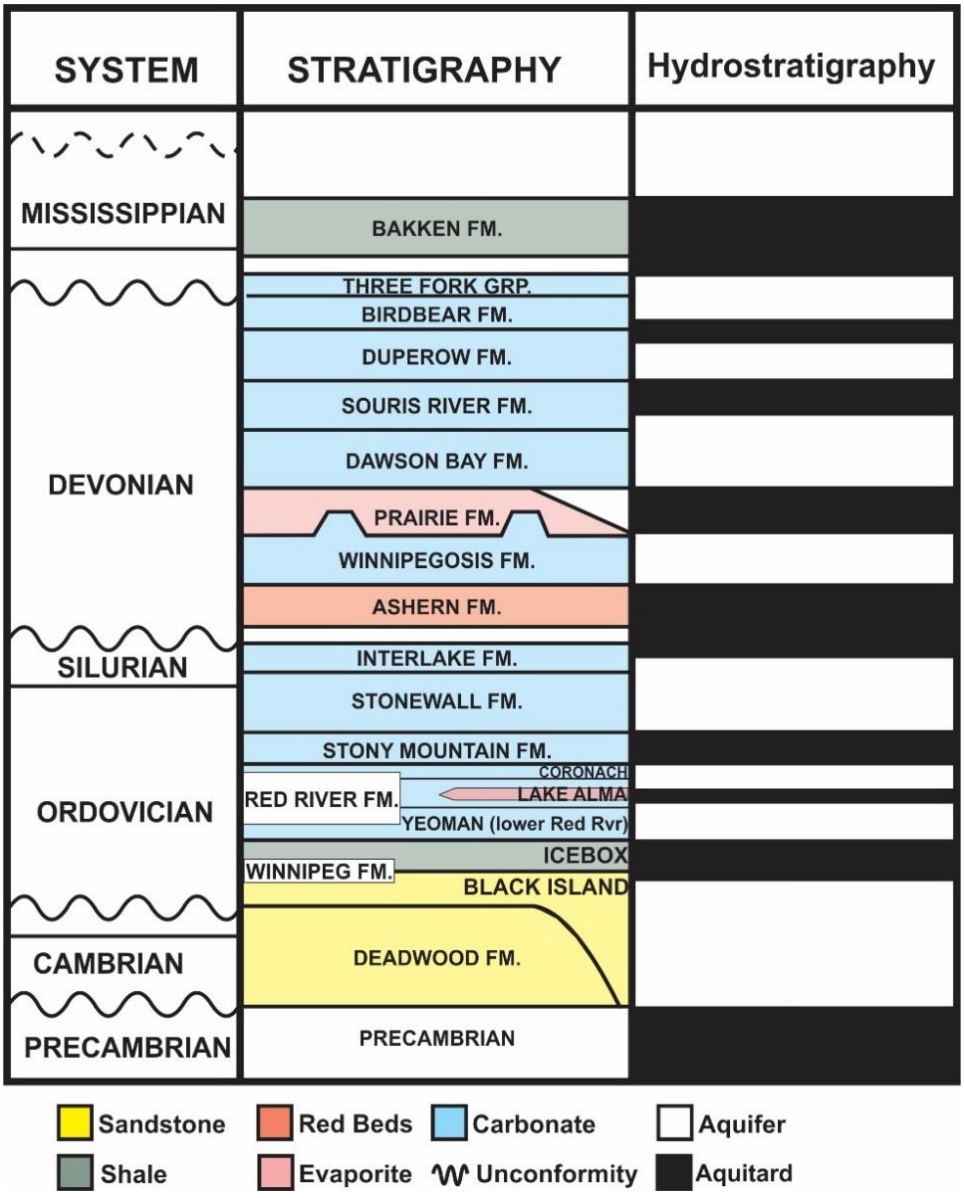

Figure 2. Williston Basin stratigraphy and hydrostratigraphy *Palombi and Rostron* [2006].

acting as a seal for the units below [*Nicolas and Barchyn*, 2008]. This is further supported by *Ferguson et al.* [2007] which indicated that the upper shale layer of the Winnipeg has been found to be an effective hydraulic barrier isolating the underlying formations.

2.3 Modeling Description

2.3.1 Numerical Simulator

Numerical simulations were conducted in order to evaluate the accumulation of salt precipitation and the related bottom-hole pressure build-up as well as CO_2 plume migration utilizing TOUGH2/ECO2N. TOUGH2 is a general-purpose numerical simulator developed for the analysis of multiphase, multicomponent fluids, and heat flow within porous and fractured media [*Pruess et al.*, 1999]. ECO2N is a fluid property module capable of predicting thermophysical properties of a water-rich phase (liquid), CO_2-rich phase (gas) and their mixture (H_2O-NaCl-CO_2) under suitable conditions ($10°C \leq T \leq 110°C$, $P \leq 60MPa$, and salinity up to full halite saturation) [*Pruess*, 2005]. Numerous previous studies associated with CO_2 sequestration processes have been conducted utilizing TOUGH2/ECO2N [*Alkan et al.*, 2010; *Doughty*, 2010; *Han et al.*, 2013; *Kim et al.*, 2012; *Strandli and Benson*, 2013; *Tambach et al.*, 2014; *Wainwright et al.*, 2013].

In the ECO2N fluid property module, the CO_2-rich phase considers sub- and supercritical CO_2 as a single non-wetting phase, which can be limiting in that there is no mass-transfer between liquid and gaseous CO_2. However, this limitation can have negligible effects in the current study because the main focus was on near well and storage reservoir conditions where both pressure and temperature are sufficiently high to maintain $scCO_2$. Pure CO_2 properties are obtained from tabular data calculated using the correlations developed by Altunin (1975) and vapor-saturated brine density is calculated using correlation developed by *Haas* [1976] with the correlations of *Andersen et al.* [1992] for the calculation of brine compressibility. Mutual solubilities of CO_2 and water for both the gas and brine phases are calculated by *Spycher and Pruess* [2003]. Finally, permeability reduction due to salt precipitation is calculated using a "tube-in-series" model following the equation [*Pruess et al.*, 1999; *Verma and Pruess*, 1988],

$$\frac{k}{k_0} = \theta^2 \frac{1-\Gamma+\Gamma\Big/\left(1-\dfrac{1/\Gamma}{1/\phi_r-1}\right)^2}{1-\Gamma+\Gamma\left[\theta\Big/\left(\theta+\left(1-\dfrac{1/\Gamma}{1/\phi_r-1}\right)-1\right)\right]^2} \qquad \text{(eq.1)}$$

Where,

$$\theta = \frac{1-S_s-\phi_r}{1-\phi_r} \qquad \text{(eq. 2)}$$

Here S_s is solid NaCl saturation representative of the fraction of pore space occupied by solid salt, ϕ_r is the fraction of original porosity ($\phi_r = \phi/\phi_0$) at which permeability is reduced to zero, and Γ is the fractional length of the pore bodies; ϕ_0, and k_0 are initial porosity and permeability, respectively, with k/k_0 representing the permeability reduction factor. *Verma and Pruess* [1988] observed that Γ had a relatively weak influence on permeability reduction, but ϕ_r had a significant effect on permeability reduction due to mineral precipitation. For this study, the values of ϕ_r and Γ were initially set to 0.8 as previous studies [*Alkan et al.*, 2010; *Kim et al.*, 2012; *Pruess and Müller*, 2009].

Modification of the formation permeability (k/k_0) due to salt precipitation is shown in Figure 3 for representative ϕ_r values of 0.75, 0.8, 0.85, and 0.9; these, ϕ_r were chosen in the sensitivity studies of section 3.5.1. Figure 3a displays the k/k_0 calculated from eq. 1 and eq. 2 for solid NaCl saturations ranging from 0 to 0.25; hereby, a ϕ_r of 0.9 would represent a storage reservoir whose

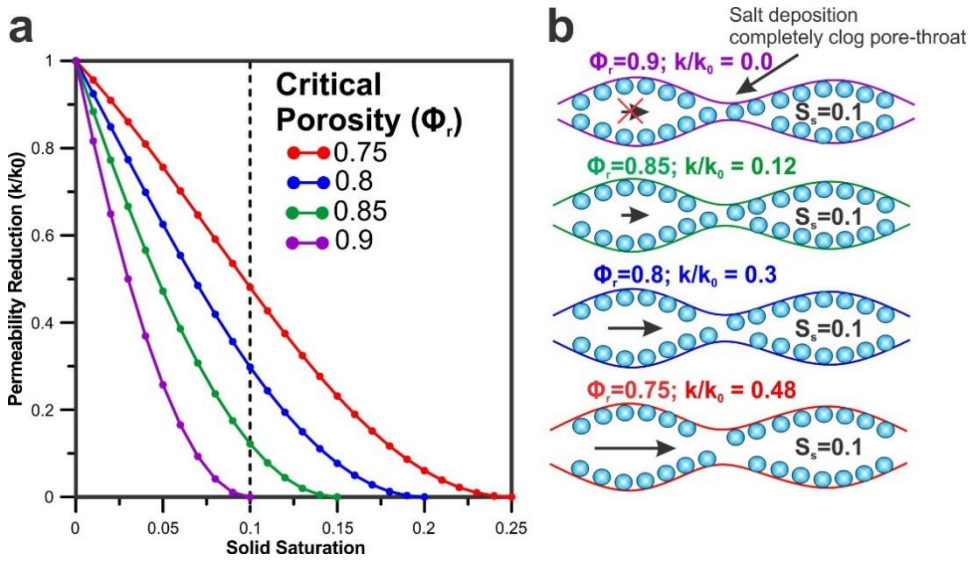

Figure 3. (a) Permeability reduction (k/k0) due to NaCl solid saturation which ranges from 0 to 0.25 for different ϕr values and (b) a schematic diagram of two pore bodies connected by a smaller radius pore throat with precipitated salts occurring uniformly along the pore wall at a solid NaCl saturation equal to 0.1 (dashed line on Figure 3a).

permeability is highly susceptible to permeability changes due to salt precipitation. The conceptual visualization of k/k_0 reduction at representative S_s=0.1 is shown at Fig 3b. A smaller radius pore throat connects two pore bodies with salt precipitation occurring uniformly along the pore wall.

2.3.2 Conceptual Model Description

A two-dimensional radially symmetric model was developed to simulate the injection of $scCO_2$ into a saline aquifer, delineating the CO_2 injection demonstration in the Aquistore project (Figure 4). The vertical thickness of the model was 470 m divided into 195 layers representing four geologic units such as the Deadwood Formation, the Winnipeg Formation (Black Island and Icebox member), and the Yeoman Formation (lower Red River Formation). The target reservoir was the Deadwood Formation with a thickness of 230 m, which is beneath the 40 m thick Black Island member; the basal sandstone unit in the Winnipeg Formation. Directly atop of Black Island member is the Icebox member, which is the 25 m thick shale formation primarily serving as the caprock.

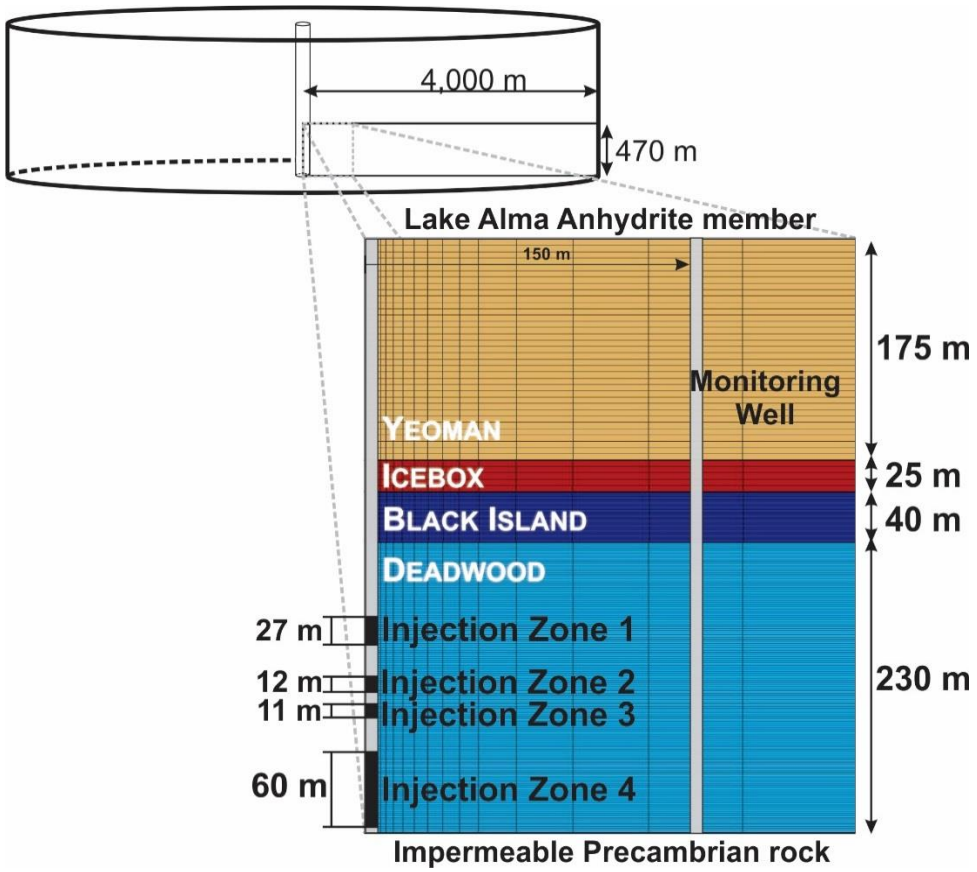

Figure 4. Schematic view of the radial symmetric model representing the Aquistore CO2 injection demonstration; the designated view is adjacent to the injection and monitoring well.

The radial extent of the model was 4,000 m with a grid discretization of 0.1 m selected at the injection well and logarithmically increased with increasing lateral distance from the injection well. The upper and lower boundaries of the model are no flow condition signifying that the model overlies impermeable Precambrian basement rock and underlies the Lake Alma unit, which contains an anhydrite member acting as a seal for the Yeoman (lower Red River Formation) [*Nicolas and Barchyn*, 2008]. The right lateral boundary represents an infinitely acting aquifer where the initial pressure and temperature conditions were maintained. The injection well at the left lateral boundary consisted of four injection intervals for the partially perforated well, from the

bottom most interval to the top interval; the lengths of the intervals are: 60m, 11m, 12m, and 27m respectively (Figure 4).

Pressure in the Deadwood formation at a depth of approximately 3,300m was estimated to be 34.3 MPa with an overall pressure gradient of 10.4 kPa/m. This was used to calculate a pressure of 30 MPa at the top boundary and 35 MPa at the bottom boundary of the model. Temperature ranged from 70 to 80°C from the top to the bottom boundary, and the salt mass fraction was set to 0.201 [*Weatherford Laboratories (Canada) Ltd.*, 2010]. Porosity was determined by a core analysis conducted by Weatherford Laboratories Ltd. The porosity of the Deadwood and Black Island units were set to 0.2, and the Icebox was 0.15.

Model Parameters	Values
Total number of elements	6825
Initial Conditions	
Pressure	30-35 MPa
Temperature	70-80 °C
Porosity	0.2
Boundary Conditions (right boundary)	Constant pressure and temperature
CO_2 injection well (left boundary)	0.1-1.0 million metric tons per year
Simulation Period	10 years
Transport Parameters	**Values**
Relative Permeability [van Genuchten-Mualem]	λ=0.7, S_{lr}=0.45, S_{lr}=0.995, S_{gr}=0.1
Brine	$S_* = (S_l - S_{lr})/(S_{ls} - S_{lr})$
	$k_r^{brine} = \sqrt{S_*}\left(1 - \left(1 - {S_*}^{1/\lambda}\right)^{\lambda}\right)^2$
Supercritical CO_2 phase	$S_\# = (S_l - S_{lr})/\left(1 - S_r - S_{gr}\right)$
	$k_r^{gas} = (1 - S_\#)^2(1 - {S_\#}^2)$
Capillary Pressure [van Genuchten]	λ=0.457, S_{lr}=0.0, $1/P_0$=5.1E^{-4}, S_{ls}=1.0
	$S^* = (S_l - S_{lr})/(S_{ls} - S_{lr})$
	$P_{CO2} = -P_0\left((S^*)^{-1/\lambda} - 1\right)^{1-\lambda}$

Table 1. Model parameters and transport parameters

For this study, the relative permeability and capillary pressure are modeled independently with the van Genuchten-Mualem and van Genuchten models [*van Genuchten,* 1980]. The relative

permeability is modeled by the equation presented in Table 1.Where k_r^{brine} is brine relative permeability, $k_r^{CO_2}$ is scCO$_2$-phase relative permeability, S_l , S_{lr}, and S_{gr} are the brine saturation, and residual saturations of brine and scCO$_2$, respectively, and λ is a fitting parameter of the van Genuchten-Mualem model. S_l, S_{lr}, and S_{gr} as well as λ were determined by curve matching to laboratory tests conducted by Weatherford Laboratories on core samples from the Deadwood Formation. Capillary pressure was included utilizing the van Genuchten function [*van Genuchten,* 1980] according to the equation presented in Table 1 and the parameters were determined and incorporated into the model with the same methods as relative permeability.

2.3.3 Simulation Scenarios

The effects of well completion on near-well salt precipitation, brine flux pattern, and pressure build-up was investigated through a series of simulations which consisted of two categories; 1) an injection well with partial perforation containing four injection intervals representing the Aquistore injection design and 2) a fully perforated well where CO_2 is injected throughout the entire thickness of the Deadwood Formation.

Hypothetical injection scenarios were conducted to evaluate the conditions under which accumulation of solid salt occurs and the associated effects that salt precipitation has on bottom-hole pressure build-up, and the brine flux pattern. The reservoir permeability was varied with different rates of injection because both formation permeability and injection rate are the most influential parameters on CO_2 plume migration, pressure build-up, and brine mobility [*Pruess and Müller*, 2009; *Wainwright et al.*, 2013], which governs the salt precipitation configuration [*Tambach et al.*, 2014]. Permeability ranged from 5.0×10^{-15} to 500×10^{-15} m^2 covering a full range of reservoir conditions. The range of the injection rates was assigned from 0.1 to 1.0 million metric tons per year (MMT/year) in order to model different scales of injection projects from pilot to

commercial scale. Later, a sensitivity analysis was conducted on the porosity-permeability relations for the flow channel parameter of critical porosity (ϕ_r). The entire simulation was conducted for a 10-year period with the first three years designated as the injection period followed by 7 years of monitoring.

2.4 Characteristics on Implementing Partially Perforated and Fully Perforated Well

2.4.1 Patterns of Near Well Salt Precipitation

Figure 5 presents the simulation results delineating the near well salt precipitation configurations for the two types of well completions, (1) a partially perforated well with four injection intervals (Figure 5a) and (2) a fully perforated well through the Deadwood formation (Figure 5b). For this comparison, two representative permeabilities (5.0×10^{-15} and 500×10^{-15} m^2) were chosen, and $scCO_2$ was injected at 0.25 MMT/year for the three-year period.

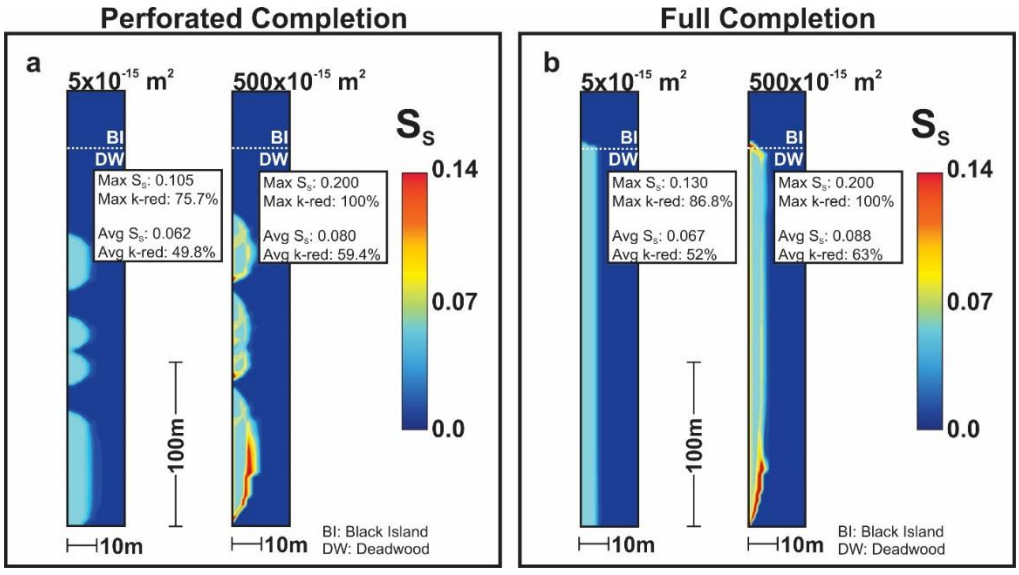

Figure 5. Near well salt precipitation configurations at the end of the injection period with reservoir permeability equal to 5×10-15 and 500×10-15 m2; (a) a partially perforated well with four injection intervals and (b) fully perforated well with an injection rate of 0.25 MMT/year.

For the partially perforated well of both the 5.0×10^{-15} and 500×10^{-15} m^2 cases, the precipitation of solid salt was focused only adjacent to the perforated intervals (Figure 5a). Because the injection of CO_2 was constrained to the designated intervals, the CO_2 plume advanced a greater distance, consequently developing a longer radial extent (approximately 10 m) of the salt precipitation. In contrast, for the fully perforated well, the solid salt precipitation was uniformly developed through the entire formation but with less radial extent (approximately 5 m) (Figure 5b). In both well-types, a comparison of the two permeability cases displayed two distinct types of salt precipitation similar to the observation by *Kim et al.* [2012]; non-localized salt precipitation developed at low-permeability (5.0×10^{-15} m^2) formation and localized salt precipitation at high permeability (500×10^{-15} m^2) formation.

In detail, the 5.0×10^{-15} m^2 case with the partially perforated well had a maximum solid saturation of 0.105 and an average value of 0.062 within the dry-out region (Figure 5a) calculated from all cells with $S_s>0$. For the 500×10^{-15} m^2 case, the severe accumulation of solid salt saturation completely clogged pores developing an impermeable zone at the bottom-most injection interval. Therefore, both the maximum and average solid saturation amplified to values of 0.2 and 0.08, respectively. The fully perforated well for both cases showed an increase in the average solid salt saturation when compared to the partially perforated well. From the partially to fully perforated well, the average salt saturation increased from 0.062 to 0.067 in low-k and from 0.080 to 0.088 in high-k reservoir.

2.4.2 Brine flux pattern and CO_2 migration

The different salt precipitation configurations are caused by the interplay between the buoyancy force acting on the CO_2 plume, the injection-induced pressure gradient, and the capillary backflow of the brine (Figs. 6a-d). For instance, at the low-permeability cases (5.0×10^{-15} m^2)

shown in Figs. 6a and 6c, the effects of the buoyancy force are limited leading to a reduced potential for vertical migration and an increased horizontal migration of the CO_2 plume. Consequently, the drawn 0.3 CO_2-saturation front extended approximately 50 m within the Deadwood formation with slight intrusion to the Black Island formation. The direction of brine flux was primarily outward from the dry-out zone to far-field parallel to the direction of the CO_2 plume, suggesting that the source of the precipitated solid salt is limited to the irreducible brine. In larger formation permeability (500×10^{-15} m^2) in Figs. 6b and 6d, larger buoyant condition induced farther movement of the CO_2 plume to the vertical direction. Hence, the drawn 0.3 CO_2-saturation front extended less than 25 m throughout the formation, but most CO_2 was accumulated beneath both the Black Island (BI) and Ice Box (IB) formations. At the tail of the CO_2 plume, the counter-flowing brine flux of 1.13×10^{-4} kg/(s-m^2) (partially perforated) and 8.0×10^{-5} kg/(s-m^2) (fully perforated) was concentrated, and acceleration of counter-flowing brine to the tail of CO_2 plume enhanced water evaporation, sustaining the precipitation process and amplifying the localized solid salt saturation (Figs. 6b and d).

The comparison of partially and fully perforated injection wells revealed the unique counter-flowing brine flux pattern specific to 500×10^{-15} m^2 formations (Figs. 6b and 6d). When the well is fully perforated, counter-flowing flux occurred at the tail of the CO_2 plume supplying brine to the bottom of the precipitation front as well as at the top (the interface of Black Island and Deadwood formations), resulting in only two solid salt accumulation regions (Figure 5b). In contrast, when the well is partially perforated, the salt precipitation predominantly occurred at both top and bottom of each individual perforated interval (Figure 5a) due to occurrence of the counter-flowing brine in between the perforated intervals (Figure 6b). For instance, the downward brine

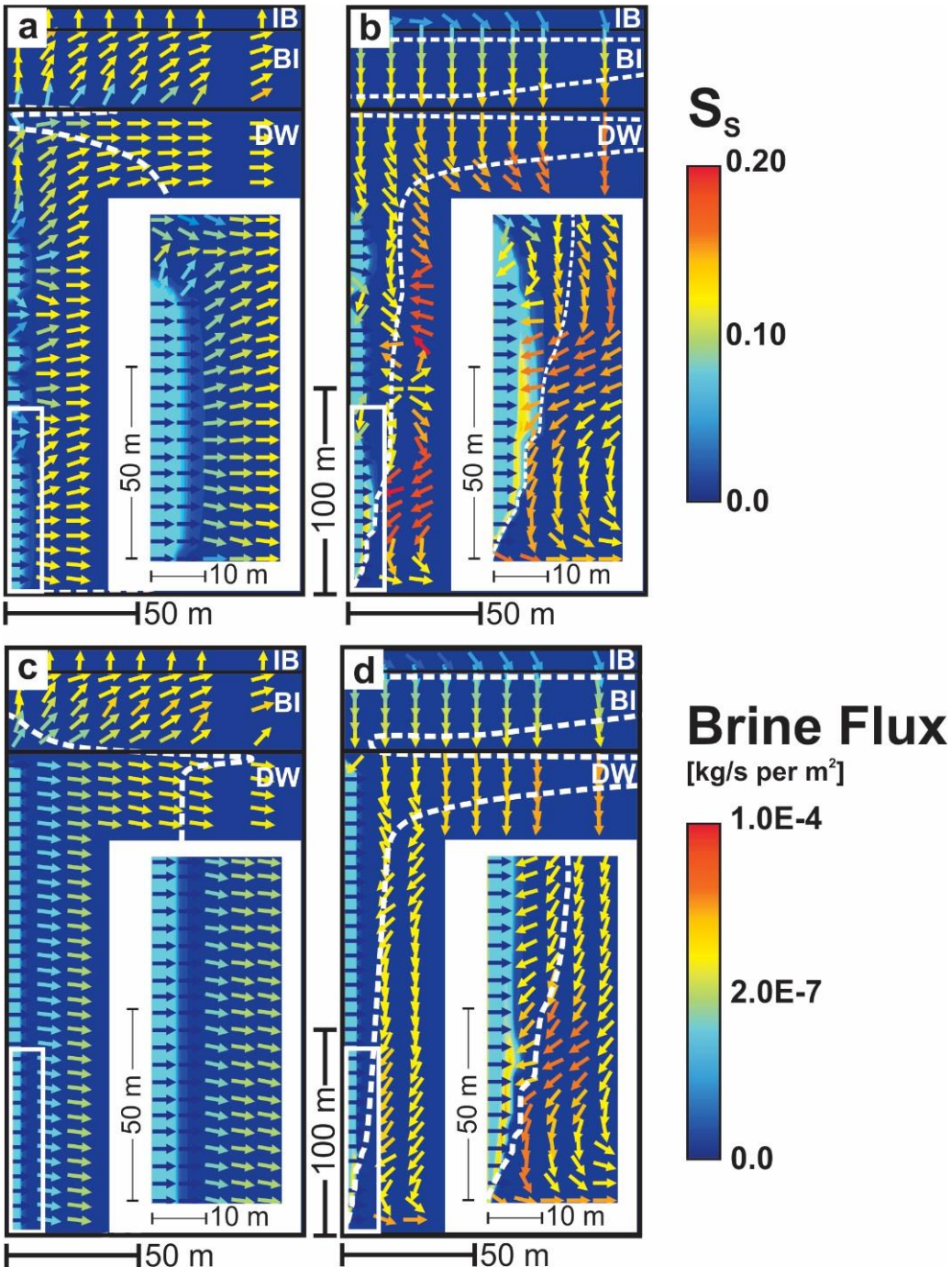

Figure 6. Solid saturation, brine flux (kg/(s-m2)), and 0.3 CO2-saturation front (dashed white line) for a partially perforated well with reservoir permeability equal to (a) 5.0×10-15 m2 (b) 500×10-15 m2, and a fully perforated well with reservoir permeability equal to (c) 5.0×10-15 m2 and (d) 500×10-15 m2 utilizing an injection rate of 0.25 MMT/year. The colors of brine flux vectors represent the magnitude.

flux from overlying intervals results in salt accumulations at the top of injection intervals 2, 3, and 4. In total, 8 regions of solid salt accumulations were developed in a partially perforated well due to the counter-flowing brine flux. Nonetheless it is evident that the most significant counter-flowing brine occurred at the base of the bottom-most perforated zone (Figure 6).

2.4.3 Reservoir permeability reduction

The reduction of reservoir permeability is an important consequence to consider while evaluating the effects of the $scCO_2$ injection. The reduction of permeability (k/k_0) is given by eq. 1, which indicates that k/k_0=1 is no reduction and 0 represents complete reduction. Figs. 7a and 7c show the sensitivity of k/k_0 for permeabilities 5.0×10^{-15}, 50×10^{-15}, 250×10^{-15}, and 500×10^{-15} m^2 with an injection rate of 0.25 MMT/year and Figs. 7b and 7d show the k/k_0 for injection rates 0.15, 0.25, 0.5, 1.0 MMT/year with a reservoir permeability value of 250×10^{-15} m^2.

2.4.3.1 Influence of Reservoir Permeability on k/k_0 Reduction

When the injection rate is 0.25 MMT/year in a partially perforated well, the median values of k/k_0 decrease with increasing permeability from 0.49 (51% reduction) for 5.0×10^{-15} m^2 to 0.45 (55% reduction) for 500×10^{-15} m^2 (Figure 7a). The greatest reduction of k/k_0 can be seen in the decreasing minimum and 10^{th} percentile values; the minimum k/k_0 are 0.24, 0.043, 2.2×10^{-7}, and 1.7×10^{-12} and the 10^{th} percentiles are 0.43, 0.38, 0.26, and 0.69×10^{-1} for 5.0×10^{-15}, 50×10^{-15}, 250×10^{-15}, and 500×10^{-15} m^2, respectively. The drastic decrease in both the minimum and 10^{th} percentiles of k/k_0 corresponds to the development of the localized salt precipitation at the well-bottom and potentially results in significant reduction of well injectivity. The area occupied by precipitated salt showed a decreasing trend with formation permeability (978.1, 964.1, 934.8, and 934.1 m^2 for 5.0×10^{-15}, 50×10^{-15}, 250×10^{-15}, and 500×10^{-15} m^2, respectively. In summary, injection

of CO_2 in the large permeability formation reduces the areal occupancy of salt precipitation but could induce the significant injectivity reduction.

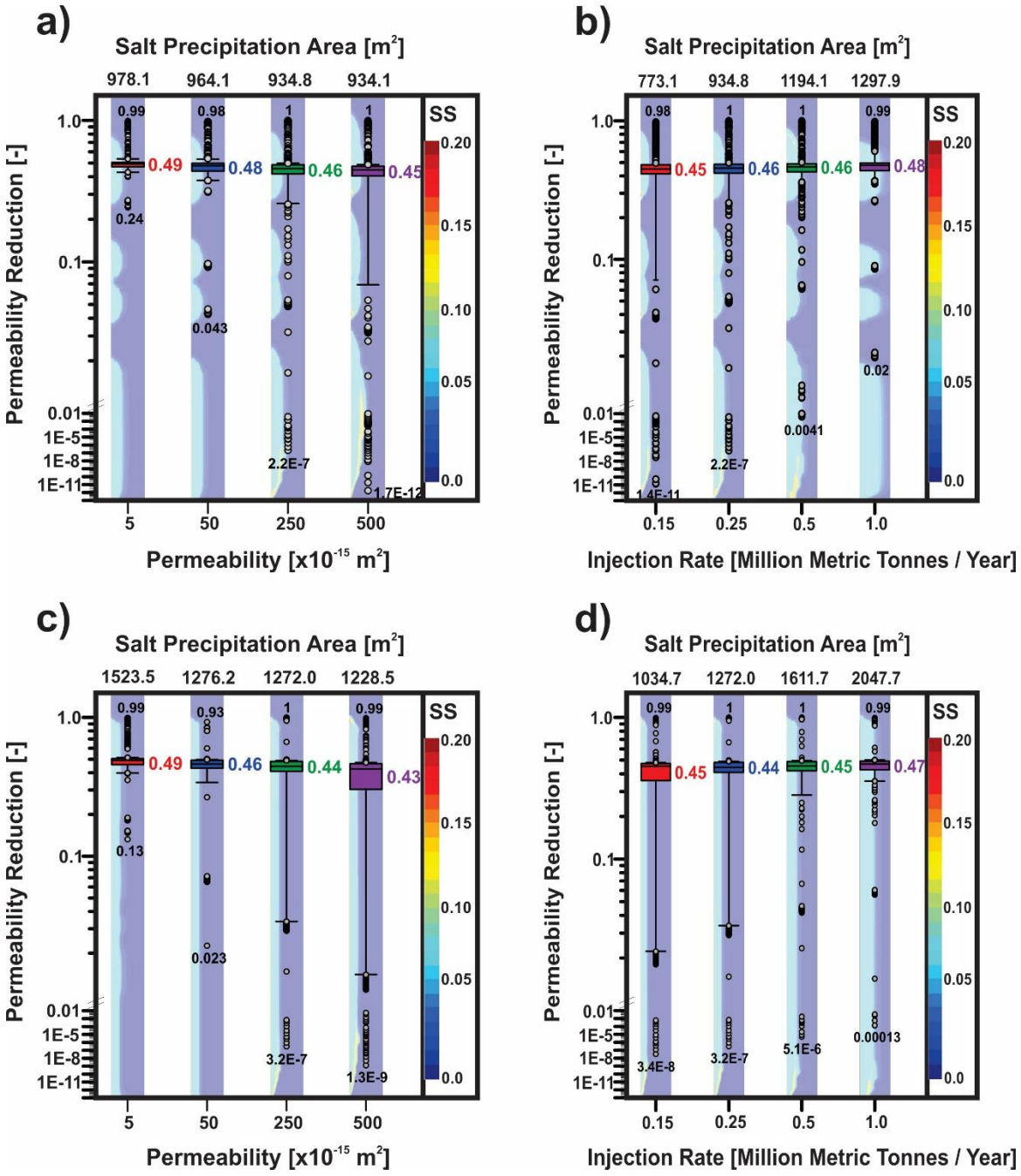

Figure 7. Reservoir permeability reduction (k/k0) (eq. 1) and area occupied by precipitated salt due to sensitivity of initial reservoir permeability of 5×10-15, 50×10-15, 250×10-15, and 500×10-15 m2 ((a) and (c)) and injection rate of 0.15, 0.25, 0.5 and 1 MMT/year ((b) and (d)) for two well completions.

For a fully perforated well, the similar trends were observed (Figure 7c). The median k/k_0 remained relatively consistent at different permeabilities, but the minimum and 10th percentile values increased significantly. Comparison between partially and fully perforated wells reveals several interesting features (Figure 7a vs 7c); k/k_0 reduction in large permeability formation (e.g. 500×10^{-15} m^2) was more severe for the partially perforated well, suggesting more potential for harmful injectivity reduction. However, a fully perforated well significantly enhanced the areal occupancy of precipitated salt, and related precipitation process occurred throughout the entire thickness of the Deadwood Formation.

2.4.3.2 Influence of injection rate on k/k_0 Reduction

The impact of injection rate was investigated by varying injection rates of 0.15, 0.25, 0.5, and 1.0 MMT/year at a reservoir permeability of 250×10^{-15} m^2 (Figs. 7b and 7d). Figure 7b displays the k/k_0 reduction for a partially perforated well. In this case, both median and minimum k/k_0 increased with increasing injection rate. Similar to the effects of permeability in Figure 7a, the minimum k/k_0 were drastically decreased with concurrent development of the localized salt, which occurred with the small injection rate (e.g., 0.15 MMT/year). The smaller injection rate enhanced the buoyance effect on CO_2 plume and accelerated the counter-flowing brine at the tail of CO_2 plume. Then, subsequent increase in the injection rate elevated the viscous force and prohibited the encroachment of brine back-flow. Therefore, with an injection rate of 1.0 MMT/year, no localized salt accumulation occurred (Figure 7b). The area of the reservoir occupied by the precipitated salt increased with higher injection rate (areas of 773.1, 934.8, 1194.1, and 1297.9 m^2 for injection rates of 0.15, 0.25, 0.5, and 1.0 MMT/year, respectively). The increase in the areal extent is attributed to higher injection rates where more $scCO_2$ is percolated into the porous reservoir causing the precipitation front to migrate further from the injection well.

The implementation of a fully perforated well resulted in similar trends as seen for the partially perforated well case. For the comparison between partially (Figure 7b) and fully perforated well (Figure 7d), ranges of median k/k_0 were almost equal in these two cases. In addition, the minimum k/k_0 experienced the same trend of increasing with increasing injection rate. Nevertheless, with a small injection rate (e.g., 0.15 MMT/year), the minimum k/k_0 ($=3.4\times10^{-8}$) for the fully perforated well was three orders of magnitude greater than ($=1.4\times10^{-11}$) for partially perforated well, suggesting that the fully perforated well has less potential for the injectivity reduction. In contrast, with a higher injection rate (e.g., 1 MMT/year), the fully perforated well showed more potential for severe injectivity reduction. Finally, the areal extent of salt precipitation becomes larger for the fully perforated well, suggesting that overall injectivity reduction would be larger at the fully perforated well.

2.4.4 Effects of Salt Precipitation on Pressure Build-Up

At field operations, the bottom-hole pressure typically controls the injection operations; if significant build-up of the bottom-hole pressure occurs, the injection will be halted to protect the well from failure. In Figure 8, the effect of solid salt precipitation on the pressure profile at the injection well was investigated at the end of the injection period. Pressure profiles were taken at the injection well, while solid saturation displays the maximum solid saturation that occurred at each measurement depth within 10 m of the injection well. The presented scenarios consist of reservoir permeability of 5.0×10^{-15}, 50×10^{-15}, 250×10^{-15}, and 500×10^{-15} m^2 at injection rate of 0.25 MMT/year.

For the partially perforated well (Figure 8a), the 5.0×10^{-15} m^2 case experienced the greatest average build-up in pressure (~ 5.6 MPa) with a maximum pressure increase of 7.9 MPa. No strong peaks were developed in the pressure profile. The pressure profile in 50×10^{-15} m^2 case displays the

similar pattern to 5.0×10^{-15} case with uniform decrease in pressure. Between 50×10^{-15}, 250×10^{-15} m^2 cases, the pressure profile transits from uniform to containing isolated peaks, and the accumulation of solid saturation begins to be highlighted. The greatest peaks (~12.5 and 5.5 MPa)

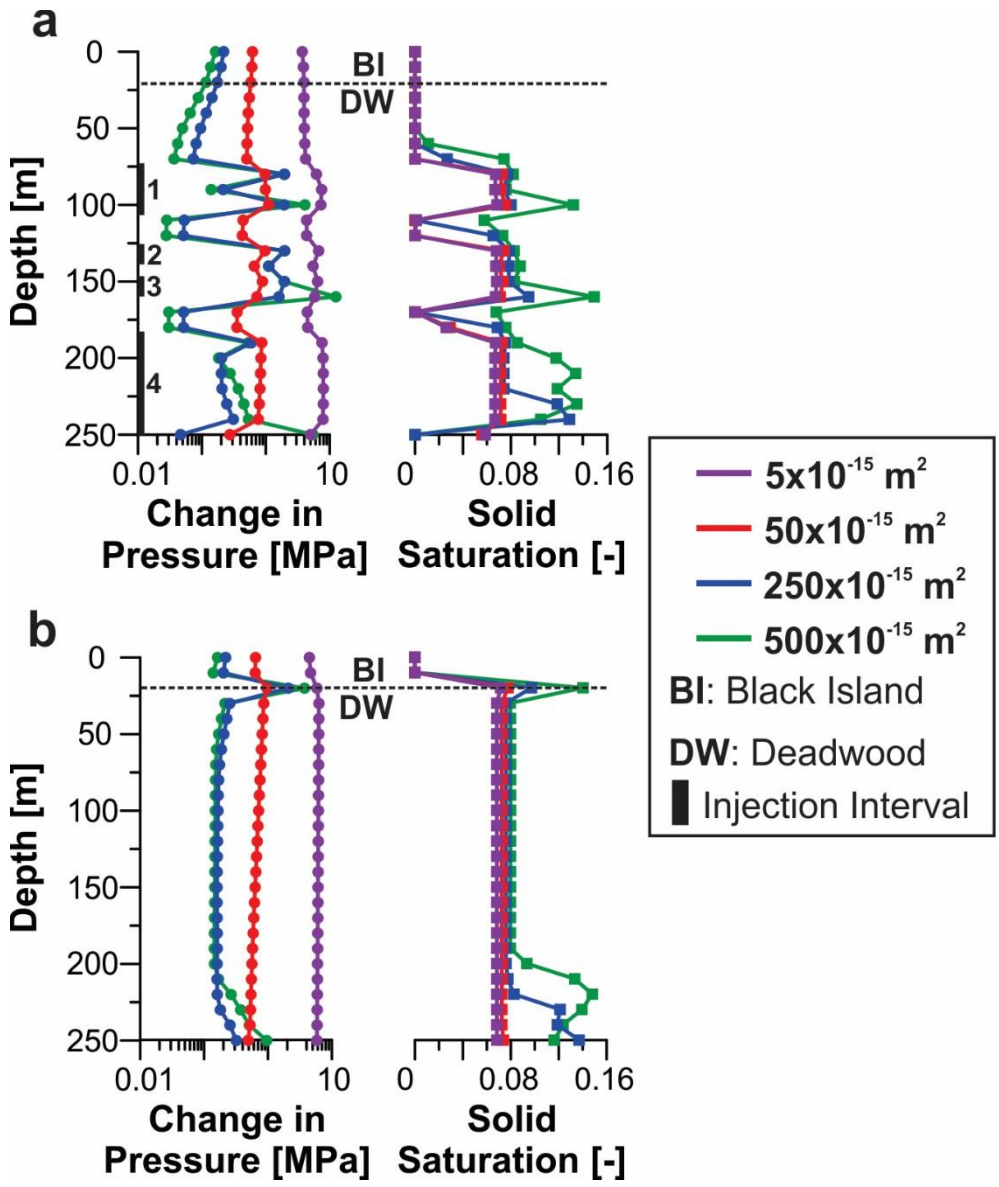

Figure 8. Change in pressure at the injection well and the maximum solid NaCl saturation within 10 m of the injection well throughout the 230 m thickness of the Deadwood formation; (a) partially perforated well and (b) a fully perforated well.

in the pressure profile appeared in the 500×10^{-15} m^2 case at the base of injection interval #3 (160 m) and the bottom of injection interval #4 (250 m), respectively.

In the fully perforated well (Figure 8b), solid salt saturation remains relatively stable throughout the thickness of the Deadwood Formation except for the top and bottom of the injection well, where for the highest permeability cases (250×10^{-15} and 500×10^{-15} m^2) the solid saturation is elevated. When non-localized salt precipitation occurred (5.0×10^{-15} and 50×10^{-15} m^2), the pressure profile increased by an average of 6.3 and 0.67 MPa, respectively, but remained linear with depth. However for the cases of 250×10^{-15} and 500×10^{-15} m^2, the pressure profile experienced peaks in the pressure profile. The greatest increase in pressure is seen in the 500×10^{-15} m^2 case where pressure increased by 3.6 and 0.81 MPa at the top and bottom of the injection well, respectively.

2.4.5 Salt Precipitation Configuration Sensitivities

2.4.5.1 Critical Porosity

The tube-in-series model that was implemented in this study is able to capture the converging-diverging nature of flow channels. With this model, the permeability of the reservoir can be reduced to zero at a given critical porosity (ϕ_r) if salt deposition on the pore walls completely clog the pore throat [*Verma and Pruess*, 1988] (Figure 3). However, ranges of ϕ_r in Eq. 1 and Eq. 2 are difficult to identify; ϕ_r is typically greater than 0.8 [*Vaughan*, 1985]. Although many previous studies implemented the tube-in-series model, all these studies simply adopted certain values [*Alkan et al.*, 2010; *Andre et al.*, 2014; *Bacci et al.*, 2011; *Kim et al.*, 2012]. Therefore, in this section, sensitivity studies associated with ϕ_r were conducted to investigate salt precipitation, permeability reduction, and pressure build-up (Figure 9).

Figure 9a-c presents the solid salt saturation, permeability, and pressure near the injection well, respectively, for an injection rate of 0.25 MMT/year and an initial reservoir permeability of

50×10^{-15} and 250×10^{-15} m^2. For 50×10^{-15} m^2, all of the simulations conducted experienced similar salt precipitation profiles with the only minor differences occurring near the well (less than 0.3 m) (Figure 9a). In contrast, localized salt precipitation appeared in the 250×10^{-15} m^2 case with the

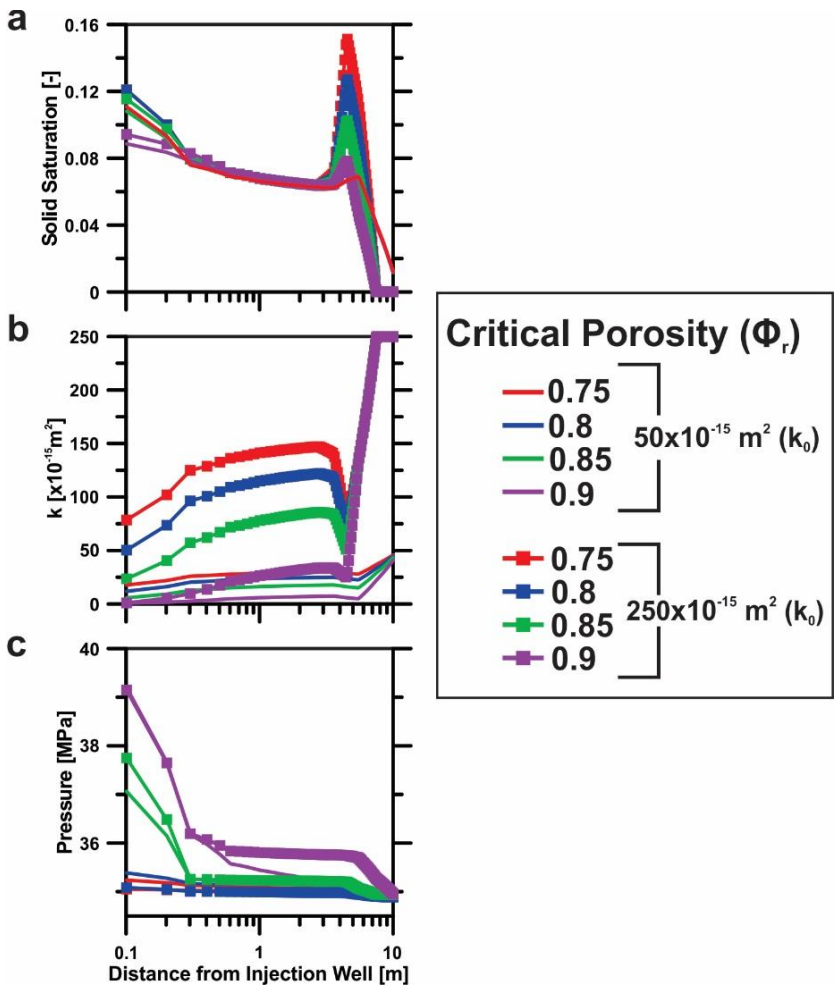

Figure 9. Sensitivity of (a) solid NaCl saturation, (b) reservoir permeability, and (c) pressure build-up to critical porosity values of 0.75 (red), 0.8 (blue), 0.85 (green), and 0.9 (purple) within 10 m of the injection well.

maximum salt saturation occurring approximately 5 m from the injection well. The highest saturation of salt precipitation occurred at (ϕ_r=) 0.75 and the lowest at (ϕ_r=) 0.9.

The main effect of ϕ_r values can be observed in the permeability profile in Figure 9b. It can be clearly seen that a ϕ_r value of 0.75 results in the least significant k reduction; in the 50×10^{-15}

mD case, an average permeability value through the 10-m horizon reduced to 32.4×10^{-15} m^2 (35.2 % reduction) and in 250×10^{-15} m^2 reduced to 170.3×10^{-15} m^2 (31.9%). In general, the most significant permeability reduction occurred at both the injection well and the location of the localized salt precipitate. Specific to the 50×10^{-15} case, with an increase in ϕ_r, the reservoir permeability was reduced systematically (Figure 9b) but the amount of precipitated solid salt remain consistent (Figure 9a); the average permeability though the horizon decreased to 28.1×10^{-15}, 22.3×10^{-15}, 13.9×10^{-15} m^2 for 0.8, 0.85 and 0.9, respectively. In contrast, when the localized peak occurs at 250×10^{-15} m^2, the solid salt saturation began to decrease with increasing ϕ_r. The higher critical porosity (ϕ_r=0.9) resulted in the lowest peak of solid salt (approx. 0.06 at 5m) (Figure 9a) but caused the highest permeability reduction (Figure 9b).

The reduction in permeability caused by different ϕ_r values has a direct effect on the pressure within the reservoir near the injection well. It can be seen in Figure 9c that when the ϕ_r was 0.9 the pressure in the reservoir increased the most. The difference in pressure response reveals the importance of understanding the sensitivity of the reservoir permeability to changes in porosity due to salt precipitation, and ϕ_r must be carefully identified.

2.4.5.2 Isotropic vs Anisotropic Conditions

To investigate the difference between isotropic and anisotropic conditions, additional simulations were conducted with a k_v/k_h ratio of 0.1 for a homogenous aquifer. The different salt precipitations, brine flux pattern, and 0.3 CO_2 saturation front are visualized in Figure 10 for an injection rate of 0.25 MMT/year and a horizontal permeability of 250×10^{-15} m^2. Figs. 10a and 10b display the results of anisotropic and isotropic conditions, respectively. Under anisotropic conditions, the vertical flow of the buoyant CO_2 becomes limited leading to the greater horizontal extend of the plume >30 m except for in the very base of the Deadwood Formation. While when

the reservoir is assumed isotropic, the CO_2 plume migrates vertically with a reduced horizontal extent (<30 m) near the injection intervals.

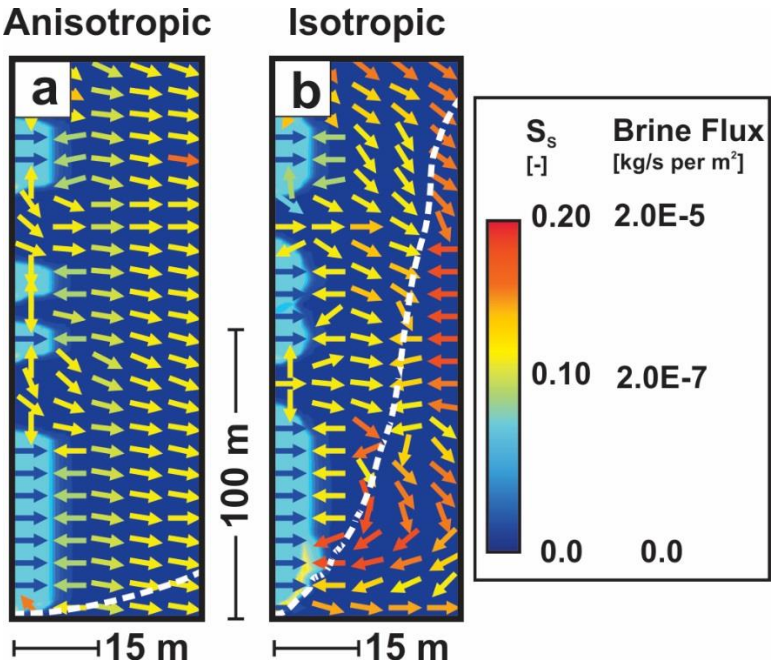

Figure 10. Solid NaCl saturation and brine flux (kg/(s-m2)) for a reservoir with a horizontal permeability of 250x10-15 m2 and injection rate of 0.25 MMT/year; (a) an anisotropic (kv/kh = 0.1) and (b) isotropic (=1). The colors of brine flux vectors represent the magnitude.

The difference in CO_2 plume migration leads to different brine flux patterns near the injection intervals. In the anisotropic case the brine flux becomes very uniform with the brine displaced away from the precipitation front. Counter-flowing brine only occurred at the base of the Deadwood formation as well as between the injection intervals near the injection well (Figure 10a). However for the isotropic case (Figure 10b); the enhanced vertical migration of the CO_2 induces back-flow of the brine near the tail end of the plume, resulting in localized salt precipitation at the base of the bottom-most injection interval. These series of simulations display the importance that the assumed k_v/k_h value can have on the evaluation of salt precipitation that occurs due to CO_2 injection. While the two case shown in Figure 10 can be thought of as two end-

members of the anisotropic/isotropic continuum, it is clear that an isotropic assumption can over-estimate the solid saturation near the injection well, and that a k_v/k_h ratio of 0.1 could potentially under-estimate the solid saturation. It is likely that under real field conditions the actual precipitation profile could range between these two cases and is likely to be affected by both horizontal and vertical changes.

2.5 Discussion and Conclusions

Through the series of simulations, the optimal injection scenario was determined considering two well types; fully and partially perforated wells. Two main factors were taken into account an economical factor as well as confidence of the success of the injection project (e.g., less degree of injectivity reduction and pressure build-up). The operation of an injection well is controlled by the build-up of bottom-hole pressure; if significant pressure builds up in the injection well, the injection activity must be ceased to prevent the potential well failure. Therefore, in this study, pressure profiles within the injection well were examined in order to determine which scenario is the least likely to encounter injectivity problems.

Low-k formations prohibit the effective dissipation of the pressure to the far field, resulting in significant pressure build-up within the storage reservoir (Figure 8). For instance, the pressure build-up for the 5.0×10^{-15} m^2 case was approximately 5.6 MPa and 5.9 MPa for a partially and fully perforated well, respectively, and decreased to 1.2 MPa and 0.35 MPa in the 500×10^{-15} m^2 case. A comparison of the two higher permeability cases (250×10^{-15} and 500×10^{-15} m^2) reveal that the 250×10^{-15} m^2 case did not experience as much strong accumulation of salt compared to the 500×10^{-15} m^2 case near the injection well (Figure 8). Due to less salt precipitation for 250×10^{-15} m^2, the maximum pressure build-up was only 1.98 MPa, which is significantly less than 12.5 MPa for 500×10^{-15} m^2 partially perforated well. Based on the pressure build-up near the injection well,

it can be concluded that a mid-range permeability (50×10^{-15} to 250×10^{-15} m^2) reservoir minimizes salt accumulation and allows for adequate pressure dissipation and therefore would be the optimal storage formation for CO_2 injection. Furthermore, the partially perforated well with 4 injection intervals (total perforated length equal to 120m) would be more economically practical than a fully perforated well through the 230 m thickness of the Deadwood formation.

Through a series of hypothetical injection scenarios, two salt precipitation profiles were observed; (1) characterized by non-localized salt precipitation and (2) characterized by localized salt precipitation. When a partially perforated well was implemented, the salt precipitation showed a greater radial extent but was limited to only adjacent to the injection intervals (Figure 5) In contrast, a fully perforated well induced development of salt precipitation throughout the target formation with constrained radial extent.

Low-k formations limit the effect of the buoyancy force acting on the plume resulting in limited vertical migration of CO_2. Under these conditions, the direction of brine flux was outward from the dry-out zone to the far field, limiting the source of salt to the irreducible brine (Figs. 6a and 6c). However, when reservoir permeability was increased, the buoyant migration of CO_2 amplified which in return accelerated counter-flowing brine to the tail of the CO_2 plume sustaining the precipitation process (Figs. 6b and 6d). Unique brine flux patterns for the partially and fully perforated well developed when significant vertical migration of the plume occurred. With a fully perforated well, brine flux toward the dry-out zone appeared at the top and bottom of the precipitation front causing two salt accumulation regions to occur. However, for the partially perforated well, areas of localized salt accumulation expanded because counter-flowing brine fluxes were concentrated at both the top and bottom of each injection interval resulting in eight accumulation regions to develop.

Significant permeability reduction of the reservoir occurred for both well completion with the onset of localized salt precipitation. The greatest *k* reductions occurred in high-k reservoirs under low injection rate conditions (Figure 7). For a given injection rate, the permeability reduction was more severe for a partially perforated well due to the occurrence of localized salt precipitation in multiple areas. Additionally, higher injection rates elevated the viscous force limiting the amount of counter-flowing brine causing less reduction in permeability. Under high injection rate conditions (e.g., 1 MMT/year), a fully perforated well displayed greater permeability reduction and in return had a higher potential for injectivity loss. However, with low injection rates (e.g., 0.15 MMT/year), a partially perforated well developed multiple zones of localized salt and thus exhibited a greater permeability reduction than the fully perforated well.

Additional simulations were conducted to evaluate the effects that critical porosity and k_v/k_h ratio had a salt precipitation, CO_2 plume migration, pressure build-up, and brine flux patterns. The lowest critical porosity value (0.75) resulted in the greatest amount of solid salt saturation, but experienced the least amount of permeability reduction and pressure build-up. Comparing anisotropic ($k_v/k_h = 0.1$) and isotropic results revealed two very different CO_2 plume migration, brine flux pattern, and salt precipitation. It was revealed that an isotropic reservoir assumption has the potential to over-estimate solid saturation, while $k_v/k_h = 0.1$ could very well under-estimate solid saturation, and it is likely that real field conditions would fall between the two results.

Chapter 2 References

Alkan, H., Cinar, Y., and Ulker, E.B. (2010), Impact of capillary pressure, salinity, and in situ conditions on CO_2 injection into saline aquifer, *Transport in Porous Media*, *93*(3), 381-399, doi:http://dx.doi.org/10.1007/s11242-010-9541-8.

Andersen, G., Probst, A., Murray, L., and Butler, S. (1992), An accurate PVT model for geothermal fluids as represented by H_20-CO_2-NaCl mixtures, paper presented at Seventeenth Workshop on Geothermal Reservoir Engineering, Stanford University, Stanford, California.

Andre, L., Audigane, P., Azaroual, M., and Menjoz, A. (2007), Numerical modeling of fluid-rock chemical interactions at the supercritical CO_2-liquid interface during CO_2 injection into a carbonate reservoir, *Energy Conversion & Management*, *48*(6), 1782-1797, doi:http://dx.doi.org/10.1016/j.enconman.2007.01.006.

Andre, L., Peysson, Y., and Azaroual, M. (2014), Well injectivity during CO_2 storage operations in deep saline aquifers - Part 2: Numerical simulations of drying, salt deposit mechanisms and role of capillary forces, *International Journal of Greenhouse Gas Control*, *22*, 301-312, doi:http://dx.doi.org/10.1016/j.ijggc.2013.10.030.

Bacci, G., Korre, A., and Durucan, S. (2011), An experimental and numerical investigation into the impact of dissolution/precipitation mechanisms on CO_2 injectivity in the wellbore and far field regions, *International Journal of Greenhouse Gas Control*, *5*, 579-588, doi:http://dx.doi.org/10.1016/j.ijggc.2010.05.007.

Burton, M., Kumar, N., and Bryant, S.L. (2008), Time-Dependent injectivity during CO_2 storage in aquifers, in *SPE Symposium on Improved Oil Recovery*, edited, Society of Potroleum Engineers, Tulsa, Oklahoma, USA, doi:http://dx.doi.org/10.2118/113937-MS.

Doughty, C. (2010), Investigation of CO_2 plume behavior for a large-scale pilot test of geolgoic carbon storage in a saline formation, *Transport in Porous Media*, *82*(1), 49-76, doi:10.1007/s11242-009-9396-z.

Ferguson, G.A.G., Betcher, R.N., and Grasby, S.E. (2007), Hydrogeology of the Winnipeg Formation in Manitoba, Canada, *Hydrogeology Journal*, *15*(3), 573-587, doi:http://dx.doi.org/10.1007/s10040-006-0130-4.

Giorgis, T., Carpita, M., and Battistelli, A. (2007), 2D modeling of salt precipitation during the injection of dry CO_2 in depleted gas reservoir, *Energy Conversion & Management*, *48*(6), 1816-1826, doi:http://dx.doi.org/10.1016/j.enconman.2007.01.012.

Gorecki, C.D., Sorensen, J.A., Steadman, E., and Harju, J.A. (2009), CO_2 storage risk minimization through systematic identification and assessment of faults: A Williston Basin case study, *Energy Procedia*, *1*(1), 2887-2894, doi:http://dx.doi.org/10.1016/j.egypro.2009.02.063.

Greggs, D.H., and Hein, F.J. (2000), The sedimentology and structure of the lower Paleozoic Deadwood Formation of Saskatchewan*Rep.*, Saskatchewan Geological Survey Sask. Energy Mines.

Haas, J.L. (1976), Physical properties of the coexisting phases and thermochemical properties of the H_2O component in boiling NaCl solutions, edited, Geological Survey Bulletin 1421-A, Washington.

Han, W.S., Kim, K.-Y., Park, E., McPherson, B.J., Lee, S.-Y., and Park, M.-H. (2013), Modeling of spatiotemporal thermal response to CO_2 injection in saline formations: interpretation for monitoring, *Transport in Porous Media*, *93*(3), 381-399, doi:10.1007/s11242-012-9957-4.

Houseworth, J.E. (2011), Leakage risk assessment for a potential CO_2 storage project in Saskatchewan, Canada, *LBNL Paper LBNL-4915E*.

Kent, D.M., and Christopher, J.E. (1994), Geological history of the Williston Basin and Sweetgrass Arch, in *Geological Atlas of the Western Canada Sedimentary Basin*, edited, pp. 421-430, Canadian Society of Petroleum Geologists.

Kim, K.-Y., Han, W.S., Oh, J., Kim, T., and Kim, J.-C. (2012), Characteristics of salt-precipitation and the associated pressure build-up during CO_2 storage in saline aquifers, *Transport in Porous Media*, *92*, 397-418, doi:10.1007/s11242-011-9909-4.

Nicolas, M.P.B., and Barchyn, D. (2008), Williston Basin Project (Targeted Geoscience Initiative II): Summary report on paleozoic stratigraphy, mapping and hydrocarbon assessment, southwestern Manitoba*Rep.*, Technology, Energy and Mines, Manitoba Geological Survey, Winnipeg, Manitoba.

Oh, J., Kim, K.-Y., Han, W.S., Kim, T., Kim, J.-C., and Park, E. (2013), Experimental and numerical study on supercritical CO_2/brine transport in a fractured rock: Implications on mass transfer, capillary pressure and storage capacity, *Advance in Water Resources*, *63*, 442-453, doi:dx.doi.org/10.1016/j.advwatres.2013.03.007.

Palombi, D., and Rostron, B. (2006), Regional Hydrochemistry of Lower Paleozoic Aquifers in the Northern Portion of the Williston Basin, Saskatchewan Manitoba, in *Saskatchewan and Northern Plains Oil & Gas Symposium*, edited, pp. 201-209, Saskatchewan Geolgoical Society.

Peysson, Y., Andre, L., and Azaroual, M. (2014), Well injectivity during CO_2 storage operations in deep saline aquifers - Part 1: Experimental investigation of drying effects, salt precipitation and capillary forces, *International Journal of Greenhouse Gas Control*, *22*, 291-300, doi:http://dx.doi.org/10.1016/j.ijggc.2013.10.031.

Pruess, K. (2005), ECO2N: A TOUGH2 fluid property module for mixtures of Water, NaCl, and CO_2*Rep.*, Lawrence Berkeley National Laboratory.

Pruess, K., and Müller, N. (2009), Formation dry-out from CO_2 injection into saline aquifers, *Water Resources Research*, *45*(3), doi:http://dx.doi.org/10.1029/2008WR007101.

Pruess, K., Oldenburg, C., and Moridis, G. (1999), TOUGH2 User's guide, version 2.0*Rep.*, Lawrence Berkeley national Laboratory.

Sorensen, J.A., Bailey, T.P., Smith, S.A., Gorecki, C.D., Fischer, D.W., Peck, W.D., Steadman, E.N., and Harju, J.A. (2009), CO_2 storage capacity estimates for stacked brine-saturated formations in the North Dakota portionof the Williston Basin, *Energy Procedia*, *1*(1), 2833-2840, doi:http://dx.doi.org/10.1016/j.egypro.2009.02.056.

Spycher, N., and Pruess, K. (2003), CO_2-H_2O mixtures in the geological sequestration of CO_2 I. Assessment and calculation of mutual solubilities from 12 to 100°C and up to 600 bar, *Geochimica et Cosmochimica Acta*, *67*(16), 3015-3031, doi:http://dx.doi.org/10.1016/S0016-7037(03)00273-4.

Strandli, C.W., and Benson, S.M. (2013), Identifying diagnostics for reservoir structure and CO_2 plume migration from multilevel pressure measurements, *Water Resources Research* *49*(6), 3462-3475, doi:http://dx.doi.org/10.1002/wrcr.20285.

Tambach, T.J., Loeve, D., Hofstee, C., Plug, W.-J., and Maas, J.G. (2014), Effects of CO_2 injection on brine flow and salt precipitation after field production, *Transport in Porous Media*, doi:http://dx.doi.org/10.1007/s11242-014-0283-x.

van Genuchten, M.T. (1980), A closed-form equation for predicting the hydraulic conductivity of unsaturated soils, *Soil Science Society of America*, *44*, 892-898, doi:10.2136/sssaj1980.03615995004400050002x.

Vaughan, P.J. (1985), Analysis of permeability reduction during flow of heated, aqueous fluid through Westerly Granite, paper presented at International Symposium on Coupled Processes Affecting the Performance of a Nuclear Waste Repository, Berkeley, California, September 18-20.

Verma, A., and Pruess, K. (1988), Thermohydrologic conditions and silica redistribution near high-level nuclear wastes emplaced in saturated geological formations, *J. Geophys. Res.*, *93*((B2)), 1159-1173, doi:http://dx.doi.org/10.1029/JB093iB02p01159.

Wainwright, H.M., Finsterle, S., Zhou, Q., and Birkholzer, J.T. (2013), Modeling the performance of large-scale CO_2 storage systems: A comparison of different sensitivity analysis methods, *International Journal of Greenhouse Gas Control*, *17*, 189-205, doi:10.1016/j.ijggc.2013.05.007.

Weatherford Laboratories (Canada) Ltd. (2010), Petroleum Technology Research Centre Deadwood Formation Well: 03-08-017-19 W2M CO_2 sequestration study, edited, Weatherford Laboratories.

Whittaker, S., and Worth, K. (2011), Aquistore: A fully integrated demonstration of the capture, transportation and geologic storage of CO_2, *Energy Procedia*, *4*, 5607-5614, doi:http://dx.doi.org/10.1016/j.egypro.2011.02.550.

Zeidouni, M., Pooladi-Darvish, M., and Keith, D. (2009), Analytical solution to evaluate salt precipitation during CO_2 injection in saline aquifers, *International Journal of Greenhouse Gas Control*, *3*, 600-611, doi:http://dx.doi.org/10.1016/j.ijggc.2009.04.004.

Chapter 3

Leakage and Pressurization Risk Assessment of CO_2 Reservoirs: A surrogate modeling approach

This chapter submitted to *Water Resources Research* as:

Guyant, E., Han, W.S., Kim, K.-Y., Park, E., and Han, K., (2015), Leakage and pressuization risk assessment of CO_2 reservoirs: A surrogate modeling approach, *Water Resources Research*

3.1 Introduction

Pressurization and pressure propagation within the storage system is a critical consequence of CO_2 injection activity and has been the focus of a wide array of previous studies [*Ashraf*, 2014; *Benisch and Bauer*, 2013; *Birkholzer et al.*, 2009; *Cavanagh and Wildgust*, 2011; *Chabora and Benson*, 2008; *Jung et al.*, 2013; *Meckel et al.*, 2013; *Zeidouni and Pooladi-Darvish*, 2012]. The subject of these previous studies are heavily focused on furthering our understanding of the possible consequences of pressurization as well as the factors influencing pressure propagation being dominantly driven by numerical analysis. Specifically, *Birkholzer et al.* [2009] identified that the area of elevated pressure is significantly larger than that of the CO_2 plume, consequently allowing for brine leakage out of the reservoir over a much larger area than the size of CO_2 plume. The ability to detect these leakages (CO_2 and/or formation brine) becomes a key component of risk assessment and management associated with CCS [*IPCC*, 2005]. However, extensive data acquisition for field-scale CO_2 deployment can become unrealistic due to cost constraints [*Friedmann et al.*, 2003], and the number of wellbores within the storage reservoir must be limited as they can pose a significant leakage risk [*Hu et al.*, 2012; *LeNeveu*, 2011; *Meckel et al.*, 2013]. The combination of the above two factors can result in utilizing transport simulation models, which are developed to study the pressurization of the reservoir system where

subsurface features and properties may not be well understood, leading to high uncertainty of the model input parameters.

For effective evaluation of the system in the context of risk assessment, it is advantageous to evaluate these transport simulations over a range of values that are presented by the uncertainties of the model input parameters. The risk assessment can require exhaustive simulations when the goal is to evaluate the occurrence of very low probability but high risk events, which can become impractical for computationally expensive simulations. An alternative is to instead utilize a simplified analytical model. However, *Rutqvist et al.* [2007] showed that analytical approaches can lead to over- or under-estimations of maximal sustainable injection pressure and concluded that a numerical analysis resulted in more accurate estimations. Similarly, *Rohmer and Bouc* [2010] arrived at consistent conclusions while evaluating the shear slip failure criterion of a cohesionless fault.

An alternative and intermediate solution to overcome the challenges associated with computationally expensive simulations in risk assessment described above is the utilization of Experimental Design and Analysis (EDA). The main objective of the EDA is to develop a training dataset typically implementing Design of Experiments (DoE) and utilizing it in the fitting of a statistical surrogate model (e.g. Response Surface Methodology (RSM)). The Response Surface Equation (RSE) developed is an analytic function that approximates the reservoir simulator, and with adequate verification, the RSE or surrogate model can be used for conducting a Monte-Carlo (MC) analysis inexpensively. This method has been applied throughout a variety of simulation modeling literature. Specific to reservoir engineering, it has been applied to history matching [*Gupta et al.*, 2008], uncertainty analysis [*Friedmann et al.*, 2003; *Li and Zhang*, 2014; *Rohmer and Bouc*, 2010; *Sun et al.*, 2013], sensitivity analysis

[*Bauman and deo*, 2011; *White et al.*, 2001] and quantifying risk and likelihood of failure [*Wriedt et al.*, 2014].

There exist a wide variety of EDA methods, which include various DoE designs used to generate training datasets as well as the method used to develop the surrogate model (e.g. kriging, neural networks, and least squares). DoE designs have been broken down into two subgroups: classical and modern designs [*Giunta et al.*, 2003]. Of the classical designs, the most common are two- and three-level designs each with a unique purpose. The two-level designs (e.g. Plackett-Burman, Fractional-Factorial) vary the input parameters between the two extreme values of its assigned range and are more geared toward screening the input parameters for model reduction and sensitivity studies. Three-level designs (e.g. Box-Behnken, Central Composite) vary the input parameters between the two extreme values and the midpoint, and are more suited for developing surrogate models which aim to predict the output responses. Modern designs (e.g. Latin Hypercube) differ in that they do not require replicate points, which can be beneficial when applied to a deterministic simulation model. Designs such as the Latin hypercube also differ from classical designs in that given n number of points in the training dataset results in n number of levels for each factor. Although the two categories differ in many aspects, they share a common objective of maximizing information gained on the system while minimizing the required number of experiments or simulations. Each specific design whether classical or modern has a unique set of pros and cons which must be evaluated in the context of the study objectives in order to select the appropriate method [*Can and Heavey*, 2011; *Giunta et al.*, 2003; *Yeten et al.*, 2005].

As above mentioned, there are multiple methods for fitting an approximating response function to the training dataset. Evaluation of these fitting methods has been conducted by

researchers across various fields [*Clarke et al.*, 2004; *Kleijnen*, 2005; *Schuetter et al.*, 2014; *Schultz et al.*, 2006; *Simpson et al.*, 2001; *Yeten et al.*, 2005]. Specific to reservoir engineering, *Schuetter et al.* [2014] evaluated nine input parameters in order to approximate three responses from a reservoir simulator using six surrogate models. In that study, a Box-Behnken paired with a quadratic RSE performed the best for predicting average pressure and total storage efficiency while a Maximum Latin Hypercube with a quadratic RSE was best suited for predicting the CO_2 plume radius. *Yeten et al.* [2005] also revealed that quadratic polynomial RSEs were comparable to more complex fitting methods in terms of regressional statistics, estimation accuracy, and capability to estimate the effect of parameters on the output response. Similarly, *Peng and Gupta* [2004] found that kriging methods did not develop better surrogate models when compared to a polynomial regression for quantifying hydrocarbon in-place probability distribution curves.

The current study utilized DoE and RSM to evaluate CO_2 injection-induced pressurization of a reservoir system in the presence of leakage pathways as well as exploring the effects of compartmentalization due to an adjacent fault system. Since a number of previously mentioned researchers utilizing DoE and RSM have found that a second-order polynomial performed adequately well, this study also adopted this method. However, the selection of DoE method has not received the same amount of attention, and few studies have compared multiple designs. For these reasons, the first stage of this work evaluated the performance of the multiple DoE designs for application to geologic CO_2 sequestration by using an idealized injection scenario. Following the design evaluation, the second stage consists of a complex injection scenario implementing the best performing design to investigate pressurization of the reservoir system.

3.2 Background: Statistical Techniques

3.2.1 Design of Experiments (DoE)

In order to utilize DoE, prior knowledge of the system must be obtained in order to identify any number of factors (model input parameters) that could possibly impact the response(s) (model output(s)) of interest. Once factors have successfully been identified, appropriate ranges of real factor values must be assigned to each. The real factor values are then coded with a discrete value of -1 for the lower limit, 0 attributed to the midpoint value, and +1 for the upper limit of the range. These coded values are then used in the development of a DoE table (i.e. Table 2).

Simulation Number	**X_1**	**X_2**	**X_3**
1	-1	-1	0
2	-1	+1	0
3	+1	-1	0
4	+1	+1	0
5	0	-1	-1
6	0	-1	+1
7	0	+1	-1
8	0	+1	+1
9	-1	0	-1
10	+1	0	-1
11	-1	0	+1
12	+1	0	+1
13	**0**	**0**	**0**

Table 2. Three Factor Box-Behnken DoE table where +/- 1 represent the upper and lower bounds of the individual factor's range and 0 represents the midpoint between the two bounds. The bold 0's of Row 13 represent any preferred number of center point replicates.

Each row of the DoE table consists of a unique combination of the discrete values representing a single simulation, which will be referred to here after as a design point. Table 2 presents a 3-factor example of a Box-Behnken DoE table. For performing each simulation prescribed in the

DoE table, the discrete values are replaced with the real factor values. Finally, the resulting response (output) from the simulation is recorded. Once all simulations have been conducted, collection of the training dataset is complete.

There are a wide variety of DoE designs requiring careful evaluation in order to select a design suited for the objectives of the study. The most basic designs are full-factorial designs where the number of design points is a function of the number of factors as well as the number of levels for each factor. For example, the most common design among the full-factorial designs is a 3^k-factorial design where there are 3 levels (i.e. -1, 0, +1) for *k* number of factors, which evaluates main, quadratic, and interaction effects of the system. Despite the efficiency of evaluating the system using the full-factorial design, the required number of simulations increases exponentially with the number of factors and can lead to an unrealistic amount of simulations. To alleviate this burden, multiple DoE designs have been developed which were specifically configured to reduce the number of design points.

In this work, four different DoE designs were evaluated: Definitive Screening, Box-Behnken, Central-Composite, and Latin-Hypercube (Figure 11). Generic examples of the four designs are delineated for *k* (=3) number of factors. The Definitive Screening Design (DSD) was introduced by *Jones and Nachtsheim* [2011], and is a relatively small design, which requires $2k+1$ simulations; *k* number of fold over pairs and an overall center-point (Figure 11a). However to maintain orthogonality for odd values of *k* requires an additional two simulations [*Jones and Nachtsheim*, 2011]. The Box-Behnken Design (BBD) is shown in Figure 1b [*Box and Behnken*, 1960]. For *k*=3, the BBD pairs together two design factors in a 2^2-factorial while the 3^{rd}-factor remains fixed at its center-point, with the same methodology applying for *k*= 4 and 5 [*Myers et al.*, 2009]. The BBD is advantageous when it is beneficial to have the three levels (-1, 0, +1) of

the design evenly spaced. A drawback to the BBD is that it consists of edge points of the cube (k=3) and there are no points on the corners (extreme values) (Figure 11b) resulting in higher uncertainties in the prediction of the response at these extreme values.

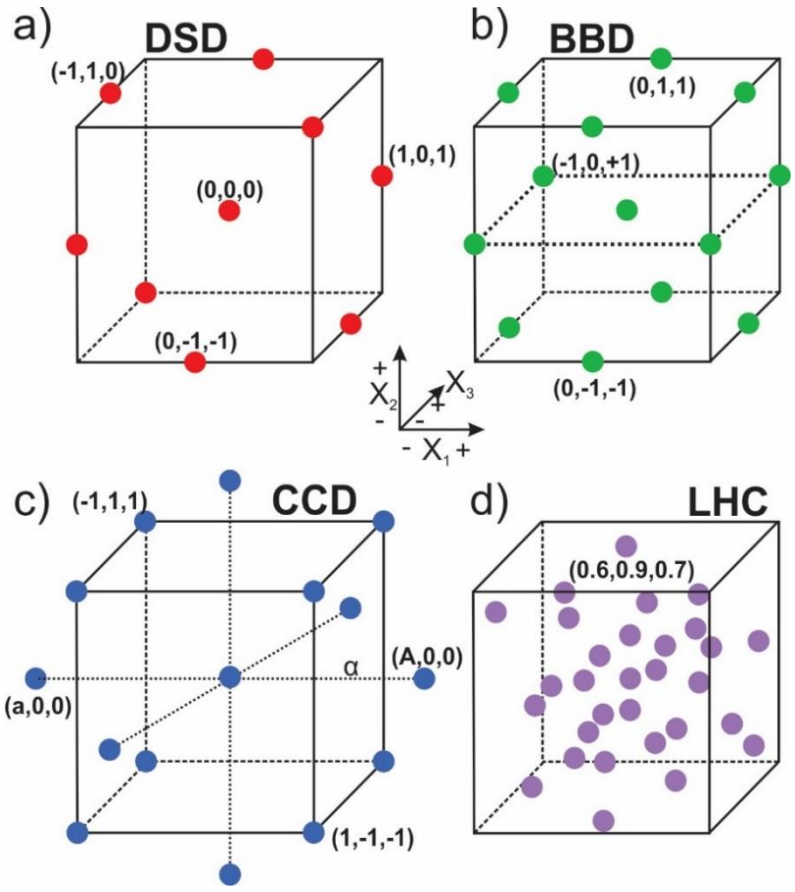

Figure 11. 3-factor DoE designs; (a) Definitive Screening design (DSD), (b) Box-Behnken design (BBD), (c) Central Composite design (CCD), and d) Latin Hypercube (LHC) design. Displayed on each of the figures are sets of DoE factor levels that correspond with the design point. Figure 11b is a visual representation of the BBD table listed in Table 2. For the CCD in Figure 11c, alpha (α) is the axial distance, which in the current study equals 1 (face-centered) where a=-1 and A=+1.

A Central Composite Design (CCD) is the most widely used response surface design [*Box and Wilson*, 1951] (Figure 11c). The CCD consists of a 2-level factorial design combined with 2k axial points and an overall center point [*Myers et al.*, 2009]. For this study, the axial distance (α) was set equal to 1 creating a specific type of CCD commonly referred to as face-center central composite. The last design evaluated is a Latin Hypercube (LHC) design which is based

on Latin Hypercube sampling proposed by *McKay et al.* [1979] (Figure 11d) and results in a LHC design developed for computer simulation experiments [*Sacks et al.*, 1989]. The LHC with optimal spacing, which was implemented in this study, maximizes the minimum distance between design points but requires even spacing of the levels of each factor. This is an intermediate design between sphere-packing which maximizes the minimum distance between pairs of design points and the uniform method which minimizes the discrepancy between the design points and a uniform distribution. The major advantage to LHC is that design points are not limited to the edges of the design space as factor levels are not strictly set to -1, 0, or +1. Rather given *n* number of required simulations (typically a minimum of 10*k*), each factor has a corresponding *n* number of levels.

3.2.2 Response Surface Methodology (RSM)

RSM consists of a group of statistical techniques for building empirical models with the objective of relating a response (output) to the levels of predictors (DoE factors) [*Box and Draper*, 1987]. The application of RSM requires the development of an approximating model, which is based on limited observed or simulated data (i.e. training dataset), for representing the true response surface of the system [*Myers et al.*, 2009]. It is assumed that some true relationship between the expectation of the response *y*, (*E(y)*), and the inputs, ($\xi_1, \xi_2, \dots, \xi_k$), exists via physical constants (Θ) as shown

$$E(y) = \eta = f(\xi 1, \xi 2, \dots, \xi k, \theta) = f(\boldsymbol{\xi}, \boldsymbol{\theta}) \quad (1)$$

where $\boldsymbol{\xi}$ denotes a column vector referring to all *k* input variables (or factors) and $\boldsymbol{\Theta}$ represents a set of physical parameter measurements [*Myers et al.*, 2009]. However, the true response surface function $f(\boldsymbol{\xi}, \boldsymbol{\theta})$ is unknown or cannot be economically obtained due to limited observed data but can be approximated locally using an interpolating function (i.e. polynomial functions) [*Box*

and Draper, 1987]. Thus $f(\boldsymbol{\xi}, \boldsymbol{\theta})$ can be replaced with an approximating function $g(\boldsymbol{x}, \boldsymbol{\beta})$ where the coefficients in the approximating function (β_0, β_1, β_{11}, ..., β_{ij}) are the elements of $\boldsymbol{\beta}$ and where the coded inputs (x_1, x_2, …, x_k) are centered and scaled design units which make up $\boldsymbol{x}$. The approximating function then can be written as

$$y = g(\boldsymbol{x}, \boldsymbol{\beta}) + \varepsilon \tag{2}$$

Where ε represents sources of variability not accounted for in g (i.e. the effect of variables not included or possibly unknown), and y is the output response of interest. In this work, a 2nd-order polynomial approximation function was implemented, which is a linear combination of powers and products of the x terms, and is given by the following general expression [*Box and Draper*, 1987; *Myers et al.*, 2009]:

$$y = \beta_0 + \sum_{i=1}^{k} \beta_i x_i + \sum_{i=1}^{k} \beta_{ii} x_i^2 + \sum \sum_{i<j=2}^{k} \beta_{ij} x_i x_j + \varepsilon \tag{3}$$

The β terms are empirical coefficients that are estimated from fitting the approximating response function to the training dataset. The regression was done utilizing the least squares method which chooses β_0, β_1, β_{11}, ..., and β_{ij} so that the sum of the squares of the errors (ε_i) are minimized. Hereafter, Eq. 3 will be referred to as the Response Surface Equation (RSE).

3.3 Methodology

3.3.1 Generalized Workflow

EDA can typically be broken down into four main stages: 1) screening, 2) model building, 3) model evaluation, and 4) application (Figure 12). Screening is the process of using a low-level design (e.g. Plackett-Burman) to determine which DoE factors have a significant impact on the response. The screening stage may or may not be included in the EDA dependent on the number of DoE factors of interest.

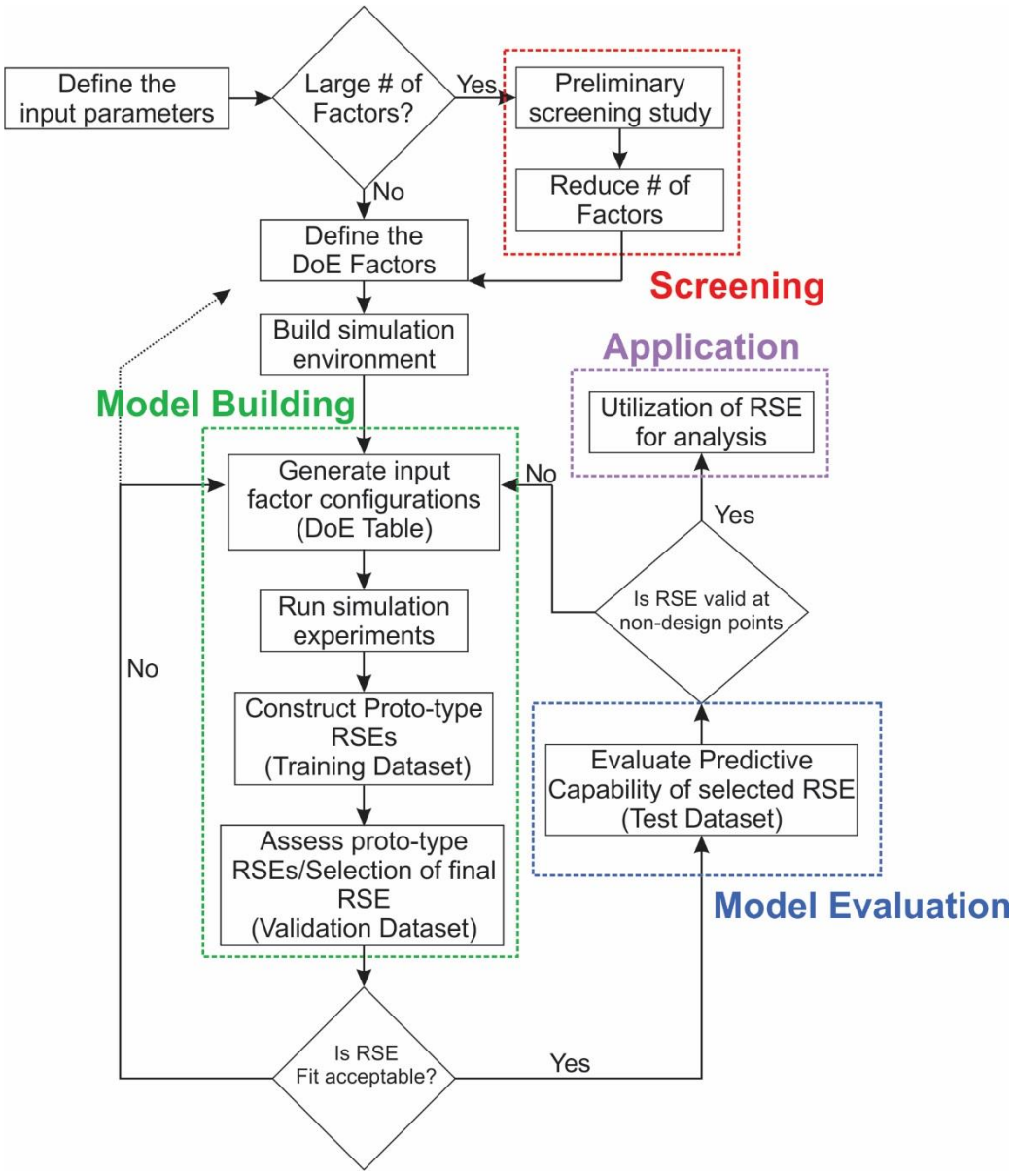

Figure 12. A generalized workflow for experiment design and analysis (EDA).

It is recommended that if the number of identified factors is greater than eight the screening stage should be included, although the optimal number of factors is somewhat arbitrary and should be based on the computational budget. For example, if a study selects a CCD with k=6, this would require a manageable 46 simulations. However, with k=7 or 8 the number increases to 80 and 82

respectively, and could approach an unmanageable number dependent on the computational cost of simulation.

The model building stage consists of constructing the simulation environment, generating a DoE table, conducting the simulations, collecting response data, and developing the RSE. This stage is similar to the conventional forward modeling combined with sensitivity studies. The input variables are sequentially varied based on the training dataset (design points) assigned in the DoE table, and corresponding outputs (response data) are collected. Preliminary regressional analyses with the training and response datasets was conducted to develop a prototype RSE.

An additional and critical step in the model building stage is the sequential evaluation of the prototype RSEs by assessing responses from randomly chosen non-design points (points that are not contained within the training dataset) simulations. Additional non-design point simulations were conducted for validation purposes where factors were randomly sampled from a uniform distribution across their respective ranges. In detail, these random simulations were subdivided into two groups: a validation and a test dataset.

These two datasets each served a different purpose in the development and evaluation of the RSE. For example, the validation dataset can be applied to determine the number of coefficients in the RSE (β_0, β_1, β_{11}, ..., and β_{ij} in eq. 3) in a forward stepwise fashion in the model building stage. Starting from a prototype RSE only containing the intercept (β_0 in eq. 3), the relative influences are determined for each factor. The forward method then adds a new variable that is the most significant (i.e. describes the most variation) to the RSE. Again, the influences are determined for all factors remaining outside of the RSE, and the evaluation process is repeated. The iterative evaluation process continues until all the factors excluded from the RSE are determined to be non-influential. Additionally, during each iteration of the forward process,

the predicted response values from the updated RSE are compared to the randomly selected validation dataset, and R^2 is calculated. Eventually, the optimum RSE is derived from the maximum R^2 relative to the randomly derived validation dataset. The goal of applying this sequential evaluation is to prevent overfitting of the training dataset when the RSE becomes overly complex resulting in poor fits and predictions of the validation dataset.

Once the optimum RSE is chosen, predictability of the RSE is assessed with the test dataset in the model evaluation step. Here, the selected RSE predicts the response data relative to the test dataset, and diagnostic statistics are calculated (i.e. R^2 and Normalized Root Mean Square Error (NRMSE)). In summary, the training and validation datasets are used to build and fine-tune the RSE, whereas the test dataset is used as an independent assessment of the RSE's predictive capability relative to new data. Finally, given adequate confirmation that the predictability is sufficient, the RSE can then be applied to predict the system responses using MC analysis.

3.3.2 Statistical and Numerical Simulators

In order to assess risk associated with pressure build-up resulting from CO_2 injection, two main software packages were used. JMP Pro 11 was used for the development of DoE tables and the RSEs along with conducting statistical analyses. For evaluating factors and responses associated with CO_2 injection, the numerical simulations were conducted utilizing TOUGH2/ECO2N. TOUGH2 is a general-purpose numerical simulator developed for the analysis of multiphase, multicomponent fluids, and heat flow within porous and fractured media [*Pruess et al.*, 1999] and ECO2N is a fluid property module capable of predicting thermophysical properties of water-, CO_2-rich, and their mixture under conditions typically found in CO_2 sequestration [*Pruess*, 2005]. TOUGH/ECO2N has been widely applied to CO_2

sequestration studies [*Doughty*, 2010; *Guyant et al.*, 2015; *Han et al.*, 2013; *Kim et al.*, 2012; *Oh et al.*, 2013; *Wainwright et al.*, 2013].

3.4 Idealized Scenario: Design Evaluation

3.4.1 Conceptual Model Description

The models developed here were considered to be a 2-dimensional slice, directly adjacent to the injection well, of a greater 3-dimensional system (Figure 13). The total vertical thickness of the model was 160 m consisting of a 100 m injection zone (storage reservoir) discretized vertically into 50 cells, overlain by a 30 m sealing formation, which is topped by a 30 m above-zone aquifer, both discretized into 15 cells vertically. The lateral extent of the model was 5,000 m with a discretization of 0.1 m selected at the injection well and logarithmically increasing away from the injection well.

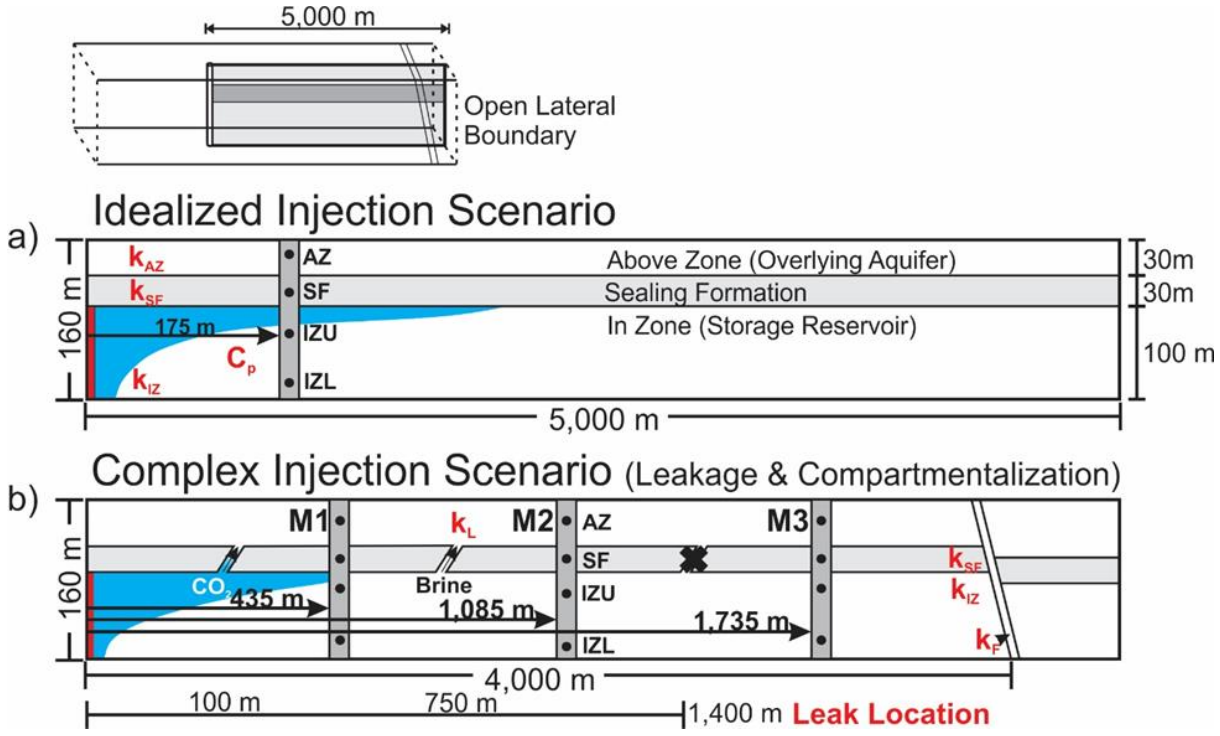

Figure 13. Schematic diagrams of the two injection scenarios; (a) an idealized scenario for DoE design evaluation study and (b) complex scenario for the analysis of pressurization in the presence of leakage pathways and fault compartmentalization. The red words in each figure represent the design factors that are considered within each scenario. The detailed description of design factors and associated real values are listed in Table 4.

The storage reservoir is considered to be infinitely acting where initially assigned pressure and temperature conditions are maintained at the right lateral boundary. The fully penetrated injection well was located at the left lateral boundary and had an average injection rate of 11.34 kg/s for the duration of the 6-year injection period (total 2.146 million metric ton injection). Initial pressure profile within the numerical model ranged from 12 MPa on the top boundary to 13.5 MPa on the bottom, following a hydrostatic pressure gradient of 9.375 kPa/m. Temperature was uniformly set to 45°C with the same temperature for injected CO_2. The relative permeability and capillary pressure are modeled independently with the van Genuchten-Mualem and van Genuchten models [*van Genuchten*, 1980] with specific values and equations presented in Table 3.

Model Parameters	Values
Initial Conditions	
Pressure	12 - 13.5 MPa
Temperature	45 °C
Porosity	0.1
Boundary Conditions (right boundary)	Constant pressure and temperature
CO_2 injection well (left boundary)	11.34 kg/s (ideal) 30 kg/s (complex)
Simulation Period	10 years
Transport Parameters	**Values**
Relative Permeability [van Genuchten-Mualem]	λ=0.457, S_{lr}=0.15, S_{lr}=1.0, S_{gr}=0.1
Brine	$S_* = (S_l - S_{lr})/(S_{ls} - S_{lr})$ $k_r^{brine} = \sqrt{S_*}\left(1 - \left(1 - {S_*}^{1/\lambda}\right)^{\lambda}\right)^2$
Supercritical CO_2 phase	$S_\# = (S_l - S_{lr})/(1 - S_r - S_{gr})$ $k_r^{gas} = (1 - S_\#)^2(1 - {S_\#}^2)$
Capillary Pressure [van Genuchten]	λ=0.457, S_{lr}=0.0, $1/P_0$=5.1E^{-4}, S_{ls}=1.0 $S^* = (S_l - S_{lr})/(S_{ls} - S_{lr})$ $P_{CO2} = -P_0\left((S^*)^{-1/\lambda} - 1\right)^{1-\lambda}$

Table 3. Model parameters and transport parameters

Where k_r^{brine} is brine relative permeability, k_r^{CO2} is CO_2-phase relative permeability, S_{ls}, S_{lr}, and S_{gr} are the brine saturation, and residual saturations of brine and CO_2, respectively, and λ is a fitting parameter of the van Genuchten-Mualem model. Table 3 presents a summary of implemented model and transport parameters.

To evaluate the performance of the multiple DoE designs in the idealized injection scenario, four uncertain parameters including in-zone permeability (k_{IZ}), the sealing formation permeability (k_{SF}), the above-zone permeability (k_{AZ}), and the in-zone compressibility (C_p) were chosen (Figure 13a) with all permeabilities assumed to be isotropic. A specific range of interest was chosen for each factor as shown in Table 4 and three discrete values corresponding to -1, 0, +1 were assigned for the DoE table.

Idealized Scenario	**Variable**	**Low [-1]**	**Mid [0]**	**High [+1]**
In Zone Permeability [m^2]	k_{IZ}	1.0×10^{-13}	1.75×10^{-13}	2.5×10^{-13}
Seal Permeability [m^2]	k_{SF}	1.0×10^{-18}	5.05×10^{-17}	1.0×10^{-16}
Above Zone Permeability [m^2]	k_{AZ}	1.0×10^{-13}	1.75×10^{-13}	2.5×10^{-13}
Compressibility [Pa^{-1}]	C_p	0.0	2.55×10^{-10}	5.1×10^{-10}
Complex Scenario				
In Zone Permeability [m^2]	k_{IZ}	5.0×10^{-14}	1.6×10^{-13}	5.0×10^{-13}
Seal Permeability [m^2]	k_{SF}	1.0×10^{-17}	3.2×10^{-17}	1.0×10^{-16}
Leakage Permeability [m^2]	k_L	1.0×10^{-16}	3.2×10^{-15}	1.0×10^{-13}
Leak Location [m from well]	LL	100	750	1400
Fault Permeability [m^2]	k_F	1.0×10^{-16}	3.2×10^{-15}	1.0×10^{-13}

Table 4. DoE factors for the idealized and complex scenario and the three levels assigned to each factor.

Consequently, each design generated a unique number of required simulations; the DSD had the fewest only requiring 9 simulations, followed by the CCD (26 simulations), BBD (27 simulations), and LHC (40 simulations) (Appendix A Tables 1-4 for complete training datasets). In addition to the required number of simulations for each design, a total of 25 additional random simulations were conducted; 15 attributed to the validation dataset and 10 prescribed to the test

dataset (See Appendix A Table 5 for complete datasets). A summary of the number of simulations conducted is listed in Table 5. The response of interest was the change in pressure from initial conditions (ΔP). The ΔP was monitored at a distance of 175 m from the injection well at two different times (Figure 13a); at the end of the injection period (T1=6 years) and at the end of the observation period (T2=10 years), at four locations such as In-Zone Lower (IZL), In-Zone Upper (IZU), Sealing Formation (SF), and Above-Zone (AZ) shown in Figure 13a.

Idealized Scenario	**Train**	**Validate**	**Test**
DSD	9	15	10
BBD	27		
CCD	26		
LHC	40		
Complex Scenario			
CCD	28	22	13

Table 5. Number of conducted simulation for the training, validate and test datasets for both the idealized and complex scenarios.

3.4.2 Utilizing the Validation Dataset to Assess the RSE Fit

The assessment of RSE fits were performed qualitatively by examination of simulated ΔP versus RSE-predicted ΔP as well as quantitatively through the R^2 values of the validation dataset. The R^2 was calculated by the following equation (4):

$$R^2 \equiv 1 - \frac{SS_{res}}{SS_{tot}} = 1 - \frac{\sum_i (y_i - f_i)^2}{\sum_i (y_i - \bar{y})^2} \quad (4)$$

In eq. 4, SS_{res} is the sum of squares of the residuals, SS_{tot} is the total sum of squares, where larger values of R^2 indicate that RSEs explain the variance of the dataset well. Figure 14 displays the training (circles), validation (diamonds), and test (triangles) datasets for the four DoE design (DSD, CCD, BBD, and LHC) at four locations (IZL: (a) and (e), IZU: (b) and (f), SF: (c) and (g), and AZ (d) and (h)) and 2 selected times (end of injection, T1=6 years (a-d), and end of

monitoring, T2=10 years (e-h)), and quantitative measures of the R^2 values are summarized in Table 6.

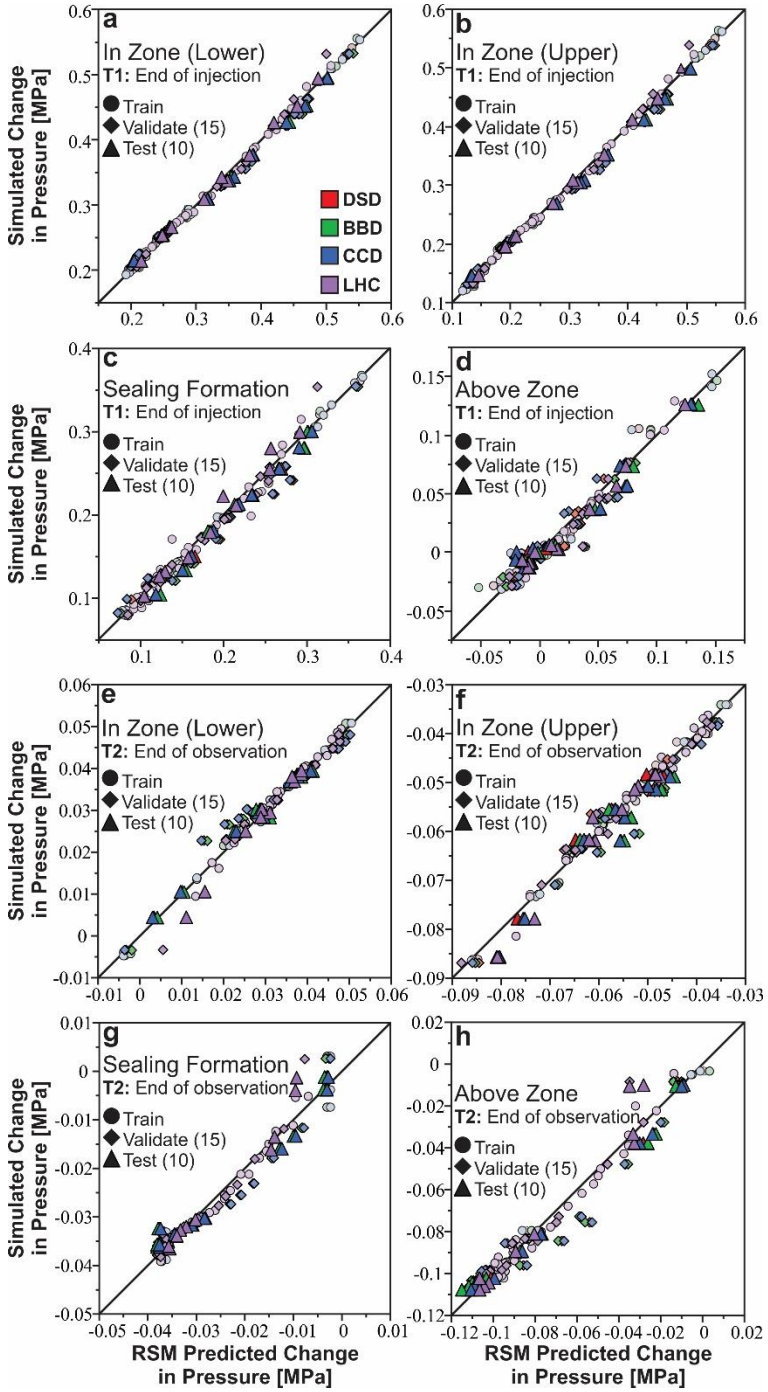

Figure 14. Simulated ΔP vs. RSE-predicted ΔP for all four evaluated designs (DSD: Red, BBD: Green, CCD: Blue, and LHC: Purple) at the end of injection (a-d) and the end of observation (e-h). Each plot displays three different symbols with circles representing the training dataset for the DoE designs (9, 27, 26, and 40 for DSD, BBD, CCD, LHC, respectively), diamonds for the validation dataset consisting of 15 randomly selected points, and triangles (10) for the test dataset.

Firstly, the R^2s of the validation dataset (R^2_{VAL}) were examined to assess how well the developed RSE explained the variation of the response dataset (output). These R^2_{VAL} were criteria for the selection of the RSE's complexity, allowing for the selection of the RSE which produced the maximum R^2_{VAL} value. For example, at T1 for the AZ location utilizing a CCD, 10 proto-type RSEs were developed with *p* equal to 4, 5, 7, 8, 9 ,11, 12, 13, 14, and 15 with *p* being the number of β terms (including the intercept) within the RSE (eq. 3). Specifically, the RSE developed with *p* equal to 5 resulted in R^2_{VAL} value of 0.8882, which was the maximum value of all proto-type RSEs tested for this time and location.

T1	**R^2_{VAL}**			
	IZL	IZU	SF	AZ
DSD	0.9856	0.9876	0.9326	0.9147
BBD	0.9824	0.9853	0.9364	0.8702
CCD	0.9824	0.9853	0.94	0.8882
LHC	0.9888	0.9912	0.9696	0.8988
	R^2_{TEST}			
	IZL	IZU	SF	AZ
DSD	0.9849	0.9877	0.9683	0.9571
BBD	0.983	0.9864	0.9668	0.9602
CCD	0.9824	0.986	0.9738	0.8325
LHC	0.9959	0.997	0.9636	0.9787
	NRMSE (Test)			
	IZL	IZU	SF	AZ
DSD	0.0379	0.0341	0.0591	0.0646
BBD	0.0242	0.0245	0.0336	0.0446
CCD	0.041	0.0364	0.0537	0.0811
LHC	0.0199	0.0169	0.0633	0.0455
	PRESS			
	IZL	IZU	SF	AZ
DSD	0.0108	0.014	0.0179	0.0181
BBD	0.0072	0.0089	0.0116	0.0146
CCD	0.0056	0.0071	0.0092	0.0066
LHC	0.632	0.0287	0.0155	0.0129

T2	**R^2_{VAL}**			
	IZL	IZU	SF	AZ
DSD	0.9295	0.9309	0.9185	0.8756
BBD	0.9417	0.9179	0.9192	0.8842
CCD	0.9211	0.9376	0.9183	0.8647
LHC	0.9583	0.9811	0.9324	0.9298
	R^2_{TEST}			
	IZL	IZU	SF	AZ
DSD	0.9865	0.9243	0.958	0.9825
BBD	0.9807	0.8973	0.9567	0.9733
CCD	0.9882	0.9228	0.9585	0.9861
LHC	0.9396	0.9521	0.9385	0.9339
	NRMSE (Test)			
	IZL	IZU	SF	AZ
DSD	0.0378	0.0879	0.0753	0.0524
BBD	0.0452	0.1024	0.0764	0.0647
CCD	0.0352	0.0853	0.0749	0.0466
LHC	0.0798	0.0699	0.0912	0.1018
	PRESS			
	IZL	IZU	SF	AZ
DSD	0.0006	0.001	0.0006	0.0041
BBD	0.0003	0.0009	0.0004	0.0026
CCD	0.0003	0.0005	0.0006	0.0025
LHC	0.001	0.0010	0.0009	0.0124

Table 6. Comparison statistics for the four-evaluated DoE designs at two times of interest (T1=Year 6 and T2=Year 10).

The examination of the R^2_{VAL} served as a first check on the adequacy of the developed RSEs. In Table 6, R^2_{VAL} represent the maximum values achieved of the sequentially tested RSEs. At T1, the average R^2_{VAL} was approximately equal to 0.952 with a maximum value of 0.991 and a minimum value of 0.870. There was a slight decrease in these values at T2 with the average dropping to 0.923 and the maximum and minimum to 0.981, and 0.865, respectively. This transition indicated that the quality of fit of the fine-tuned RSE is decreased after CO_2 injection ended. Overall, all four designs applied were able to achieve adequate approximations to the simulation model at different depths and times.

3.4.3 Assessment of RSE's Predictability via Test Dataset

Predictability of the RSE was assessed with the test dataset with measures of the R^2_{TEST}, Normalized Root Mean Square Error (NRMSE), and the Prediction Error Sum of Squares (PRESS). The R^2_{TEST} was calculated by applying eq. (4) to the test dataset and the NRMSE and the PRESS were calculated by the following eq. (5) and (6), respectively. The NRMSE was adopted rather than the RMSE due to the difference in the ranges of the response values at the four different monitoring locations. The PRESS was calculated based on a leave-one-out cross validation method, where the model was fit with a single observation withheld and then a predicted value was computed for the withheld observation, and the residual was calculated. This is repeated for all observations, which afterwards, the residuals are squared and summed resulting in the PRESS value [*Myers et al.*, 2009].

$$NRMSE = \frac{\sqrt{\frac{\sum_{i=1}^{n}\left(Y_{PRED,i}-Y_{SIM,i}\right)^2}{n}}}{Y_{PRED,max}-Y_{PRED,min}} \quad (5)$$

$$PRESS = \sum_{i=1}^{n}\left(y_i - \hat{y}_{(i)}\right)^2 \quad (6)$$

In eq. 5, Y_{PRED} is the RSE-predicted values, Y_{SIM} is the simulated-output values, $Y_{PRED,max}$ and $Y_{PRED,\,min}$ are the maximum and minimum values of the RSE-predicted values, respectively. In eq. 6, n is the number of observations, y_i is the simulated response value and $\hat{y}_i$ is the predicted response value for the i^{th} observation when the model is fit excluding observation i.

When the formation pressure reached its maximum due to CO_2 injection at T1, RSE-predicted ΔP fit better to the simulated ΔP at the in-zone locations (IZL, and IZU) than the out-zone regions (SF, and AZ) (Figure 14). This is attributed to the in-zone locations having a more direct relationship to the ΔP associated with the injection activity which occurs within the storage reservoir. In contrast, as the pressure propagates to the out-of-zone regions, complexities are added decreasing the prediction accuracy of ΔP. The statistical measures of both NRMSE and PRESS also generally support better predictability of the RSE at the in-zone locations. For example, the NRMSE of DSD at T1 was approximately twice as large for the SF (0.0591), and AZ (0.0646) when compared to the IZL (0.0379), and the IZU (0.0341) (Table 6). In addition, the PRESS values for the same DSD design showed slightly better prediction at in-zone locations 0.0108, 0.014, 0.0179, and 0.0181 for IZL, IZU, SF, and AZ, respectively. At the later time (T2) after the dissipation of the built-up pressure, the predictability of the RSE was decreased (Figure 14). The NRMSE values were increased for a majority of the DoE designs and monitoring locations and the R^2_{TEST} is vice versa. For example, the CCD at the IZU had a NRMSE of 0.0364 at T1, which increased more than twice to 0.0853 at T2 and the R^2_{TEST} value decreased from 0.986 (T1) to 0.9228 (T2) (Table 6). However, the comparison of the PRESS statistic suggest that the RSEs developed for T2 are superior to those of T1 observed by the decrease in the values (Table 6). For example, the CCD at the IZU had a PRESS value of 0.0071 at T1, which decreased to 0.0005 at T2.

3.4.4 Selection of Suitable DoE Design for Complex Geologic CO_2 Sequestration Simulations

For the evaluation of different DoE designs, the three previously mentioned statistics of R^2_{TEST}, NRMSE, and PRESS were used for the criteria. A key observation of the DoE comparison study is the limitations of the modern design (LHC), and that the classical designs provided better predictions in many cases. The limitation of LHC design occurs likely because the design points of LHC design are distributed only within the cube but does not include design points on the edges and corners of the cube (Figure 11d). The design points on either edges or corners typically corresponded the extreme values of the responses (e.g. pressure build-up), which is critical for risk assessment. Therefore, ignorance of these points may lead to greater errors in the prediction. Conversely, the other designs (DSD, BBD, and CCD), which focus the training set on the outer limits of the parameter space, do not predict as well as the LHC at the midrange response values although these classical designs predicted better at the extreme response values.

A plot of all four measured statistics is shown in Figure 15, and a complete list of the values is listed in Table 6. Both R^2_{VAL} and R^2_{TEST} for all the designs were above 0.8 in both T1 and T2; especially, a vast majority of the R^2_{TEST} (triangles) values at T1 are above 0.95. Although R^2 values give insight on how well the RSEs fitted the simulated data, these values themselves do not serve as a confirmative tool for assessing the predictability. Therefore, NRMSE (horizontal bars in Figure 15) and the PRESS (gray squares in Figure 15) statistics as well as the nature of the design itself (i.e. number of required simulations) are interpreted to select the optimum DoE design for the geologic CO_2 sequestration simulation study addressed in this work.

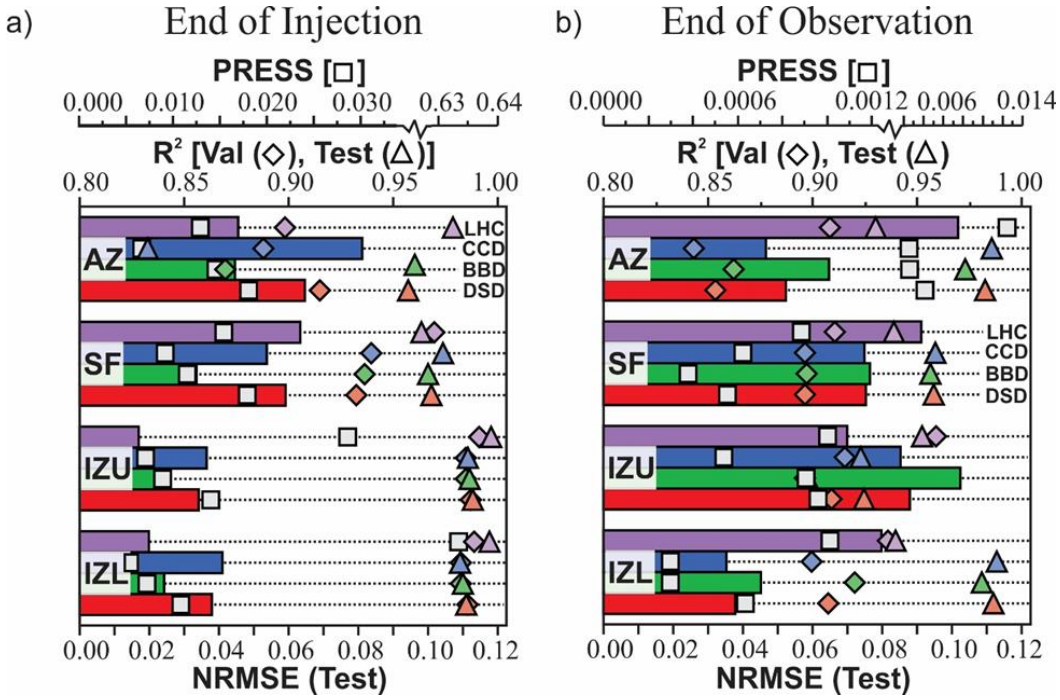

Figure 15. Comparison statistics considered for design evaluation; (a) the end of injection and (b) the end of observation. Normalized Root Mean Square Error (NRMSE) for the test dataset displayed by the horizontal bars for each location (IZL, IZU, SF, and AZ) and each design (DSD: Red, BBD: Green, CCD: Blue, and LHC: Purple). The R^2 values for the validation and test dataset are depicted by diamonds and triangles respectively. The Prediction Error Sum of Squares (PRESS) represented by squares is shown on the top-most axis.

Of the four designs, the first one eliminated as a possibility for implementation into the complex model was the LHC (purple color in Figure 15). This was justified by considering that the LHC required maximum numbers of simulations (40) although it had comparable NRMSE values relative to the other designs at T1 (Figure 15a). Furthermore, at T2, the LHC had the highest NRMSE value for 3 out of the 4 locations, showing the lowest predictability among the evaluated designs (Figure 15b). Consideration of the second statistic (PRESS) shows that in the instances when the LHC has the lowest NRMSE it has the highest PRESS value. For example, the PRESS values of the LHC at T1 are 0.632 and 0.0287 for the IZL and IZU locations, respectively. In summary, after assessment of all DoE designs across both time and space, the

additional number of simulations required by the LHC was considered not to be justified moving to the complex scenario.

The second design that was eliminated was the DSD (red color in Figure 15). The DSD typically had one of the highest NRMSE value and never had the lowest value. This same characteristic can also be seen in the PRESS statistic. Although the NRMSE and PRESS values derived from the DSD may be considered adequate or at least comparable to the other designs, there was not a high level of confidence implementing a low-level design (lowest number of required simulations: 9 training data) into the complex scenario, where the response surface could be much more complex than in the idealized scenario.

The remaining two designs (BBD and CCD) are two of the most commonly used designs [*Simpson et al.*, 2001], and measured statistics from this study also indicate that both BBD and CCD are comparable and effective designs. Figure 15 shows that the BBD slightly outperforms the CCD at the end of injection (T1) based on the NRMSE. However the CCD at the same time outperforms the BBD based on the PRESS values. At the end of observation (T2), the CCD outperforms the BBD at all locations based off the calculated NRMSE. Assessment of the PRESS values at T2 show that for the locations of IZL and AZ, both designs result in similar values of 0.003 (BBD and CCD) and 0.0026 (BBD), 0.0025 (CCD), respectively. And for the other two locations (IZU and SF), the CCD has a lower PRESS value at the IZU location and the BBD has a lower PRESS value at the SF location. Summarizing these two measures, both designs could be justified for utilization within the complex scenario. However, since the main focus of the complex scenario is the risk associated with pressurization of the reservoir system of which high changes in pressure is of most concern, the CCD design was chosen. This decision was made based on the nature of the design itself. As seen in Figure 11c (for k=3), the CCD

places design points on the vertices of the cube. These locations would represent the extreme limits of the parameter ranges and likely to be parameter settings where the highest change in pressure will occur. For this reason, it is advantageous to have design points located here to aid in the prediction of pressure associated with risk assessment.

3.5 Complex injection Scenario: Pressurization Evaluation

3.5.1 Conceptual Model Description

The dimension as well as the model and transport parameters of the complex model are the same as those in the idealized model (Table 3). Fault systems within the storage system can have a variety of effects on the injection activity ranging from barriers, impeding fluid flow and having adverse effects on pressure build up, to conduits which permits fluid flow and alleviate pressure build up [*Bense et al.*, 2013; *Caine et al.*, 1996]. Due to the diversity in their possible effects, fault systems within storage reservoirs have been the topic of previous studies such as those focused on the Cranfield CO_2-EOR site located in Mississippi [*Nicot et al.*, 2013]. To evaluate the potential impact of a fault system on pressure build-up and propagation, the current study inserted a fault system at a distance of 4,000 m from the injection well (Figure 13b). Additionally, three leakage pathways were assigned at 100, 750, and 1,400 m within the sealing formation with only one location which had a permeability that differed from the sealing formation (LL factor in Table 4) in any given simulation.

In the complex scenario, the mesh representing the lateral discretization of the model did not increase logarithmically, but rather locally refined mesh was chosen around each of the leakage pathways as well as around the faulted region in order to capture the detailed pressure responses. The resulting number of grid cells was 10,640 as compared to only 2,960 cells of the idealized model. As seen, the complex model was significantly more computationally expensive,

and this is why only the best preforming DoE design (i.e. CCD) was used to evaluate the risk associated with pressurization. The injection rate was also increased for this scenario to 31.71 kg/s (1 million metric tons per year) for the duration of the 5 year injection period (total 5 million metric ton injection).

In this scenario, the number of DoE factors increased from 4 to 5, which include in-zone permeability (k_{IZ}), sealing formation permeability (k_{SF}), leakage pathway permeability (k_L), leakage location (LL), and fault permeability (k_F) (Figure 13b) with the ranges for each parameter listed in Table 4 and all permeabilities assumed isotropic. The response of interest was again ΔP, which was collected at three locations M1: 435 m, M2: 1,085 m, and M3: 1,735 m from the injection well at the same four depths (IZL, IZU, SF, and AZ) as shown in Figure 13b. The times of interest were all during the injection period because during this period the leakage risk and associated pressure build-up is at its greatest. Also, within the context of leakage detection the sooner a leakage can be detected and managed, the less likely significant harm will be caused. Finally, the idealized scenario showed that the surrogate models performed better during the injection period. For these reasons, ΔP was observed at 0.05 (T1), 0.5 (T2), and 5.0 (T3) years.

3.5.2 Description of the Central Composite Design (CCD)

For this scenario, the CCD required 28 simulations to be conducted (Table 5). The simulations required are listed in Table 7 showing the coded values for each simulation (See Appendix B Tables 1-3 for complete response datasets). The real parameter values assigned to the coded value were presented in Table 4. Each row in Table 7 represents a designated simulation with a unique combination of parameter values with the exception of simulation #8

and #10, which are replicated center point runs. For the remainder of this work, each simulation will be referred to as a design point of the training dataset.

Simulation Number	k_{IZ}	k_{SF}	k_L	LL	k_F
1	-1	+1	+1	+1	+1
2	+1	+1	+1	+1	-1
3	-1	-1	-1	+1	+1
4	-1	+1	-1	-1	+1
5	+1	+1	-1	-1	-1
6	+1	-1	-1	-1	+1
7	+1	-1	-1	+1	-1
8	0	0	0	0	0
9	-1	-1	+1	-1	+1
10	0	0	0	0	0
11	-1	+1	-1	+1	-1
12	a	0	0	0	0
13	+1	-1	+1	+1	+1
14	-1	-1	-1	-1	-1
15	+1	-1	+1	-1	-1
16	A	0	0	0	0
17	0	0	0	0	a
18	+1	+1	-1	+1	+1
19	-1	+1	+1	-1	-1
20	0	0	a	0	0
21	+1	+1	+1	-1	+1
22	0	0	0	0	A
23	0	0	0	a	0
24	0	0	A	0	0
25	0	0	0	A	0
26	0	A	0	0	0
27	0	a	0	0	0
28	-1	-1	+1	+1	-1

Table 7. Coded CCD design table used in the complex scenario where -1 represents the lower limit of the factor range, 0 the midpoint, and +1 the upper limit. The CCD has axial points which for this study are centered on face, that is (a) is equivalent to -1 and (A) to +1.

3.5.3 Assessment of RSM Fit

The assessment of how well the response surface model performed at each location and time was carried out in a similar fashion as described in section 3. For this scenario, the total

number of random simulations conducted was equal to 35 with 22 prescribed to the validation dataset and the remaining 13 to the test dataset (Table 5) (See Appendix B Table 4 and 5-7 for complete datasets).

Figure 16 reveals key observations of how well the RSEs performed at selected times (T1, T2, and T3), depths (i.e. IZL, IZU, SF, and AZ), and monitoring location (M1, M2, and M3). The accuracy and predictability of the RSEs can qualitatively be measured from 1:1 plots of the simulated ΔP vs RSE-predicted ΔP (Figure 16a-c, 16e-g, and 16i-k) as well as quantitatively with measures of the NRMSE (bar graph) and R^2 values for the validation (diamond) and test (triangle) dataset in Figure 16d, h, and l with the precise values listed in Table 8. Generally, with increasing distance from the injection well moving from M1, M2, to M3, the NRMSE increased and the R^2 values decreased (Figure 16d, h, and l). For example, in the above-zone (AZ) region at T1, the NRMSE is 0.066 at M1 and increases to 0.085 (M2), and 0.101 (M3), while the R^2_{TEST} values decrease from 0.9436 at M1 to 0.9273 (M2), and 0.8953 (M3). This indicates that the predictability of the RSM, although acceptable at each location, is decreasing further from the injection well.

At M1 for IZL, IZU, and SF, the fit and predicative capability of the RSEs distinctively decreased with increasing time since the onset of injection; the NRMSE increased with time (Figure 16d). However, for the AZ region, a different trend is shown. Based on the NRMSE, the best prediction model (=0.0599) was at T2 followed by T3 (=0.0661), and lastly T1 (0.0665) (Table 8). For M2 in Figure 16h, the trend of NRMSE for all locations (IZL, IZU, SF, and AZ) was similar to M1. However, at M3 for IZL and IZU shown in Figure 16l, the NRMSE still increases with time but their values are much more similar to each other. For example, the NRMSE for IZL at M3 for T1 equals 0.0819, T2 (=0.0826), and T3 (=0.0918) compared to the

values at M1 which are T1 (=0.0337), T2 (=0.0496), and T3 (=0.0673). Within the two out-zone regions (SF and AZ), the predictive capabilities do not increase with increasing time. Rather, at SF the best predictive model was T2 followed by T1, then T3. In addition, at AZ, T2 was again the best followed by T3, then T1.

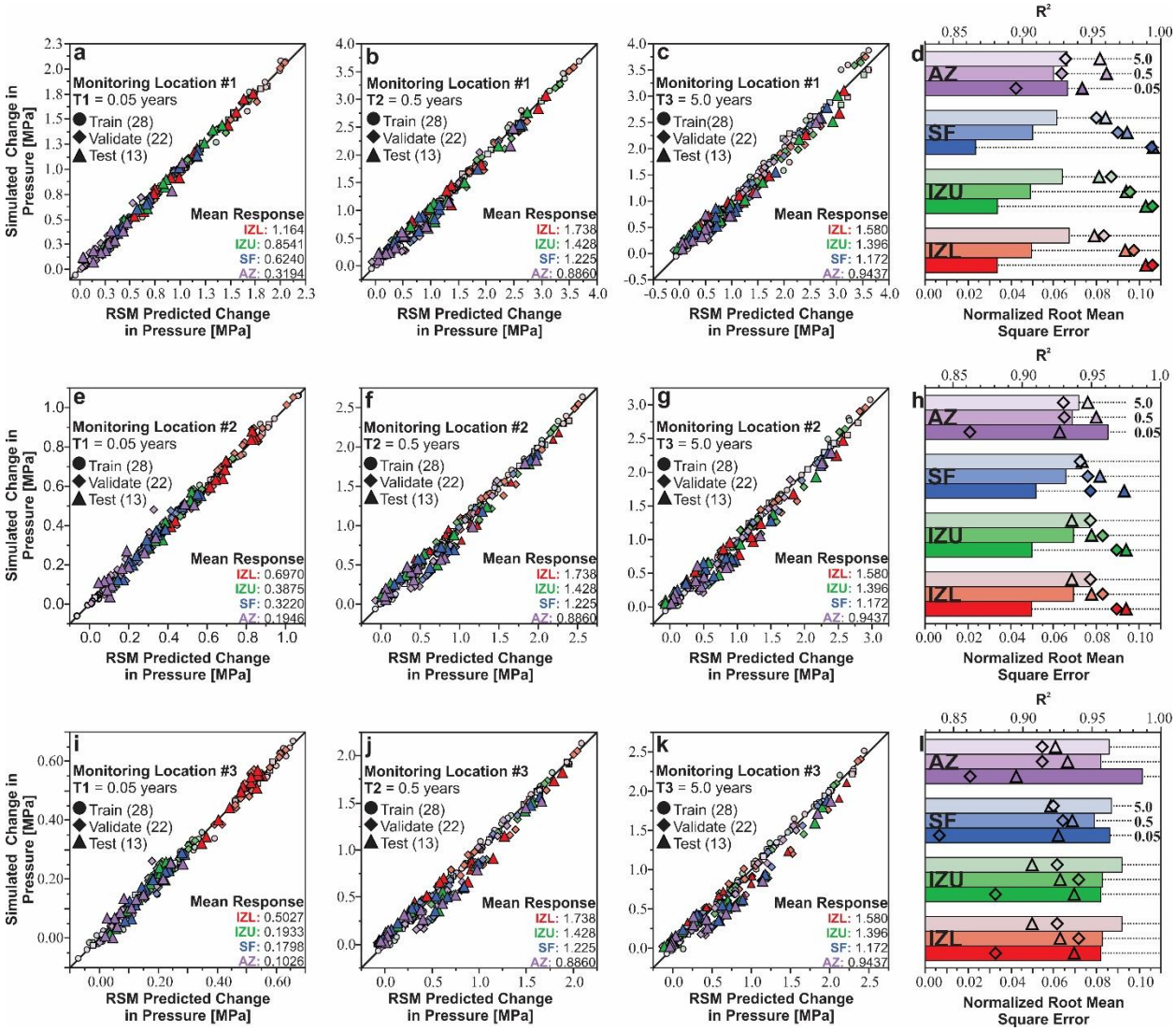

Figure 16. Visualization of the RSE fit at times T1 (a, e, and i), T2 (b, f, and j), and T3 (c, g, and k) at all three monitoring locations (M1: a-c, M2: e-g, and M3: i-k) for all four vertical depths (IZL (red), IZU (green), SF (blue), and AZ (purple)). The three right-most plots (d, h, and l) display the NRMSE as horizontal bars where the lightest color is 5.0 years and the darkest is 0.05 years. The symbols of diamonds and triangle represent the R^2 values for the validation and test dataset, respectively.

An important finding from this assessment is that the RSEs slightly over-predicted the change in pressure with both increasing distance from the injection well and increasing monitoring times. This can be seen in the 1:1 plots, where the displayed point shift to the right of the one-to-one line for M2 (Figure 16e-g) and becomes more evident at M3 (Figure 16i-k).

3.5.4 Sensitivity Analysis

DoE and RSM provide the means to conduct a sensitivity analysis of the considered parameter and allows for ranking of main, interaction, and quadratic effects. Figure 17 is a series of tornado diagrams displaying the top five most influential terms at M1 for all depths (Figure 17 a-d), the above-zone regions at M2 (Figure 17e) and M3 (Figure 17f), for T1 (blue), T2 (red), and T3 (green). The vertical axis list the factors, interaction, or quadratic term where k_{IZ} is reservoir permeability, k_F is fault permeability, k_L is leakage permeability, k_{SF} is seal permeability, and LL is Leakage Location. For example, $k_{IZ}\times k_F$ would represent the interaction term between the reservoir and fault permeability and $k_{IZ}\times k_{IZ}$ would be the quadratic term of reservoir permeability within the RSE. The horizontal axis is the t-ratio of each term, and is calculated by the ratio of the term estimate to its standard error. The length of the bar is indicative of its influence; larger bars have a larger impact on the response, and the sign (+ or -) of the t-ratio reflects the relationship which factors or terms have on the change in pressure response.

Firstly, the ranking of RSE terms are almost identical between IZL and IZU (Figure 17a and b) even though their locations were vertically distanced by 70 m (Figure 13b). At T1 (blue bar), k_{IZ} is the most influential term followed by the quadratic term of $k_{IZ}\times k_{IZ}$, k_F, interaction of $k_{IZ}\times k_F$, and finally k_L. At later times (T2: red bar and T3: green bar), the influence of k_{IZ} generally decreased with the exception of IZU at T2. Interestingly, k_F becomes an influential

parameter; k_F and the quadratic term of $k_F \times k_F$ were 2nd and 3rd rank, respectively. This suggests that faults could be acting as either a barrier or conduit governing pressure accumulation or dissipation within the in-zone regions (i.e., IZU and IZL).

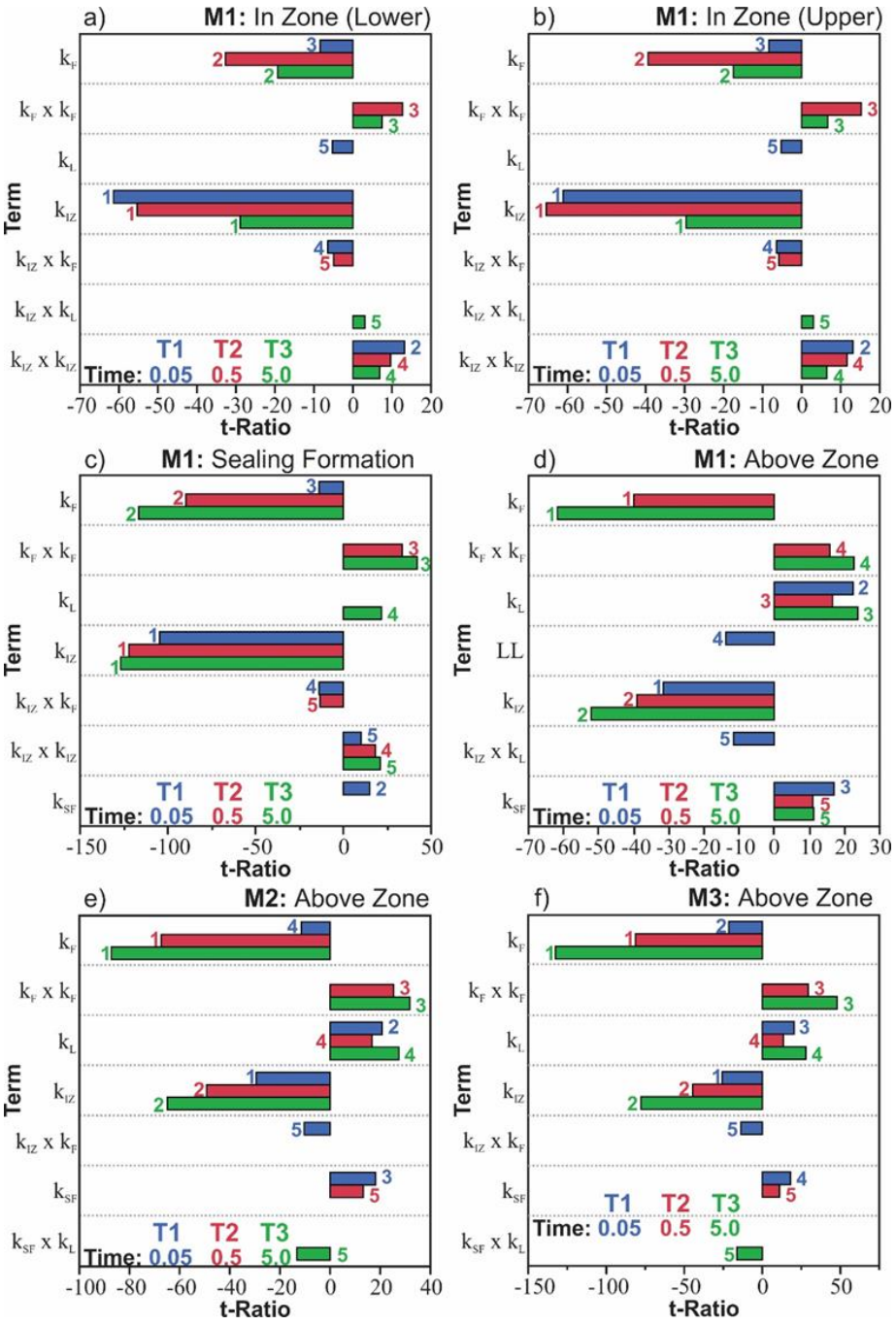

Figure 17. Tornado diagram displaying the top 5 most influential factors at monitoring location #1 (a-d) at the four depths of interest; (a) In-zone (lower): IZL, (b) In-zone (upper): IZU, (c) sealing formation: SF, and (d) above zone region (AZ). The above-zone sensitivities for M2 and M3 are shown in Figure 17e and f, respectively. The color of the bar indicates its time where 0.05 is blue, 0.5 is red and 5.0 is green.

General trends such as the ones observed at the in-zone regions are not as easily stated for the out-of-zone (SF and AZ) regions. Specific to the sealing formation shown in Figure 17c, k_{IZ} was the top ranking parameter at all times. In detail, the same top 3 influential terms (k_{IZ}, k_F, $k_F \times k_F$) appear in both T2 and T3, which is different from those (k_{IZ}, k_{SF}, k_F) at T1. The k_{SF}, which was a 2nd-ranked parameter at T1, drops out of rank at both T2 and T3. In addition, k_L only appears at T3 and is ranked 4th. The 3rd, 4th, and 5th ranked terms varies with time but generally consist of the quadratic terms of $k_F \times k_F$, $k_{IZ} \times k_{IZ}$ and the interaction effect of $k_{IZ} \times k_{F,}$ displaying the high level of influence of both k_{IZ} and k_F.

For the above-zone region (Figure 17d), k_{IZ} is the most dominant parameter only at T1, and transitioning to T2 and T3, k_F becomes 1st rank. The k_L was the 2nd most influential term on the ΔP value at T1, and then, decreased its rank to 3rd at both T2 and T3. A key observation of the influential terms on the ΔP values in the above-zone region is that k_F is not one of top 5 influencers at T1. As k_F transitions to the top-most influential parameter at T2 and T3 it begins to mask the effects of the other four parameters limiting the effectiveness of using ΔP to assess leakage at the above-zone region. The k_{SF} is ranked 3rd, followed by the LL and $k_{IZ} \times k_L$ for T1. The influence of LL is only specific to the above-zone region at T1. At the two later times, the quadratic term $k_F \times k_F$ is ranked 4th, followed by the k_{SF}.

Comparison of the sensitivities in the above-zone region at different monitoring locations (Figure 17d, e, and f) reveals that the influence of k_F on ΔP is increased. At M1T1 (Figure 17d), k_F is not among the top 5 influencers. However, at M2 (Figure 17e), k_F was ranked 4th at T1, and transitions to 1st rank at both T2 and T3. Furthermore, k_F becomes even more influential at M3T1, being ranked 2nd (Figure 17e). The increasing influence of k_F is again observed by the quadratic term $k_F \times k_F$,which is increased from 4th at M1 to 3rd at M2 and M3. Specific to k_{IZ}, the

same trend is observed at all three locations. Finally, the remaining terms, although slightly vary in their ranks, generally consist of k_L, k_{SF}, and $k_{IZ} \times k_F$.

3.5.5 Uncertainty Analysis

For each monitoring location and at all times of interest, the developed RSEs are utilized to evaluate the prediction uncertainty of the ΔP. The uncertainty analysis was carried out by conducting a 10,000-realization Monte Carlo (MC) analysis. For this analysis, each parameter was prescribed a uniform distribution, indicating that each realization within respective ranges of the factors was selected with equal probability. A random vector of the input factor results in a single predicted ΔP value, and after 10,000 realizations, an empirical probability density function (*pdf*) was created. The results of the Monte Carlo analysis implementing the response surface equation (MC-RSE) are shown in Figure 18, presenting occurrence of ΔP at all monitoring locations of the above-zone region at T1, T2, and T3. Here, the above-zone region is specifically discussed because pressure monitoring in an above-zone region has been shown to be an effective tool for evaluating whether displacement of brine or CO_2 out of the storage reservoir is occurring, as well as assessing pressure propagation through the storage system [*Meckel and Hovorka*, 2010].

Scatter-plots of all the MC-RSEs are shown with the ΔP values listed on the y-axis, and the log-permeabilities of the reservoir (k_{IZ}), seal (k_{SF}), leak (k_L), and fault (k_F) appears on the x-axis. The shaded regions on the scatter-plot are indicative of the density of realization outputs, and symbols represent outliers determined by 1.5×IQR (Interquartile Range). In addition, the dotted line represents a linear best-fit. Although the linear best-fit does not match the data precisely in some situations (Figure 18b; purple symbols representing non-linear fault influence on ΔP at M1T2), it indicates the general trends that each parameter has on the ΔP value (i.e. + or –

relation, and a steeper slope indicates a greater effect). To the right of each scatter-plot is the empirical *pdf* derived from the MC-RSE overlaid with a box-whisker plot, and values of interest are listed (i.e. median, 90, 97.5, and 99.5 percentiles). Also listed are the skewness and kurtosis values for each *pdf* providing further information to characterize its configuration for above-zone ΔP values. For skewness, a value of 0 indicates a symmetric *pdf*, and a negative represents data that is skewed upwards and positive values skewed downward. Kurtosis is a measure of steepness, where a value of 0 indicates a normal distribution, a positive value a sharper peak, and a negative value a flatter peak compared to a normal distribution.

3.5.5.1 T1: 0.05 Year Monitoring Time

Figure 18a, 18d, and 18g present the MC-RSE results for all three locations (M1, M2, and M3) at T1 (0.05 years). As described in Table 4, seal (k_{SF}) and in-zone (k_{IZ}) permeabilities range from 10^{-17} to 10^{-16} m^2 and 5×10^{-14} to 5×10^{-13} m^2, respectively. In addition, both fault (k_F) and leakage (k_L) permeabilities overlap each other from 10^{-16} to 10^{-13} m^2. In detail, in Figure 18a showing M1T1, the above-zone ΔP showed the positive best-fits with both k_{SF} and k_L even if their degrees of slopes are different. The positive relationship indicates that larger k_{SF} and k_L allows for more pressure propagation to the above-zone region, and thus, occurrence of greater ΔP appears more frequently (i.e., k_{SF} outliers (green symbols) occur more frequently toward larger permeability). In contrast, the best-fits of both k_F and k_{IZ} trend negatively with above-zone ΔP. Based on qualitative assessment of all four best-fit slopes, the k_{IZ} was the most influential factor for the above-zone ΔP value, which is consistent with the observation of the Tornado diagram in Figure 17d, 17e, and 17f. The *pdf* indicates that median ΔP and 90% percentile were 0.257 MPa and 0.503 MPa, respectively. In addition, the *pdf* is skewed downward (skewness:

0.616), indicating small ΔP occur more frequently in early time, and the peak is relatively flat (kurtosis: -0.039).

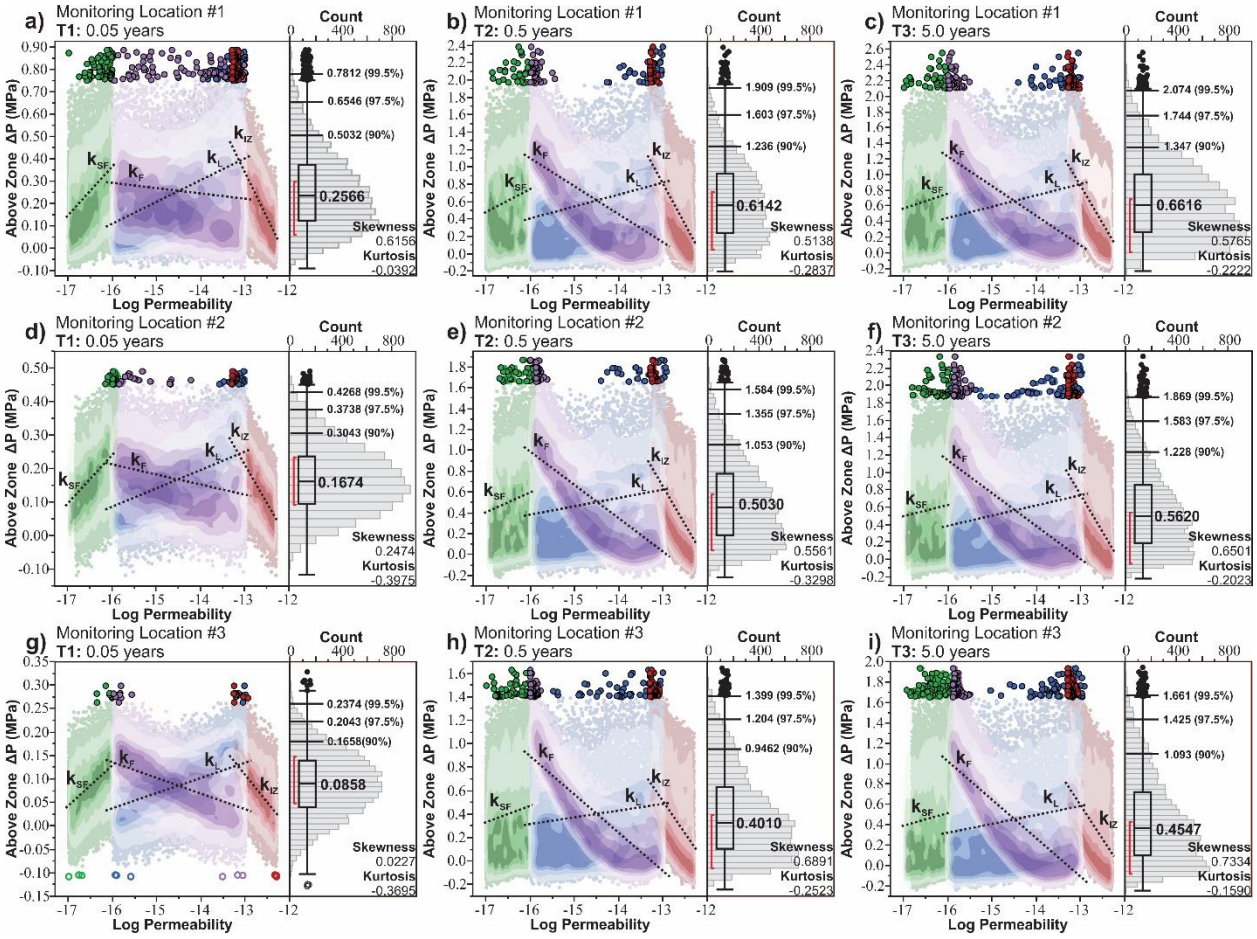

Figure 18. Monte Carlo simulation results for the above-zone region for M1 (a-c), M2 (d-f) and M3 (g-i). The shaded regions are density contours of the Monte Carlo results and the plotted dotted lines represent linear best-fits of ΔP. The symbols indicate ΔP outliers. The histogram and box-whisker plots shown in Figure 18 provide information on the ΔP distribution as well as statistical measures of median, 90, 97.5, and 99.5% quantiles, skewness, and kurtosis.

As monitoring locations move further from the injection well (M2 and M3 in Figure 18d and 18g), above-zone ΔP deceases, which appears in changes in ΔP medians from 0.257 MPa to 0.167 MPa (M2) and to 0.086 MPa (M3). In addition, the configuration of the *pdf* approaches almost symmetric normal distribution at M3. By examining the best-fits, the trends (positive or negative relationship) are maintained in spite of the different distances of monitoring locations,

but the magnitude of slope in the best-fits decreases overall except for k_F. The largest reduction of the slope appears in k_{IZ}. Oppositely, the slope for k_F increased far from the injection well and reached the largest at M3, reflecting its proximity to fault (Figure 13b).

3.5.5.2 T2: 0.5 Year Monitoring Time

Figure 18b, 18e, and 18h presents the MC-RSE results for all three locations (M1, M2, and M3) at T2 with a key thing to note being the change in the y-axis scaling. As more CO_2 is injected, an increase in ΔP value was observed at all locations relative to ones at T1; the median ΔP values increased from 0.257 (M1), 0.167 (M2), 0.086 (M3) at T1 to 0.614, 0.503, and 0.401 at T2, respectively. It can also be identified that the influence of k_F is growing while transitioning from T1 to T2. At T1, the best-fit of k_F remained relatively flat (Figure 18a, 18d, and 18g). Conversely, at T2 the slope magnitude of the best-fit for k_F becomes increased. At this time, the shaded density region of k_F is no longer described well by the linear best-fit; k_F ranging from 10^{-16} to approximately $10^{-14.5}$ m^2 has a strong negative trend with respect to the above-zone ΔP but k_F ranging from $10^{-14.5}$ to 10^{-13} m^2 has a negligible effect on the pressure. This likely indicates that when k_F is within the range of $10^{-14.5}$ to 10^{-16} m^2 the fault is acting as a barrier within the system increasing ΔP, and when k_F is $10^{-14.5}$ to 10^{-13} m^2 it acts as a conduit with little effect on the ΔP. Further examination of the best-fits indicates that k_{SF} and k_L have a positive relation with the above zone ΔP, which is consistent with observations at T1. The magnitude of the slope for these two parameters is considerably less than that of the k_{IZ} and k_F. Nevertheless, the outliers, ΔP greater than 1.5×IQR, of k_L were distributed across a wide range of a log-permeability values at M3 (Figure 18h), implying that large ΔP could occur at the above-zone with wide range of k_L.

The *pdfs* also become further skewed downward with skewness of 0.514, 0.556, and 0.689 for M1, M2, and M3, respectively, indicating that occurrence of higher ΔP values at the above-

zone region become increasingly less common. Here the greatest change in *pdf* shape is observed at M3 where the *pdf* at T1 (Figure 18g) was very similar to a normal distribution with a skewness of 0.023, but at T2 (Figure 18h) became heavily skewed downward with at value of 0.689. Overall, the *pdfs* are flatter at all monitoring locations during the transition from T1 to T2; kurtoses shifted to increased values.

3.5.5.3 T3: 5.0 Year Monitoring Time

Figure 18c, 18f, and 18i present the MC-RSE results at the end of the injection period (T3) for all three locations (M1, M2, and M3). Again, the influence of each parameter is similar to those in T2 (0.5 years) with both k_{IZ} and k_F being the dominant influencers of ΔP. The MC-RSE analysis allows for the identification of key ΔP values that are beneficial in the context of risk assessment. From this analysis, it can be identified that the 90, 97.5, and 99.5 percentile values are 1.347, 1.744, and 2.074 MPa, respectively, for M1 (Figure18c). These values are decreased to 1.228, 1.583, 1.869 MPa for M2 (Figure 18f), and 1.093, 1.425, and 1.661 MPa for M3 (Figure 18i). The identification of ΔP percentiles as well as the factors is a key advantage to application of MC-RSE. To this end, outliers (1.5×IQR) for M1 roughly correspond to the ΔP greater than the 99.5 percentile value (Figure 18c). Interestingly, these outliers can arise from any k_{SF} values regardless of the other three parameters values. For example, in order to attain a ΔP value above the 99.5 percentile, k_F must be between $10^{-15.5}$ and 10^{-16} m^2. The k_L does not have as strong of an impact, and the 99.5 percentile of ΔP occurs at k_L between 10^{-13} and $10^{-14.5}$ m^2, while the k_{IZ} is limited to between $10^{-12.75}$ and 10^{-13} m^2. The ranges of these parameters, which result in ΔP greater than the 99.5 percentile values, remain relatively consistent for both M2 (Figure 81f) and M3 (Figure 18i) with the exception of the k_L. For M2 and M3, k_L begins to have less influence on the high ΔP reservoir simulations.

3.5.6 Risk Assessment Associate with Leakage and Pressurization Due to Compartmentalization

Of main interest are the effects of k_F and k_L, as these are the two factors associated with pressurization and leakage risk respectively. Figure 19 shows the cumulative density functions, *cdfs*, of the above-zone ΔP at M1T1 and M1T2 influenced by k_F and k_L. The black-lines represent unconditional *cdfs* where all 5 factors are randomly sampled from a uniform distribution. The colored lines represent *cdfs* conditioned to k_L (Figure 19a and c) and k_F (Figure 19b and d). These *cdf's* are derived by random sampling of all factors except k_L (Figure 19a and c) and k_F (Figure 19b and d). There are a total of 16 conditional *cdfs* for each figure; log-permeability first set equal to -13 then decreased by 0.2 till -16. These values were then binned into three risk levels consisting of high risk (red), medium risk (green), and low risk (blue). Also listed on the figure are conditional probabilities for each of the risk levels given a ΔP value greater than the 80th percentile and a value less than or equal to the 60th percentile. The conditional probabilities were calculated by the following equation:

$$P(A|B) = \frac{P(A \cap B)}{P(B)} \tag{7}$$

Here A is the event of interest (i.e. k_L is within the low risk range) and B is assumed to have occurred (i.e. ΔP value above or below a certain value). $P(A \cap B)$ is the probability that both event A and B occurred, and $P(B)$ is the probability of event B. In eq. 7, $P(A|B)$ is then the probability that A will occur when given B has already occurred.

For the risk assessment of leakage of CO_2 or brine, the range of the k_L was divided into three levels of permeability between 10^{-13} and 10^{-14} m^2 for high risk, 10^{-14} to 10^{-15} m^2 for medium risk, and 10^{-15} to 10^{-16} m^2 for low risk (Figure 19a and c). At M1T1 (Figure 19a), if $\Delta P > 0.406$ MPa at the above-zone region, there is a 63.5% probability that k_L falls within 10^{-13} to 10^{-14} m^2

indicating a high risk scenario, a 27.1% probability there exists a medium risk leakage pathway (10^{-14} to 10^{-15} m^2), and a 9.4% probability that a low risk pathway (10^{-15} to 10^{-16} m^2) is present. For T2 (Figure 19c), the probability of a high risk pathway decreases to 48.7%, medium risk increases slightly to 31.4%, and low risk doubles to 19.0%. This trend is likely due to the increasing effect that k_F has on ΔP value at the above-zone (as discussed in section 5.4 and 5.5).

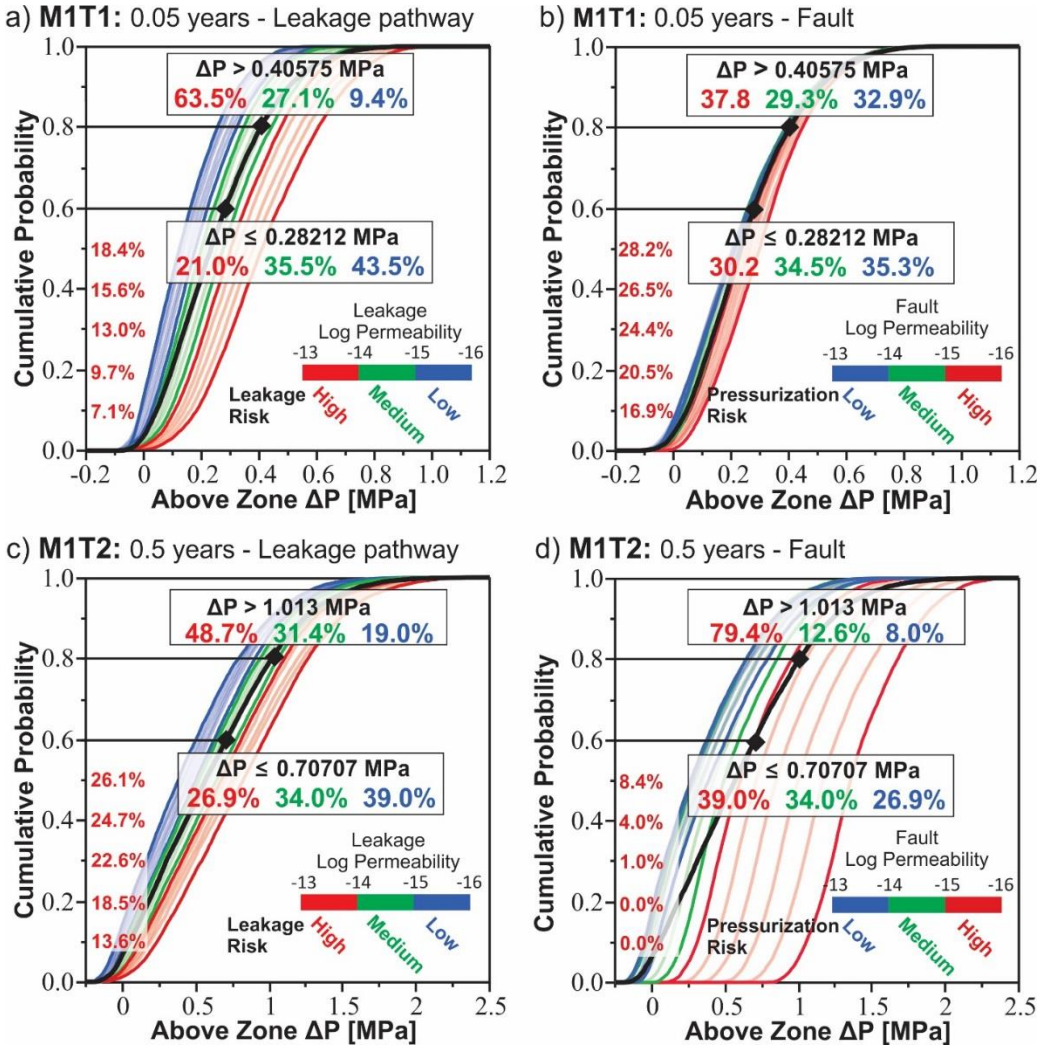

Figure 19. Conditional (colored lines) and unconditional (thick black line) *cdf's* for M1 at times 0.05 years (a and b) and at 0.5 years (c and d). Here, a and c show the *cdfs* for leakage permeability, where red indicates high leakage risk (k_L: 10^{-13} to 10^{-14} m^2) scenarios, green medium risk (k_L: 10^{-14} to 10^{-15} m^2), and blue low risk (k_L: 10^{-15} to 10^{-16} m^2). Figure 9 c and d show the *cdfs* for fault permeability, where red indicates high pressurization risk (k_F: 10^{-15} to 10^{-16} m^2), green medium risk (k_F: 10^{-14} to 10^{-15} m^2), and blue low risk (k_F: 10^{-13} to 10^{-14} m^2). Also listed are the 80th percentile values with the conditional probability of the three levels of risks if the AZ ΔP is above the value, as well as the 60th percentile value with the conditional probabilities if AZ ΔP is below the value. The red values listed are the conditional probabilities of the high risk scenarios for AZ ΔP less than or equal to the 50, 40, 30, 20, 10th percentiles.

At M1T1 (Figure 19a), the 60th percentile value is 0.282 MPa. If the ΔP value at the above-zone region is less than or equal to this value, the probability of k_L being a low risk pathway (10^{-15} to 10^{-16} m^2) is 43.5% followed by a medium risk pathway (35.5%) and lastly a high risk pathway (21.0%). At the later time (M1T2) (Figure 19b), the 60th percentile increases to 0.707 MPa, and the likelihood associated with the three risk levels shift to 26.9%, 34.0%, and 39.0% for high, medium, and low, respectively. Here the probability of a high risk pathway increases, medium risk slightly decrease, and low risk decreases compared to M1T1. The red values listed along the left axis represent the conditional probability of a high risk scenario relative to k_L for pressure values less than or equal to the 10th, 20th, 30th, 40th, and 50th percentile values. It can be seen that with increasing pressure moving from the 10th to 60th percentile there is a steady increase in the likelihood of a k_L pathway with high risk. This trend is observed at both M1T1 and M1T2.

Figure 19b and d display the risk of pressurization associated with compartmentalization of the storage system via an adjacent fault system. Here a fault permeability between 10^{-13} and 10^{-14} m^2 is classified as a low risk event, 10^{-14} to 10^{-15} m^2 a medium risk, and 10^{-15} to 10^{-16} m^2 considered a high risk scenario. At M1T1 (Figure 19b) given an $\Delta P >$ the 80th percentile at the above-zone region, the probability of the risk levels are similar with values of 37.8%, 29.3%, and 32.9% for high, medium, and low risk, respectively. The similarity in the values are indicative of the little influence that k_F has on ΔP at T1. Conversely, at M1T2 (Figure 19d) the values become significantly different when the k_F is the dominant parameter with values of 79.4%, 12.6%, and 8.0% for high, medium, and low risk scenarios, respectively.

If the pressure observed in the AZ region is ≤0.282 (60th percentile) at M1T1 (Figure 19b) again the probabilities of the risk levels are relatively similar with a 30.2% chance of a high

risk scenario, 34.5% medium risk, and 35.3% low risk. Again considering this pressure condition at T1 the little influence of the fault adds complications to determining the permeability of the fault based solely on the AZ pressure. However, this trend remains moving to T2 with values of 39%, 34.0%, and 26.9% for high, medium, and low risk, respectively. Interestingly, it can be seen that for AZ $\Delta P \leq$ the 10^{th}, and 20^{th} percentile there is a 0% chance of a high risk scenario. This observation is unique M1T2 considering the risk associated with fault permeability.

3.6 Discussion and Conclusions

In order to evaluate the pressurization of a CO_2 storage reservoir, four designs (DSD, BBD, CCD, and LHC) were firstly evaluated to investigate how well the developed RSEs were able to fit the datasets ($R^2_{VAL,\ TEST}$) as well as how well they were able to predict new data (NRMSE and PRESS). Design evaluation addressed in section 4 is crucial for proper design selection because advice provided by previous literature can be inconsistent and dependent on the specific study referred to. For example, *Giunta et al.* [2003] states that modern designs (i.e. Latin Hypercube) are preferable over classical DoE design when implementing EDA which utilizes a deterministic computer simulation. This advice is based on the fundamental assumptions of DoE and least squares regressional analysis. For example, the error (ε) term in eq. (2) and (3) is composed of two parts; ε_{BIAS} or error of the approximation and ε_{RANDOM} caused by measurement errors. The caution attributed to the use of traditional EDA methods is that ε_{RANDOM} is equal to 0 for a deterministic simulation. Due to this limitation, the validation of the RSE using additional data points (i.e, validation and test datasets) is essential with which the NRMSE for these additional points can be calculated in order to assess model accuracy. Another method that remains valid for deterministic computer simulations is leave-one-out cross validation which shares similarities to the PRESS statistic utilized within this work. Given the

potential problems that arise in applying least-squares regressional analysis to deterministic simulations gives way to a trade-off between appropriateness and practicality [*Simpson et al.*, 2001]. Furthermore, *Simpson et al.* [2001] points out if DoE and RSM used on data derived from a deterministic computer simulation can provide good agreement between the simulated and predicted values, then there remains no reason to discard the approximation model.

This work, which focused on the application of DoE and RSM to a computer simulation, found that the classical DoE designs paired with least squares regressional analysis performed adequately well and even could be considered better prediction models compared to modern designs. This finding is consistent with previous studies, which applied both DoE and RSM to deterministic computer simulations [*Peng and Gupta*, 2004; *Schuetter et al.*, 2014; *Yeten et al.*, 2005]. It should be noted however that this conclusion can be dependent on the statistics used to evaluate the design's performance as well as where and when the response (output) is observed.

Overall, this work presented an evaluation of multiple designs consisting of classical and modern designs. This evaluation heavily focused on the accuracy of the predictions for each method and utilized additional random datasets to assess the performance of each design. It was shown by a holistic evaluation of the designs mainly utilizing NRMSE of the test dataset and the calculated PRESS statistic that the Box-Behnken and Central Composite designs were best suited to achieve the research objectives. For the complex scenario, a Central Composite design was implemented, and was successfully able to achieve adequate approximations to the numerical simulations at a variety of locations and times (Figure 16). Following verification of the developed RSEs a sensitivity and Monte Carlo analysis were conducted. This found that at the above zone region change in pressure sensitivities were dynamic with respect to increasing time post onset of injection and increasing lateral distance from the injection well. The MC-RSE was

further able to identify ranges of DoE factors which resulted in outlier pressure values as well as derive empirical *pdf's* and *cdf's* allowing for the identification of significant pressure values. The MC-RSE also utilized in the risk assessment associated with pressurization due to compartmentalization as well as leakage of CO_2 and/or formation bine. This allowed for the identification that at M1T1 if the AZ ΔP was $\leq$0.282 (60^{th} percentile) MPa there was a 21.0% chance of a high risk scenario with respect to leakage permeability and a 30.2% with respect to compartmentalization. Moving to T2 if the AZ $\Delta P \leq 0.707$ MPa (60^{th} percentile) the likelihood of a leakage high risk scenario increases to 26.9%, and of a fault high risk scenario increases to 39.0%. At M1T1 a ΔP greater than the 80^{th} percentile was more readily attributed to a high k_L (high risk) resulting in the conditional probability of 63.5%. The relatively small impact of k_F at M1T1 allowed for adequate determination of the leakage risk associated with $\Delta P > 0.405$ MPa. However, at T2 the determination of the associated leakage risk for $\Delta P > 1.01$ MPa was inhibited due to the significantly greater influence k_F had on the pressure response compared to k_L.

This work further supports that although traditional methods applied to deterministic computer simulations can encounter potential pitfalls, these can be accounted for, and assessment and verification of the RSE can be carried out using additional random simulations.

Chapter 3 References

Ashraf, M. (2014), Geological storage of CO_2: Heterogeneity impact on the behavior of pressure, *International Journal of Greenhouse Gas Control*, *28*, 356-368, doi:http://dx.doi.org/10.1016/j.ijggc.2014.06.018.

Bauman, J.H., and deo, M.D. (2011), Parameter space reduction and sensitivity analysis in complex thermal subsurface production processes, *Energy Fuels*, *25*, 251-259, doi:http://dx.doi.org/10.1021/ef101225g.

Benisch, K., and Bauer, S. (2013), Short- and long-term regional pressure build-up during CO_2 injection and its applicability for site monitoring, *International Journal of Greenhouse Gas Control*, *19*, 220-233, doi:http://dx.doi.org/10.1016/j.ijggc.2013.09.002.

Bense, V.F., Gleeson, T., Loveless, S.E., Bour, O., and Scibek, J. (2013), Fault zone hydrogeology, *Earth-Science Reviews*, *127*, 171-192, doi:http://dx.doi.org/10.1016/j.earscirev.2013.09.008.

Birkholzer, J.T., Zhou, Q., and Tsang, C.-F. (2009), Large-scale impact of CO_2 storage in deep saline aquifers: A sensitivity study on pressure response in stratified systems, *International Journal of Greenhouse Gas Control*, *3*(2), 181-194, doi:http://dx.doi.org/10.1016/j.ijggc.2008.08.002.

Box, G.E.P., and Behnken, D.W. (1960), Some new three level designs for the study of quantitative variables, *Technometrics*, *2*(4), 455-475, doi:http://dx.doi.org/10.1080/00401706.1960.10489912.

Box, G.E.P., and Draper, N.R. (1987), *Empirical moel-building and response surfaces*, John Wiley & Sons, New York.

Box, G.E.P., and Wilson, K.B. (1951), On the experimental attainment of optimum conditions, *Journal of the Royal Statistical Society*, *13*(1), 1-45.

Caine, J.S., Evans, J.P., and Forster, C.B. (1996), Fault zone architecture and permeability structure, *Geology*, *24*(11), 1025-1028, doi:http://dx.doi.org/10.113/0091-7613.

Can, B., and Heavey, C. (2011), Comparison of experimental designs for simulation-based symbolic regression of manufacturing systems, *Computers & Industrial Engineering*, *61*, 447-462, doi:http://dx.doi.org/10.1016/j.cie.2011.03.012.

Cavanagh, A., and Wildgust, N. (2011), Pressurization and brine displacement issure for deep saline formation CO_2 storage, *Energy Procedia*, *4*, 4814-4821, doi:http://dx.doi.org/10.1016/j.egypro.2011.02.447.

Chabora, E.R., and Benson, S.M. (2008), Brine displacement and leakage detection using pressure measurements in aquifers overlying CO_2 storage reservoirs, paper presented at International Conference on Greenhouse Gas Control Technologies (GHGT-9), Energy Procedia, Washington DC, 2008 November 16-20.

Clarke, S.M., Griebsch, J.H., and Simpson, T.W. (2004), Analysis of support vector regression fro approximation of complex engineering analyses, *Journal of Mechanical Design*, *127*(6), 1077-1087, doi:http://dx.doi.org/10.1115/1.1897403.

Doughty, C. (2010), Investigation of CO_2 plume behavior for a large-scale pilot test of geolgoic carbon storage in a saline formation, *Transport in Porous Media*, *82*(1), 49-76, doi:10.1007/s11242-009-9396-z.

Friedmann, F., Chawathe, A., and Larue, D.K. (2003), Assessing uncertainty in channelized reservoirs using experimental designs, *SPE Reservoir Evaluation & Engineering*, 264-274, doi:http://dx.doi.org/10.2118/85117-PA.

Giunta, A.A., Wojtkiewics, S.F., Jr., and Eldred, M.S. (2003), Overview of modern design of experiments methods for computational simulations, in *AIAA Aerospace Sciences Meeting and Exhibit*, edited, AIAA, Reno, NV.

Gupta, R., Collinson, R., Smith, G.C., Ryan, S.A., and Louis, J.P. (2008), History Matching of Field Production Using Desing of Experiments, in *SPE Asia Pacific Oil and Gas Conference and Exhibition*, edited, Society of Petroleum Engineers, Perth, Australia, doi:http://dx.doi.org/10.2118/115685-MS.

Guyant, E., Han, W.S., Kim, K.-Y., Park, M.-H., and Kim, B.-Y. (2015), Salt precipitation and CO_2/brine flow distribution under different injection well completions, *International Journal of Greenhouse Gas Control*, *37*, 299-310, doi:http://dx.doi.org/10.1016/j.ijggc.2015.03.020.

Han, W.S., Kim, K.-Y., Park, E., McPherson, B.J., Lee, S.-Y., and Park, M.-H. (2013), Modeling of spatiotemporal thermal response to CO_2 injection in saline formations: interpretation for monitoring, *Transport in Porous Media*, *93*(3), 381-399, doi:10.1007/s11242-012-9957-4.

Hu, L., Pan, L., and Zhang, K. (2012), Moedeling brine leakage to shallow aquifer through an open wellbore using T2WELL/ECO2N, *International Journal of Greenhouse Gas Control*, *9*, 393-401, doi:http://dx.doi.org/10.1016/j.ijggc.2012.05.010.

IPCC (2005), IPCC Special report on carbon dioxide capture and storage*Rep.*, Cambridge University Press, Cambridge.

Jones, B., and Nachtsheim, C. (2011), A class of three-level designs for definitive screening in the presence of second-order effects, *Journal of Quality Technology*, *43*(1), 1-15, doi:http://dx.doi.org/10.1007/978-3-7908-2410-0_14.

Jung, Y., Zhou, Q., and Birkholzer, J.T. (2013), Early detection of brine and CO_2 leakage through abandoned wells using pressure and surface-deformation monitoring data: Concept and demonstration, *Advances in Water Resources*, *62*, 555-569, doi:http://dx.doi.org/10.1016/j.advwatres.2013.06.008.

Kim, K.-Y., Han, W.S., Oh, J., Kim, T., and Kim, J.-C. (2012), Characteristics of salt-precipitation and the associated pressure build-up during CO_2 storage in saline aquifers, *Transport in Porous Media*, *92*, 397-418, doi:10.1007/s11242-011-9909-4.

Kleijnen, J.P.C. (2005), An overview of the desing and analysis of simulation experiments for sensitivity analysis, *European Journal of Operational Research*, *164*(2), 287-300, doi:http://dx.doi.org/10.1016/j.ejor.2004.02.005.

LeNeveu, D.M. (2011), Analysis of potential acid gas leakage from wellbores in Alberta, Canada, *International Journal of Greenhouse Gas Control*, *5*, 862-879, doi:http://dx.doi.org/10.1016/j.ijggc.2011.01.009.

Li, S., and Zhang, Y. (2014), Model complexity in carbon sequestration: A design of experiment and response surface uncertainty analysis, *International Journal of Greenhouse Gas Control*, *22*, 123-138, doi:http://dx.doi.org/10.1016/j.ijggc.2013.12.007.

McKay, M.D., Beckman, R.J., and Conover, W.J. (1979), Comparison of three methods for selecting values of input variables in the analysis of output from a computer code, *Technometrics*, *21*(2), 239-245, doi:http://dx.doi.org/10.1080/00401706.1979.10489755.

Meckel, T., and Hovorka, S. (2010), Above-zone pressure monitoring as a surveilance tool for carbon sequesration projects, in *SPE Internation Conference on CO_2 Capture, Storage, and Utilization*, edited, Society of Petroleum Engineers, New Orleans, Louisiana, doi:http://dx.doi.org/10.2118/139720-MS.

Meckel, T.A., Zeidouni, M., Hovorka, S.D., and Hosseini, S.A. (2013), Assessing sensitivity to well leakage from three years of continuous reservoir pressure monitoring during CO_2 injection at Cranfield, MS, USA, *International Journal of Greenhouse Gas Control*, *18*, 439-448, doi:http://dx.doi/org/10.1016/j.ijggc.2013.01.019.

Myers, R.H., Montgomery, D.C., and Anderson-Cook, C.M. (2009), *Response Surface Methodology: Process and product optimization using designed experiments*, John Wiley & Sons, Hoboken, New Jersey.

Nicot, J.-P., Oldenburg, C.M., Houseworth, J.E., and Choi, J.-W. (2013), Analysis of potential leakage pathways at the Cranfield, MS, U.S.A., CO_2 sequestration site, *International Journal of Greenhouse Gas Control*, *18*, 388-400, doi:http://dx.doi.org/10.1016/j.ijggc.2012.10.011.

Oh, J., Kim, K.-Y., Han, W.S., Kim, T., Kim, J.-C., and Park, E. (2013), Experimental and numerical study on supercritical CO_2/brine transport in a fractured rock: Implications on mass transfer, capillary pressure and storage capacity, *Advance in Water Resources*, *63*, 442-453, doi:dx.doi.org/10.1016/j.advwatres.2013.03.007.

Peng, C.Y., and Gupta, R. (2004), Experimental design and analysis methods in multiple deterministic modelling for quantifying hydrocarbon in-place probability distribution curve, in *SPE Asia Pacific Conference on Integrated Modelling for Asset Management*, edited, Society of Petroleum Engineers, Kuala Lumpur, Malaysia, doi:http://dx.doi.org/10.2118/87002-MS.

Pruess, K. (2005), ECO2N: A TOUGH2 fluid property module for mixtures of Water, NaCl, and CO_2*Rep.*, Lawrence Berkeley National Laboratory.

Pruess, K., Oldenburg, C., and Moridis, G. (1999), TOUGH2 User's guide, version 2.0*Rep.*, Lawrence Berkeley national Laboratory.

Rohmer, J., and Bouc, O. (2010), A response surface methodology to address uncertainties in cap rock failure assessment for CO_2 geological storage in deep aquifers, *International Journal of Greenhouse Gas Control*, *4*, 198-208, doi:http://dx.doi.org/10.1016/j.ijggc.2009.12.001.

Rutqvist, J., Birkholzer, J., Cappa, F., and Tsang, C.-F. (2007), Estimating maximum sustainable injection pressure during geological sequestration of CO_2 using couple fluid flow and geomechanical fault-slip analysis, *Energy Conversion and Management*, *48*, 1798-1807, doi:http://dx.doi.org/10.1016/j.enconman.2007.01.021.

Sacks, J., Schiller, S.B., and Welch, W.J. (1989), Designs for computer experiments, *Technometrics*, *31*(1), 41-47.

Schuetter, J., Mishra, S., Ganesh, P.R., and Mooney, D. (2014), Building Statistical Proxy Models for CO_2 Geologic Sequestration, *Energy Procedia*, *63*, 3702-3714, doi:http://dx.doi.org/10.1016/j.egypro.2014.11.399.

Schultz, M.T., Small, M.J., Fischbeck, P.S., and Farrow, R.S. (2006), Evaluating response surface designs for uncertainty analysis and prescriptive appliations of a large-scale water quality model, *Environmental Modelling & Software*, *11*, 345-359, doi:http://dx.doi.org/10.1007/s10666-006-9043-9.

Simpson, T.W., Poplinski, J.D., Koch, P.N., and Allen, J.K. (2001), Metamodels for computer-based engineering design: survey and recommendations, *Engineering with Computers*, *17*(2), 129-150, doi:http://dx.doi.org/10.1007/PL00007198.

Sun, A.Y., Zeidouni, M., Nicot, J.-P., Lu, Z., and Zhang, D. (2013), Assessing leakage detectability at geologic CO_2 sequestration sites using the probabilistic collocation

method, *Advances in Water Resources*, *56*, 49-60, doi:http://dx.doi.org/10.1016/j.advwatres.2012.11.017.

van Genuchten, M.T. (1980), A closed-form equation for predicting the hydraulic conductivity of unsaturated soils, *Soil Science Society of America*, *44*, 892-898, doi:10.2136/sssaj1980.03615995004400050002x.

Wainwright, H.M., Finsterle, S., Zhou, Q., and Birkholzer, J.T. (2013), Modeling the performance of large-scale CO_2 storage systems: A comparison of different sensitivity analysis methods, *International Journal of Greenhouse Gas Control*, *17*, 189-205, doi:10.1016/j.ijggc.2013.05.007.

White, C.D., Willis, B.J., Narayanan, K., and Dutton, S.P. (2001), Identifying and estimating significant geologic parameters with experimental design, *Society of Petroleum Engineers Journal*, *6*(3), 311-324, doi:http://dx.doi.org/10.2118/74140-PA.

Wriedt, J., Deo, M., Han, W.S., and Lepinski, J. (2014), A methodology for quantifying risk and likelihood of failure for carbon dioxide injection into deep saline reservoirs, *International Journal of Greenhouse Gas Control*, *20*, 196-211, doi:http://dx.doi.org/10.1016/j.ijggc.2013.10.021.

Yeten, B., Castellini, A., Guyaguler, B., and Chen, W.H. (2005), A comparison study on experimental design and response surface methodologies, in *SPE Reservoir Symposium*, edited, Society of Petroleum Enginers, Houston, TX, doi:http://dx.doi.org/10.2118/93347-MS.

Zeidouni, M., and Pooladi-Darvish, M. (2012), Leakage characterization through above-zone pressure monitoring: 2-Design considerations with application to CO_2 storage in saline aquifers, *Journal of Petroleum Science and Engineering*, *98-99*, 69-82, doi:http://dx.doi.org/10.1016/j.petrol.2012.09.005.

Chapter 4

Concluding Remarks

The Previous two chapters discussed potential risks and challenges of Geologic CO_2 Sequestration (GCS). Chapter 2 mainly discussed possible adverse effects of precipitated solid salt due to the injection of dry-supercritical CO_2, which can cause near-well pressure build-up resulting in loss of well injectivity. In order to mitigate this adverse effect, previous studies have suggested a variety of methods. *Pruess and Müller* [2009] suggested that a pre-flush of fresh water prior to the injection of CO_2 could significantly reduce and delay pressure build-up in the near well region. However, implementation of this strategy would depend on site specific geologic characteristics of the storage formation; if the storage formation has a high percentage of clay minerals, the freshwater pre-flush could have a negative impact due to clay swelling [*Pruess and Müller*, 2009]. Another approach presented by *Kim et al.* [2012] is to develop a skin zone around the injection well. *Kim et al.* [2012] showed that when a skin zone had a permeability 100 times greater than the storage reservoir, the bottom-hole pressure build-up was significantly reduced. A third method would be utilizing numerical studies of the injection activity to determine a minimum injection rate above which salt precipitation is minimized. The benefits of this method where highlighted in Section 2.4.3 Figure 7 (b and d) of this work.

Chapter 3 of this work focused on a method for risk quantification that are associated with geologic CO2 sequestration, mainly the risk of over-pressurizing the storage reservoir due to injection activities, and the risk of CO_2/brine leaking from the storage reservoir to an overlying formation. The first can be a significant risk when the injection activity occurs within a saline aquifer where no fluid production is occurring. During CO_2 injection if a significant risk of

over-pressurization is of concern, it could be managed by developing a brine production well within the storage reservoir to alleviate the over-pressure. However, this creates the additional challenge and cost of treating and/or managing the produced brine. *Roach et al.* [2014] evaluated under what conditions this additional challenge/cost is justified. The second risk addressed here, CO_2/brine leakage from the storage formation, must be considered for any storage formation (i.e. depleted oil and gas reservoirs or saline aquifers). This work addressed the first step in managing CO_2/brine leakage (i.e. detection of a leak) through the evaluation of "abnormal" pressure responses observed in an overlying aquifer unit, and then identifying the likelihoods of a high, medium, or low risk pathway (Section 3.5.6). If a leak is detected, the following step includes locating and further characterizing the leakage pathway through analytical or numerical modeling [*Réveillère et al.*, 2012]. Methods to do this rely on inverse modeling of the observed pressure response, and have been proposed by *Javandel et al.* [1988] and *Zeidouni and Pooladi-Darvish* [2010]. The last step in the management of a leaky reservoir is the determination of the proper corrective action. Possible actions include correcting the cause of the leakage such as reservoir overpressure [*Guénan and Rohmer*, 2011], modifying the leak pathway's permeability, or the application of a hydraulic barrier [*Réveillère et al.*, 2012].

With consideration of the previous and ongoing research efforts surrounding Carbon Capture and Geologic Storage, there appears to be strong support for the implementation of the technology to aid in the mitigation of anthropogenic CO2 emissions, and will likely be part of the future global climate change mitigation strategy.

Chapter 4 References

Guénan, T.L., and Rohmer, J. (2011), Corrective measures based on pressure control strategies for CO2 geological storage in deep aquifers, *International Journal of Greenhouse Gas Control*, *5*, 571-578, doi:http://dx.doi.org/10.1016/j.ijggc.2010.05.009.

Javandel, I., Tsang, C.F., Witherspoon, P.A., and Morganwalp, D. (1988), Hydrologic detection of abandoned wells near proposed injection wells for hazardous waste disposal, *Water Resources Research*, *24*(2), 261-270, doi:http://dx.doi.org/10.1029/WR024i002p00261.

Kim, K.-Y., Han, W.S., Oh, J., Kim, T., and Kim, J.-C. (2012), Characteristics of salt-precipitation and the associated pressure build-up during CO_2 storage in saline aquifers, *Transport in Porous Media*, *92*, 397-418, doi:10.1007/s11242-011-9909-4.

Pruess, K., and Müller, N. (2009), Formation dry-out from CO_2 injection into saline aquifers, *Water Resources Research*, *45*(3), doi:http://dx.doi.org/10.1029/2008WR007101.

Réveillère, A., Rohmer, J., and Manceau, J.-C. (2012), Hydraulic barrier design and applicability for managing the risk of CO2 leakage from deep saline aquifers, *International Journal of Greenhouse Gas Control*, *9*, 62-71, doi:http://dx.doi.org/10.1016/j.ijggc.2012.02.016.

Roach, J.D., Heath, J.E., Kobos, P.H., and Klise, G.T. (2014), System-level benefits of extracting and treating saline water from geologic formations during national-scale carbon capture and storage, *International Journal of Greenhouse Gas Control*, *25*, 186-197, doi:http://dx.doi.org/10.1016/j.ijggc.2014.04.012.

Zeidouni, M., and Pooladi-Darvish, M. (2010), Characterization of Leakage through Cap-Rock with Application to CO2 Storage in Aquifers - Single Injector and Single Monitoring Wel, in *Canadian Unconventional Resources and International Petroleum Conference*, edited, Society of Petroleum Engineers, Calgary, Alberta, Canada, doi:http://dx.doi.org/10.2118/138178-MS.

Appendix A: Idealized Scenario Data

Simulation	DoE Factor (coded values)				End of Injection ΔP [MPa]				End of Observation ΔP [MPa]			
	k_{IZ}	k_{SF}	k_{AZ}	C_p	**IZL**	**IZU**	**SF**	**AZ**	**IZL**	**IZU**	**SF**	**AZ**
1	-1	0	-1	+1	0.52881	0.53677	0.30552	0.10574	0.02558	-0.05847	-0.03240	-0.10245
2	0	-1	-1	-1	0.28053	0.23311	0.19602	-0.0003	0.01380	-0.07283	-0.00370	-0.00489
3	+1	-1	0	+1	0.19715	0.1223	0.1329	-0.0012	0.02168	-0.06298	-0.00736	-0.00346
4	0	+1	+1	+1	0.28812	0.23979	0.1438	0.01425	0.04442	-0.04169	-0.03722	-0.10417
5	-1	+1	0	-1	0.5087	0.51648	0.32101	0.14252	0.02791	-0.05658	-0.03298	-0.10769
6	+1	0	+1	-1	0.20093	0.1261	0.08334	-0.0283	0.04470	-0.03999	-0.03272	-0.07960
7	+1	+1	-1	0	0.20467	0.12951	0.08242	-0.0283	0.05076	-0.03403	-0.03889	-0.09828
8	-1	-1	+1	0	0.5406	0.54983	0.36162	0.00516	-0.00463	-0.08614	0.00311	-0.00830
9	0	0	0	0	0.2923	0.24496	0.1387	0.00137	0.03971	-0.04645	-0.03267	-0.09026

Table A1. DSD Training datasets for the end of injection (6 years) and end of observation (10 years).

Simulation	DoE Factor (coded values)				End of Injection ΔP [MPa]				End of Observation ΔP [MPa]			
	k_{IZ}	k_{SF}	k_{AZ}	C_p	IZL	IZU	SF	AZ	IZL	IZU	SF	AZ
1	0	+1	+1	0	0.28406	0.23581	0.14067	0.01137	0.04440	-0.04171	-0.03722	-0.10417
2	0	+1	-1	0	0.28406	0.23581	0.14067	0.01137	0.04440	-0.04171	-0.03722	-0.10417
3	-1	0	0	+1	0.52881	0.53677	0.30552	0.10574	0.02558	-0.05847	-0.03240	-0.10245
4	0	-1	0	+1	0.28872	0.24149	0.1973	-0.0003	0.01364	-0.07329	-0.00367	-0.00489
5	0	0	-1	-1	0.28185	0.23411	0.1323	-0.0026	0.03982	-0.04619	-0.03273	-0.09028
6	-1	0	+1	0	0.52829	0.53677	0.305	0.10457	0.02540	-0.05840	-0.03235	-0.10243
7	0	0	+1	+1	0.28776	0.23957	0.13577	0.00038	0.03987	-0.04615	-0.03279	-0.09029
8	+1	0	+1	0	0.20349	0.12862	0.08486	-0.0271	0.04470	-0.03998	-0.03272	-0.07960
9	0	+1	0	-1	0.28111	0.233	0.13822	0.00879	0.04439	-0.04171	-0.03723	-0.10417
10	+1	-1	0	0	0.1945	0.1196	0.13234	-0.0012	0.02168	-0.06298	-0.00737	-0.00346
11	+1	0	-1	0	0.20349	0.12862	0.08486	-0.0271	0.04470	-0.03998	-0.03272	-0.07960
12	-1	+1	0	0	0.51287	0.52049	0.3252	0.14741	0.02792	-0.05658	-0.03298	-0.10768
13	0	0	+1	-1	0.28185	0.23411	0.1323	-0.0026	0.03982	-0.04619	-0.03273	-0.09028
14	-1	-1	0	0	0.55559	0.56418	0.36873	0.00521	-0.00403	-0.08644	0.00301	-0.00830
15	0	0	0	0	0.2923	0.24496	0.1387	0.00137	0.03971	-0.04645	-0.03267	-0.09026
16	0	0	-1	+1	0.28776	0.23957	0.13577	0.00038	0.03987	-0.04615	-0.03279	-0.09029
17	0	0	0	0	0.2923	0.24496	0.1387	0.00137	0.03971	-0.04645	-0.03267	-0.09026
18	-1	0	0	-1	0.52238	0.53101	0.30162	0.10194	0.02537	-0.05841	-0.03236	-0.10244
19	1	0	0	+1	0.20556	0.13083	0.08612	-0.0263	0.04466	-0.04001	-0.03270	-0.07959
20	-1	0	-1	0	0.52829	0.53677	0.305	0.10457	0.02540	-0.05840	-0.03235	-0.10243
21	0	-1	-1	0	0.28589	0.23845	0.19712	-0.0003	0.01382	-0.07275	-0.00372	-0.00489
22	0	1	0	+1	0.28667	0.23847	0.14276	0.01336	0.04440	-0.04171	-0.03721	-0.10416
23	0	-1	0	-1	0.28053	0.23311	0.19602	-0.0003	0.01380	-0.07283	-0.00370	-0.00489
24	+1	+1	0	0	0.20343	0.12815	0.08135	-0.0291	0.05079	-0.03400	-0.03890	-0.09829
25	0	0	0	0	0.2923	0.24496	0.1387	0.00137	0.03971	-0.04645	-0.03267	-0.09026
26	0	-1	+1	0	0.28589	0.23845	0.19712	-0.0003	0.01382	-0.07275	-0.00372	-0.00489
27	+1	0	0	-1	0.20192	0.12711	0.08389	-0.0281	0.04469	-0.03999	-0.03272	-0.07960

Table A2. BBD training datasets for the end of injection (6 years) and end of observation (10 years).

Simulation	DoE Factor (coded values)				End of Injection ΔP [MPa]				End of Observation ΔP [MPa]			
	k_{IZ}	k_{SF}	k_{AZ}	C_p	IZL	IZU	SF	AZ	IZL	IZU	SF	AZ
1	-1	+1	-1	+1	0.52363	0.53126	0.33155	0.15175	0.02790	-0.05655	-0.03300	-0.10765
2	0	0	0	-1	0.28185	0.23411	0.13230	-0.00261	0.03982	-0.04619	-0.03273	-0.09028
3	0	-1	0	0	0.28589	0.23845	0.19712	-0.00032	0.01382	-0.07275	-0.00372	-0.00489
4	0	0	0	0	0.29230	0.24496	0.13870	0.00137	0.03971	-0.04645	-0.03267	-0.09026
5	+1	-1	-1	-1	0.19365	0.11903	0.13357	-0.00120	0.02163	-0.06303	-0.00735	-0.00346
6	-1	-1	-1	+1	0.55341	0.56198	0.36573	0.00512	-0.00398	-0.08644	0.00301	-0.00830
7	0	0	+1	0	0.29230	0.24496	0.13870	0.00137	0.03971	-0.04645	-0.03267	-0.09026
8	+1	+1	+1	-1	0.20024	0.12509	0.07903	-0.03120	0.05075	-0.03403	-0.03889	-0.09828
9	-1	0	0	0	0.52829	0.53677	0.30500	0.10457	0.02540	-0.05840	-0.03235	-0.10243
10	+1	-1	+1	+1	0.19715	0.12230	0.13290	-0.00119	0.02168	-0.06298	-0.00736	-0.00346
11	+1	+1	-1	-1	0.20024	0.12509	0.07903	-0.03120	0.05075	-0.03403	-0.03889	-0.09828
12	-1	-1	+1	-1	0.53238	0.54161	0.35854	0.00516	-0.00459	-0.08615	0.00311	-0.00830
13	0	0	0	0	0.29230	0.24496	0.13870	0.00137	0.03971	-0.04645	-0.03267	-0.09026
14	-1	-1	+1	+1	0.55341	0.56198	0.36573	0.00512	-0.00398	-0.08644	0.00301	-0.00830
15	-1	+1	+1	-1	0.50889	0.51636	0.31997	0.14125	0.02792	-0.05660	-0.03302	-0.10770
16	-1	-1	-1	-1	0.53238	0.54161	0.35854	0.00516	-0.00459	-0.08615	0.00311	-0.00830
17	0	0	0	+1	0.28776	0.23957	0.13577	0.00038	0.03987	-0.04615	-0.03279	-0.09029
18	-1	+1	-1	-1	0.50889	0.51636	0.31997	0.14125	0.02792	-0.05660	-0.03302	-0.10770
19	0	0	-1	0	0.29230	0.24496	0.13870	0.00137	0.03971	-0.04645	-0.03267	-0.09026
20	+1	0	0	0	0.20349	0.12862	0.08486	-0.02714	0.04470	-0.03998	-0.03272	-0.07960
21	+1	-1	-1	+1	0.19715	0.12230	0.13290	-0.00119	0.02168	-0.06298	-0.00736	-0.00346
22	+1	+1	+1	+1	0.20702	0.13204	0.08419	-0.02676	0.05070	-0.03407	-0.03887	-0.09827
23	-1	+1	+1	+1	0.52363	0.53126	0.33155	0.15175	0.02790	-0.05655	-0.03300	-0.10765
24	+1	+1	-1	+1	0.20702	0.13204	0.08419	-0.02676	0.05070	-0.03407	-0.03887	-0.09827
25	+1	-1	+1	-1	0.19365	0.11903	0.13357	-0.00120	0.02163	-0.06303	-0.00735	-0.00346
26	0	+1	0	0	0.28406	0.23581	0.14067	0.01137	0.04440	-0.04171	-0.03722	-0.10417

Table A3. CCD training datasets for the end of injection (6 years) and end of observation (10 years).

Simulation	DoE Factor (coded values)				End of Injection ΔP [MPa]				End of Observation ΔP [MPa]			
	k_{IZ}	k_{SF}	k_{AZ}	C_p	IZL	IZU	SF	AZ	IZL	IZU	SF	AZ
1	0.4359	-0.8974	0.6410	0.5385	0.24098	0.17995	0.13556	-0.00498	0.02347	-0.06176	-0.01101	-0.02212
2	-0.5897	-0.7949	-0.5897	-0.4359	0.38973	0.36953	0.19999	0.01114	0.01753	-0.07339	-0.01469	-0.04990
3	1.0000	0.2308	-0.1795	0.3846	0.20504	0.13024	0.08074	-0.02776	0.04667	-0.03803	-0.03443	-0.08596
4	0.9487	0.1282	0.4872	-0.2821	0.20622	0.13203	0.08338	-0.02728	0.04582	-0.03891	-0.03379	-0.08385
5	-0.6923	-0.5385	-0.3333	0.7949	0.41635	0.40211	0.22715	0.03016	0.02479	-0.06553	-0.02438	-0.07793
6	-0.8974	0.3846	-0.2308	-0.3333	0.48134	0.48081	0.28474	0.10095	0.02997	-0.05974	-0.03319	-0.10568
7	0.3846	-0.1795	-1.0000	-0.1282	0.24787	0.18831	0.11617	-0.01384	0.04053	-0.04488	-0.03094	-0.07996
8	0.3333	0.8974	0.2308	0.2821	0.24976	0.19099	0.11375	-0.00760	0.04701	-0.03879	-0.03830	-0.10154
9	-0.4872	-0.0769	1.0000	0.4359	0.37498	0.34884	0.19766	0.03235	0.03448	-0.05518	-0.03155	-0.09411
10	-0.6410	-0.1282	0.7949	-0.5385	0.40829	0.39092	0.22105	0.04362	0.03103	-0.06012	-0.03073	-0.09502
11	0.5897	1.0000	0.4359	-0.6410	0.22800	0.16184	0.09809	-0.01765	0.04863	-0.03699	-0.03874	-0.10085
12	-0.7949	-0.3333	-0.0256	-1.0000	0.44834	0.44108	0.23927	0.05004	0.02649	-0.06600	-0.02876	-0.09091
13	0.8974	-0.4359	-0.3846	-0.7949	0.20700	0.13390	0.08936	-0.02155	0.03846	-0.04679	-0.02525	-0.06144
14	0.0256	-0.6410	0.8974	-0.2308	0.28439	0.23631	0.13743	-0.00526	0.02993	-0.05603	-0.02092	-0.05735
15	-0.0256	-0.8462	-0.1282	0.1795	0.28665	0.24004	0.15370	-0.00309	0.02213	-0.06569	-0.01221	-0.03403
16	0.0769	-0.2821	0.2821	-0.7436	0.27765	0.22784	0.13671	-0.00595	0.03690	-0.04920	-0.02945	-0.07955
17	-0.8462	0.7949	0.8462	-0.8462	0.46028	0.45597	0.27425	0.10421	0.03140	-0.05996	-0.03391	-0.10725
18	0.7949	0.9487	-0.6410	0.0256	0.21510	0.14384	0.08986	-0.02384	0.04952	-0.03625	-0.03883	-0.09909
19	-1.0000	0.5385	0.0256	0.8462	0.51383	0.52184	0.31517	0.12980	0.02731	-0.05689	-0.03353	-0.10697
20	0.1795	0.2821	0.9487	-0.5897	0.26802	0.21431	0.12710	-0.00491	0.04307	-0.04383	-0.03454	-0.09474
21	-0.0769	0.6923	-0.4872	-0.1795	0.28984	0.24421	0.14210	0.00985	0.04269	-0.04543	-0.03702	-0.10230
22	-0.2308	0.5897	0.1795	-0.8974	0.31479	0.27619	0.15978	0.02013	0.04065	-0.04689	-0.03627	-0.10227
23	0.7436	-0.7436	0.3846	-0.3846	0.21439	0.14565	0.10355	-0.01246	0.03065	-0.05520	-0.01620	-0.03886
24	-0.2821	0.7436	0.6923	0.8974	0.33412	0.29784	0.17552	0.03378	0.04031	-0.04663	-0.03583	-0.10385
25	0.8462	-0.6923	-0.4359	0.1282	0.20807	0.13601	0.09568	-0.01495	0.03243	-0.05330	-0.01766	-0.04289
26	0.1282	-0.4872	-0.7949	0.6410	0.27358	0.22214	0.13423	-0.00717	0.03369	-0.05251	-0.02591	-0.06779
27	0.6923	-0.5897	-0.0769	0.9487	0.22155	0.15412	0.09885	-0.01566	0.03450	-0.05117	-0.02101	-0.05322
28	-0.1282	-0.2308	0.3333	1.0000	0.31342	0.27147	0.15605	0.00639	0.03590	-0.05195	-0.03016	-0.08433
29	-0.4359	0.0769	-0.9487	0.2308	0.35394	0.32465	0.18914	0.02883	0.03563	-0.05384	-0.03288	-0.09700
30	0.2821	-1.0000	-0.7436	-0.4872	0.24905	0.19205	0.17206	-0.00076	0.01623	-0.07047	-0.00505	-0.00438
31	-0.3846	0.6410	0.5897	-0.0769	0.34445	0.31268	0.18236	0.03725	0.03825	-0.05111	-0.03536	-0.10374
32	0.6410	0.1795	0.7436	0.5897	0.22566	0.15903	0.09445	-0.02057	0.04471	-0.04087	-0.03388	-0.08810
33	-0.1795	0.4359	-0.2821	0.6923	0.31485	0.27412	0.16260	0.01833	0.04070	-0.04717	-0.03629	-0.10022
34	-0.5385	-0.9487	0.5385	0.4872	0.38600	0.36349	0.23453	0.00415	0.00936	-0.08142	-0.00533	-0.02011
35	-0.9487	0.8462	-0.6923	0.3333	0.48981	0.49275	0.29715	0.12669	0.02875	-0.05745	-0.03239	-0.10756
36	-0.3333	0.0256	-0.8462	-0.6923	0.33463	0.30107	0.17261	0.01835	0.03584	-0.05310	-0.03222	-0.09470
37	-0.7436	-0.3846	0.1282	-0.0256	0.43283	0.42159	0.22956	0.04225	0.02695	-0.06576	-0.02840	-0.08782
38	0.5385	0.3333	-0.8974	0.7436	0.23663	0.17134	0.10246	-0.01645	0.04539	-0.04009	-0.03482	-0.09239
39	0.2308	-0.0256	0.0769	0.0769	0.26279	0.20725	0.12010	-0.00899	0.04089	-0.04593	-0.03259	-0.08694
40	0.4872	0.4872	-0.5385	-0.9487	0.23510	0.17170	0.10464	-0.01721	0.04595	-0.03943	-0.03591	-0.09551

Table A4. LHC training datasets for the end of injection (6 years) and end of observation (10 years).

Simulation	DoE Factor (coded values)				End of Injection ΔP [MPa]				End of Observation ΔP [MPa]			
	k_{IZ}	**k_{SF}**	**k_{AZ}**	**C_p**	**IZL**	**IZU**	**SF**	**AZ**	**IZL**	**IZU**	**SF**	**AZ**
1	0.3467	-0.0909	-0.3067	0.5686	0.2488	0.1903	0.1142	-0.0133	0.0409	-0.0453	-0.0317	-0.0835
2	-0.2800	-0.5071	0.0400	-0.8518	0.3287	0.2929	0.1710	0.0051	0.0302	-0.0565	-0.0255	-0.0726
3	0.2400	0.5697	0.1200	-0.2118	0.2597	0.2035	0.1235	-0.0058	0.0447	-0.0421	-0.0370	-0.0987
4	0.6267	0.7657	-0.6933	-0.9932	0.2244	0.1579	0.0980	-0.0203	0.0480	-0.0377	-0.0379	-0.0982
5	0.9467	0.1980	-0.1467	-0.6216	0.2055	0.1314	0.0814	-0.0281	0.0464	-0.0384	-0.0343	-0.0856
6	0.3067	-0.7030	0.6667	-0.7149	0.2526	0.1956	0.1209	-0.0091	0.0293	-0.0573	-0.0178	-0.0478
7	-0.7600	-0.5879	-0.0933	-0.7227	0.4398	0.4299	0.2419	0.0331	0.0227	-0.0708	-0.0230	-0.0757
8	-0.4667	0.8000	-0.2267	0.1961	0.3554	0.3270	0.1968	0.0468	0.0384	-0.0512	-0.0359	-0.1053
9	-0.4800	0.5253	0.5467	0.8039	0.3659	0.3385	0.1962	0.0460	0.0377	-0.0520	-0.0352	-0.1035
10	-0.6933	-0.4303	-0.1333	-0.5569	0.4217	0.4082	0.2255	0.0351	0.0267	-0.0636	-0.0273	-0.0845
11	-0.3067	0.3455	0.3867	-0.0353	0.3301	0.2945	0.1738	0.0240	0.0387	-0.0480	-0.0357	-0.1001
12	-0.7600	0.3293	0.8933	-0.2471	0.4395	0.4288	0.2470	0.0765	0.0324	-0.0605	-0.0338	-0.1043
13	-0.8133	-0.1859	0.4133	-0.4706	0.4620	0.4553	0.2578	0.0634	0.0279	-0.0642	-0.0300	-0.0961
14	0.2129	-0.8706	-0.9695	0.1297	0.2576	0.2024	0.1411	-0.0050	0.0231	-0.0638	-0.0117	-0.0280
15	-0.9827	-0.9989	0.8400	-0.0392	0.5314	0.5388	0.3542	0.0051	-0.0032	-0.0868	0.0027	-0.0086
16	0.1733	-0.2222	0.4400	-0.5137	0.2661	0.2128	0.1280	-0.0090	0.0385	-0.0482	-0.0303	-0.0808
17	-0.9600	0.8283	0.1200	-0.5569	0.4945	0.4987	0.2994	0.1268	0.0284	-0.0572	-0.0323	-0.1076
18	-0.8267	0.1172	0.3867	-0.9974	0.4526	0.4474	0.2552	0.0740	0.0295	-0.0618	-0.0336	-0.1024
19	-0.5333	0.8000	0.4667	-0.4627	0.3760	0.3522	0.2128	0.0568	0.0380	-0.0515	-0.0362	-0.1059
20	-0.1867	-0.0990	-0.2800	-0.6502	0.3082	0.2680	0.1496	0.0060	0.0370	-0.0506	-0.0317	-0.0897
21	-0.3333	0.7657	0.4667	0.8784	0.3376	0.3035	0.1801	0.0367	0.0395	-0.0487	-0.0357	-0.1043
22	0.7733	-0.7535	0.5733	0.0471	0.2152	0.1457	0.1046	-0.0121	0.0304	-0.0555	-0.0159	-0.0375
23	-0.3086	-0.9837	-0.6481	0.8265	0.3431	0.3087	0.2235	0.0008	0.0105	-0.0778	-0.0039	-0.0098
24	-0.6827	-0.9883	0.2333	-0.8647	0.4262	0.4123	0.2809	0.0034	0.0043	-0.0858	-0.0013	-0.0105
25	0.2936	-0.8283	-0.1947	0.5097	0.2528	0.1958	0.1328	-0.0064	0.0249	-0.0618	-0.0133	-0.0332

Table A5. Validation (1-15) and Test (16-25) datasets for the end of injection (6 years) and end of observation (10 years).

Appendix B: Complex Scenario Data

Simulation	Time 1: 0.05 years ΔP [MPa]				Time 2: 0.5 years ΔP [MPa]				Time 3: 5.0 years ΔP [MPa]			
	IZL	**IZU**	**SF**	**AZ**	**IZL**	**IZU**	**SF**	**AZ**	**IZL**	**IZU**	**SF**	**AZ**
1	1.8040	1.4921	1.1100	0.5989	2.4090	2.0958	1.7111	1.1738	2.2849	2.1995	1.5134	1.1380
2	0.7526	0.4432	0.4117	0.2911	1.6537	1.3477	1.3505	1.2253	1.5595	1.2988	1.4215	1.3596
3	2.0817	1.7714	0.8955	0.0327	2.8008	2.4887	1.5968	0.4884	2.6227	2.5392	1.2761	0.4925
4	1.8205	1.5085	1.1002	0.5594	2.4377	2.1243	1.7051	1.1283	2.3383	2.2520	1.4494	1.0522
5	0.7648	0.4554	0.3959	0.2432	1.6578	1.3518	1.3363	1.1934	1.5625	1.3011	1.3441	1.2396
6	0.4869	0.1776	0.1164	-0.0526	0.4889	0.1832	0.1388	-0.0524	0.3202	0.0577	0.0869	-0.0555
7	0.8385	0.5290	0.2777	0.0191	1.8061	1.5000	1.2458	0.8491	1.7251	1.4639	1.2018	0.9090
8	1.0022	0.6926	0.5091	0.2265	1.1559	0.8455	0.6805	0.3911	0.8353	0.6467	0.5851	0.4073
9	1.5791	1.2693	1.0865	1.0225	2.1502	1.8403	1.8654	1.8085	1.7417	1.5843	1.7016	1.6401
10	1.0023	0.6927	0.5097	0.2272	1.1553	0.8449	0.6800	0.3908	0.8450	0.6562	0.5864	0.4073
11	1.8288	1.5167	1.1102	0.5736	3.2780	2.9646	2.5643	2.0114	3.5007	3.4056	2.6041	2.2081
12	1.8695	1.5588	1.0533	0.4508	2.5438	2.2314	1.7236	1.0488	2.3458	2.2631	1.6118	1.2028
13	0.4809	0.1715	0.1328	0.0033	0.4849	0.1792	0.1682	0.0133	0.3158	0.0533	0.1894	0.1348
14	2.0749	1.7646	0.9081	0.0747	3.6885	3.3763	2.3986	1.2135	3.8757	3.7830	2.3248	1.4672
15	0.8000	0.4906	0.3811	0.3200	1.7539	1.4474	1.4305	1.2948	1.6663	1.3982	1.5344	1.4768
16	0.5233	0.2139	0.1835	0.0528	0.5336	0.2279	0.2231	0.0778	0.3676	0.1050	0.1788	0.0869
17	1.1050	0.7953	0.5777	0.2832	2.2048	1.8937	1.7121	1.4088	2.0333	1.8414	1.7465	1.5542
18	0.4796	0.1702	0.1516	0.0299	0.4836	0.1778	0.1771	0.0417	0.3197	0.0571	0.1219	0.0246
19	1.5682	1.2581	1.2053	1.0717	3.0200	2.7099	2.7405	2.6782	2.9903	2.8316	2.8740	2.7983
20	1.0284	0.7188	0.4751	0.1206	1.1766	0.8662	0.6395	0.2797	0.8671	0.6780	0.4796	0.2416
21	0.4717	0.1624	0.2015	0.1478	0.4771	0.1713	0.2398	0.1765	0.3180	0.0534	0.2150	0.1908
22	0.9870	0.6774	0.4953	0.2111	1.1144	0.8041	0.6370	0.3452	0.7912	0.6017	0.5365	0.3596
23	1.0095	0.6999	0.5068	0.2111	1.1643	0.8539	0.6676	0.3545	0.8416	0.6499	0.5717	0.3820
24	0.9634	0.6539	0.5690	0.4003	1.1246	0.8143	0.7421	0.5585	0.8051	0.6167	0.7324	0.6710
25	1.0154	0.7058	0.4852	0.1601	1.1683	0.8579	0.6560	0.3245	0.8539	0.6650	0.5160	0.2954
26	0.9816	0.6718	0.5527	0.3233	1.1387	0.8281	0.7128	0.4801	0.8440	0.6546	0.6052	0.4632
27	1.0141	0.7046	0.4564	0.1805	1.1655	0.8552	0.6621	0.3413	0.8471	0.6577	0.5773	0.3839
28	1.9821	1.6719	0.9517	0.3198	3.4676	3.1556	2.5505	1.7919	3.5973	3.5068	2.7528	2.1553

Table B1. Training response data for Monitoring Location #1, Table 6 presents the remainder of the training dataset.

Simulation	Time 1: 0.05 years ΔP [MPa]				Time 2: 0.5 years ΔP [MPa]				Time 3: 5.0 years ΔP [MPa]			
	IZL	**IZU**	**SF**	**AZ**	**IZL**	**IZU**	**SF**	**AZ**	**IZL**	**IZU**	**SF**	**AZ**
1	0.8721	0.5622	0.5230	0.3955	1.4196	1.1096	1.0717	0.9282	1.5479	1.2369	1.1666	0.9860
2	0.6363	0.3269	0.3435	0.2775	1.5378	1.2281	1.2591	1.1942	1.5679	1.2587	1.3847	1.3562
3	1.0594	0.7497	0.3653	0.0046	1.7068	1.3969	0.9934	0.4340	1.8544	1.5460	1.0827	0.4550
4	0.8997	0.5896	0.5112	0.3392	1.4599	1.1496	1.0623	0.8624	1.6070	1.2955	1.1490	0.8817
5	0.6496	0.3402	0.3203	0.2126	1.5425	1.2328	1.2422	1.1527	1.5731	1.2639	1.3018	1.2114
6	0.3626	0.0533	0.0474	-0.0599	0.3681	0.0587	0.0507	-0.0597	0.3282	0.0192	0.0556	-0.0603
7	0.7221	0.4127	0.2150	0.0158	1.6899	1.3802	1.1667	0.8334	1.7344	1.4251	1.1988	0.8964
8	0.6477	0.3382	0.2876	0.1552	0.7808	0.4714	0.4433	0.3103	0.7670	0.4591	0.4568	0.3244
9	0.8463	0.5367	0.4697	0.4714	1.4073	1.0977	1.1324	1.0781	1.3375	1.0280	1.2341	1.3174
10	0.6482	0.3387	0.2882	0.1558	0.7805	0.4710	0.4430	0.3100	0.7691	0.4611	0.4571	0.3243
11	0.9129	0.6028	0.5262	0.3591	2.3322	2.0218	1.9449	1.7589	2.7323	2.4211	2.2905	2.0408
12	0.9167	0.6069	0.4817	0.2971	1.5328	1.2229	1.0932	0.8458	1.6511	1.3406	1.2175	0.9764
13	0.3565	0.0471	0.0673	0.0007	0.3639	0.0546	0.0804	0.0087	0.3232	0.0142	0.1528	0.1349
14	1.0623	0.7525	0.3788	0.0396	2.6375	2.3273	1.8136	1.1517	3.0759	2.7646	2.1841	1.4210
15	0.6933	0.3838	0.2567	0.1594	1.6463	1.3366	1.2735	1.1126	1.6769	1.3675	1.4107	1.3053
16	0.4007	0.0913	0.1062	0.0270	0.4140	0.1047	0.1267	0.0508	0.3760	0.0670	0.1380	0.0603
17	0.7629	0.4534	0.3620	0.2107	1.8473	1.5376	1.4810	1.3200	1.9587	1.6504	1.6157	1.4605
18	0.3570	0.0477	0.0701	-0.0048	0.3642	0.0548	0.0787	0.0048	0.3274	0.0184	0.0793	0.0016
19	0.8496	0.5400	0.5639	0.5105	2.2979	1.9881	2.0350	1.9892	2.5555	2.2460	2.3913	2.4289
20	0.6681	0.3587	0.2648	0.0806	0.7960	0.4865	0.4137	0.2295	0.7843	0.4764	0.3922	0.2112
21	0.3542	0.0449	0.0859	0.0327	0.3618	0.0525	0.0988	0.0499	0.3263	0.0174	0.1215	0.0742
22	0.6313	0.3218	0.2724	0.1387	0.7390	0.4295	0.3990	0.2632	0.7193	0.4114	0.4090	0.2759
23	0.6590	0.3495	0.2773	0.1187	0.7908	0.4814	0.4262	0.2625	0.7738	0.4659	0.4332	0.2798
24	0.6186	0.3092	0.3304	0.2794	0.7582	0.4488	0.4880	0.4319	0.7300	0.4219	0.5689	0.5740
25	0.6534	0.3440	0.2781	0.1284	0.7864	0.4769	0.4322	0.2803	0.7718	0.4638	0.4265	0.2696
26	0.6342	0.3247	0.3173	0.2157	0.7703	0.4608	0.4623	0.3630	0.7647	0.4567	0.4646	0.3600
27	0.6569	0.3475	0.2476	0.1245	0.7877	0.4782	0.4306	0.2757	0.7698	0.4619	0.4596	0.3085
28	0.9440	0.6343	0.4298	0.3197	2.3940	2.0840	1.9670	1.7582	2.8012	2.4907	2.3700	2.1300

Table B2. Training response data for Monitoring Location #2, Table 6 presents the remainder of the training dataset.

Simulation	Time 1: 0.05 years ΔP [MPa]				Time 2: 0.5 years ΔP [MPa]				Time 3: 5.0 years ΔP [MPa]			
	IZL	**IZU**	**SF**	**AZ**	**IZL**	**IZU**	**SF**	**AZ**	**IZL**	**IZU**	**SF**	**AZ**
1	0.5268	0.2174	0.2540	0.2075	0.9967	0.6872	0.7253	0.6679	1.0690	0.7595	0.7953	0.7351
2	0.5857	0.2763	0.2973	0.2361	1.4790	1.1694	1.2020	1.1391	1.5375	1.2278	1.3036	1.2793
3	0.6299	0.3204	0.1484	-0.0195	1.1712	0.8615	0.6775	0.3668	1.2644	0.9547	0.7404	0.3946
4	0.5474	0.2378	0.2439	0.1643	1.0268	0.7171	0.7176	0.6173	1.1117	0.8018	0.7824	0.6593
5	0.5981	0.2887	0.2801	0.1853	1.4832	1.1735	1.1888	1.1059	1.5445	1.2352	1.2563	1.1686
6	0.2989	-0.0104	0.0096	-0.0682	0.3028	-0.0065	0.0122	-0.0675	0.3010	-0.0078	0.0215	-0.0672
7	0.6694	0.3600	0.1860	0.0113	1.6299	1.3202	1.1215	0.8049	1.7058	1.3965	1.1994	0.8703
8	0.4836	0.1743	0.1652	0.0768	0.5984	0.2891	0.3020	0.2159	0.6103	0.3009	0.3139	0.2269
9	0.5349	0.2254	0.2092	0.2189	1.0263	0.7168	0.7566	0.7046	1.0058	0.6963	0.8444	0.8819
10	0.4841	0.1748	0.1658	0.0774	0.5982	0.2888	0.3018	0.2157	0.6110	0.3016	0.3140	0.2268
11	0.5706	0.2611	0.2694	0.1964	1.9160	1.6061	1.6187	1.5341	2.2509	1.9408	1.9358	1.8290
12	0.5584	0.2489	0.2237	0.1408	1.0930	0.7833	0.7517	0.6151	1.1771	0.8675	0.8389	0.7053
13	0.2941	-0.0152	0.0249	-0.0232	0.2997	-0.0096	0.0344	-0.0165	0.2946	-0.0142	0.0861	0.0790
14	0.6470	0.3375	0.1662	0.0129	2.1330	1.8230	1.5129	1.0817	2.5132	2.2031	1.8528	1.3517
15	0.6446	0.3352	0.2044	0.0941	1.5904	1.2807	1.1977	1.0136	1.6498	1.3403	1.3141	1.1798
16	0.3391	0.0298	0.0601	-0.0020	0.3502	0.0409	0.0784	0.0201	0.3488	0.0398	0.0907	0.0268
17	0.6186	0.3092	0.2502	0.1333	1.6778	1.3681	1.3402	1.2118	1.8076	1.4978	1.4760	1.3477
18	0.2951	-0.0142	0.0215	-0.0383	0.3005	-0.0088	0.0282	-0.0308	0.2993	-0.0097	0.0367	-0.0294
19	0.5561	0.2467	0.2910	0.2557	1.9332	1.6235	1.6812	1.6445	2.2165	1.9070	2.0099	2.0104
20	0.4961	0.1867	0.1560	0.0411	0.6065	0.2971	0.2863	0.1731	0.6209	0.3115	0.2912	0.1665
21	0.2939	-0.0154	0.0273	-0.0245	0.2997	-0.0096	0.0361	-0.0133	0.2981	-0.0109	0.0502	-0.0004
22	0.4653	0.1560	0.1480	0.0585	0.5566	0.2472	0.2569	0.1670	0.5648	0.2555	0.2665	0.1766
23	0.4907	0.1813	0.1616	0.0599	0.6039	0.2945	0.2930	0.1905	0.6144	0.3050	0.3050	0.2032
24	0.4668	0.1575	0.1858	0.1392	0.5865	0.2771	0.3265	0.2804	0.5842	0.2749	0.3700	0.3625
25	0.4838	0.1744	0.1663	0.0790	0.5986	0.2892	0.3013	0.2142	0.6119	0.3025	0.3080	0.2124
26	0.4745	0.1652	0.1851	0.1139	0.5924	0.2830	0.3123	0.2447	0.6060	0.2966	0.3218	0.2495
27	0.4907	0.1813	0.1373	0.0583	0.6031	0.2937	0.2938	0.1932	0.6130	0.3037	0.3102	0.2153
28	0.5527	0.2432	0.2156	0.2474	1.9217	1.6119	1.6595	1.6317	2.2774	1.9676	2.0276	1.9905

Table B3. Training response data for Monitoring Location #3, Table 6 presents the remainder of the training dataset.

Simulation	DoE Factor (coded values)				
	kIZ	**kSF**	**kL**	**LL**	**kF**
1	0.2007	-0.3704	-0.2408	-1	0.1941
2	-0.8300	0.4535	-0.3619	0	-0.1388
3	0.0540	-0.5910	-0.1736	0	-0.8104
4	-0.7623	0.3562	-0.8027	-1	-0.0981
5	-0.5118	0.3571	-0.8523	+1	-0.0944
6	0.4253	-0.8169	0.9632	0	0.6540
7	-0.4943	0.2298	-0.8923	0	0.7685
8	0.5345	-0.3679	-0.7183	-1	0.4012
9	-0.9003	-0.8450	0.7869	0	-0.5163
10	0.4934	-0.2590	-0.0111	-1	-0.4451
11	0.9545	0.2448	-0.8644	+1	-0.9878
12	-0.2322	0.9951	0.7953	+1	-0.2506
13	-0.4796	0.0347	-0.4229	+1	-0.1261
14	0.7549	0.9810	-0.4619	0	-0.3914
15	0.6122	-0.5469	0.1884	-1	-0.4183
16	-0.0778	-0.2040	-0.0482	-1	-0.5150
17	-0.8181	0.3931	-0.2634	+1	0.8734
18	-0.6252	0.4953	0.8764	0	-0.2055
19	0.0634	-0.1592	0.2409	+1	-0.0412
20	-0.9980	-0.7900	-1.1748	0	-0.9809
21	-0.7368	-0.1006	0.5144	-1	-0.9048
22	-0.9958	-0.8388	-0.3667	0	-0.9819
23	0.8447	0.0315	0.9721	-1	0.4614
24	-0.8928	0.5813	0.4364	+1	-0.4776
25	-0.2397	-0.8950	0.4691	0	0.2801
26	0.6257	0.6023	0.2746	-1	-0.7359
27	0.7688	0.8920	-0.7590	0	0.3044
28	-0.2437	0.8169	-0.0064	0	-0.3838
29	-0.5022	0.0199	-0.9552	+1	-0.1953
30	0.3706	0.7012	-0.0684	-1	0.5197
31	0.2406	-0.7109	0.1217	+1	-0.4181
32	0.1285	-0.8707	0.3112	+1	0.7204
33	-0.2899	0.6226	-0.4343	-1	0.1300
34	-0.9884	0.9110	0.9974	0	-0.9677
35	-0.9952	0.8298	0.9723	-1	-0.9040

Table B4. Random simulations utilized in the Validation (1-22) and Test (23-35) datasets.

Simulation	Time 1: 0.05 years ΔP [MPa]				Time 2: 0.5 years ΔP [MPa]				Time 3: 5.0 years ΔP [MPa]			
	IZL	**IZU**	**SF**	**AZ**	**IZL**	**IZU**	**SF**	**AZ**	**IZL**	**IZU**	**SF**	**AZ**
1	0.8878	0.5783	0.3857	0.0924	0.9768	0.6687	0.4875	0.1782	0.7009	0.4933	0.3694	0.1665
2	1.7014	1.3906	0.9543	0.3960	2.2708	1.9583	1.5185	0.9185	2.0357	1.9404	1.2622	0.8605
3	1.0868	0.7772	0.4994	0.1735	1.7310	1.4206	1.1827	0.8126	1.4508	1.2564	1.0789	0.8312
4	1.6661	1.3555	0.8997	0.3193	2.1796	1.8672	1.4072	0.7832	1.9078	1.8071	1.1293	0.7233
5	1.4228	1.1127	0.7485	0.2635	1.7876	1.4755	1.1193	0.6121	1.4171	1.2860	0.8727	0.5504
6	0.7168	0.4074	0.3570	0.2388	0.7675	0.4624	0.4362	0.2880	0.5152	0.2905	0.4358	0.3957
7	1.4084	1.0983	0.7219	0.2259	1.7202	1.4081	1.0415	0.5224	1.3806	1.2478	0.7937	0.4645
8	0.6933	0.3839	0.2563	0.0223	0.7269	0.4223	0.3124	0.0674	0.4909	0.2577	0.2073	0.0494
9	1.6749	1.3649	0.9867	0.6651	2.4172	2.1053	1.8131	1.3907	2.0736	1.9891	1.8511	1.6455
10	0.8072	0.4977	0.3572	0.1284	0.9505	0.6453	0.5253	0.2741	0.6986	0.4679	0.4476	0.2973
11	0.8030	0.4936	0.3611	0.1459	1.6873	1.3814	1.3083	1.1036	1.5892	1.3298	1.3045	1.1473
12	1.1457	0.8357	0.6664	0.3840	1.4266	1.1148	0.9488	0.6588	1.1000	0.9334	0.7980	0.6106
13	1.4158	1.1058	0.7133	0.2067	1.7681	1.4561	1.0742	0.5377	1.4199	1.2856	0.8547	0.4966
14	0.6765	0.3670	0.3176	0.1661	0.7619	0.4570	0.4286	0.2714	0.5604	0.3129	0.3506	0.2445
15	0.7520	0.4426	0.3291	0.1397	0.8637	0.5588	0.4753	0.2588	0.6507	0.4100	0.4400	0.3202
16	1.1118	0.8021	0.5502	0.2095	1.4465	1.1355	0.8934	0.5174	1.1069	0.9217	0.7888	0.5611
17	1.7101	1.3994	0.9321	0.3399	2.2132	1.9007	1.4305	0.7955	1.9028	1.8059	1.1463	0.7442
18	1.4021	1.0920	0.9022	0.6180	1.8483	1.5363	1.3610	1.0609	1.4808	1.3668	1.3387	1.2101
19	0.9719	0.6623	0.4635	0.1675	1.1127	0.8031	0.6239	0.3180	0.8058	0.6107	0.5021	0.2998
20	2.0595	1.7491	0.9380	0.0982	3.5868	3.2746	2.3928	1.3093	3.7429	3.6508	2.3250	1.5244
21	1.4947	1.1848	0.9765	0.7178	2.6050	2.2947	2.2236	2.0477	2.4197	2.2683	2.2830	2.1639
22	2.0063	1.6960	0.9506	0.2072	3.5121	3.1999	2.4376	1.4945	3.6805	3.5890	2.4436	1.7497
23	0.5340	0.2246	0.2538	0.1937	0.5466	0.2414	0.3075	0.2469	0.3672	0.1107	0.2754	0.2518
24	1.7535	1.4425	1.0158	0.4664	2.4731	2.1605	1.7376	1.1567	2.2697	2.1805	1.5456	1.1523
25	1.1346	0.8250	0.6106	0.3888	1.3526	1.0409	0.8845	0.6058	0.9842	0.8189	0.8534	0.7315
26	0.8050	0.4955	0.4272	0.2676	1.1820	0.8767	0.8398	0.6785	0.9862	0.7442	0.8030	0.7080
27	0.5791	0.2697	0.2279	0.0810	0.5982	0.2935	0.2657	0.1075	0.4034	0.1556	0.1922	0.0834
28	1.1691	0.8591	0.6766	0.3831	1.4971	1.1853	1.0113	0.7123	1.1846	1.0198	0.8861	0.7089
29	1.4415	1.1315	0.7176	0.1900	1.8230	1.5109	1.1048	0.5406	1.4854	1.3541	0.8732	0.4937
30	0.7586	0.4491	0.3647	0.1729	0.8170	0.5108	0.4285	0.2242	0.5618	0.3398	0.3279	0.2009
31	0.9190	0.6095	0.3956	0.1240	1.1005	0.7930	0.6256	0.3314	0.8292	0.6186	0.5108	0.3156
32	0.9155	0.6060	0.3904	0.1139	1.0135	0.7047	0.5254	0.2191	0.7118	0.5125	0.4160	0.2184
33	1.2067	0.8967	0.6537	0.2931	1.4513	1.1395	0.9021	0.5303	1.1024	0.9421	0.6995	0.4650
34	1.7032	1.3921	1.1408	0.7831	3.0777	2.7652	2.5285	2.1623	3.1150	3.0248	2.7943	2.5880
35	1.5736	1.2635	1.2006	1.0616	2.8306	2.5204	2.5491	2.4844	2.6807	2.5236	2.5735	2.4988

Table B5. Validation and Test response data at Monitoring Location #1, Table S9 provides the remainder of the dataset.

Simulation	Time 1: 0.05 years ΔP [MPa]				Time 2: 0.5 years ΔP [MPa]				Time 3: 5.0 years ΔP [MPa]			
	IZL	**IZU**	**SF**	**AZ**	**IZL**	**IZU**	**SF**	**AZ**	**IZL**	**IZU**	**SF**	**AZ**
1	0.5970	0.2876	0.2105	0.0475	0.6702	0.3608	0.3025	0.1349	0.6451	0.3367	0.2966	0.1295
2	0.8890	0.5792	0.4611	0.2570	1.4096	1.0996	0.9800	0.7432	1.5351	1.2285	1.0387	0.7422
3	0.7578	0.4483	0.3036	0.1256	1.3830	1.0733	0.9666	0.7461	1.3980	1.0899	0.9855	0.7626
4	0.8950	0.5852	0.4396	0.2058	1.3649	1.0550	0.9080	0.6397	1.4739	1.1687	0.9428	0.6332
5	0.8191	0.5094	0.3885	0.1773	1.1505	0.8408	0.7307	0.5038	1.1962	0.8903	0.7196	0.4853
6	0.4923	0.1830	0.2046	0.1606	0.5327	0.2234	0.2642	0.2100	0.4904	0.1817	0.3301	0.3251
7	0.8114	0.5017	0.3692	0.1472	1.0910	0.7813	0.6612	0.4230	1.1413	0.8352	0.6508	0.4038
8	0.4878	0.1785	0.1383	0.0032	0.5147	0.2053	0.1779	0.0455	0.4723	0.1634	0.1703	0.0368
9	0.8290	0.5195	0.4776	0.4791	1.5237	1.2141	1.2325	1.1574	1.5694	1.2596	1.4121	1.4555
10	0.5999	0.2905	0.2222	0.0747	0.7315	0.4221	0.3783	0.2273	0.6928	0.3840	0.3792	0.2399
11	0.6811	0.3717	0.2886	0.1295	1.5647	1.2551	1.2167	1.0739	1.5968	1.2876	1.2567	1.1254
12	0.6995	0.3900	0.3830	0.2857	0.9536	0.6440	0.6438	0.5426	0.9630	0.6557	0.6570	0.5469
13	0.8243	0.5147	0.3723	0.1475	1.1429	0.8332	0.7052	0.4579	1.1896	0.8836	0.7048	0.4483
14	0.5196	0.2102	0.2130	0.1210	0.6012	0.2919	0.3061	0.2213	0.5634	0.2544	0.3005	0.2129
15	0.5708	0.2615	0.2023	0.0729	0.6742	0.3648	0.3336	0.1974	0.6351	0.3262	0.3540	0.2351
16	0.7359	0.4264	0.3105	0.1231	1.0437	0.7341	0.6383	0.4284	1.0310	0.7232	0.6482	0.4575
17	0.8933	0.5835	0.4490	0.2275	1.3477	1.0377	0.9037	0.6504	1.4481	1.1424	0.9488	0.6551
18	0.7668	0.4573	0.4727	0.4161	1.1782	0.8687	0.8970	0.8284	1.1966	0.8887	1.0125	1.0304
19	0.6324	0.3230	0.2735	0.1466	0.7546	0.4452	0.4173	0.2846	0.7341	0.4260	0.4212	0.2809
20	1.0511	0.7413	0.4004	0.0581	2.5426	2.2324	1.8053	1.2351	2.9514	2.6402	2.1405	1.4698
21	0.8525	0.5429	0.4760	0.3668	1.9635	1.6537	1.6575	1.5664	2.0839	1.7740	1.8792	1.8821
22	1.0153	0.7056	0.4108	0.1386	2.4828	2.1756	1.8445	1.3860	2.9076	2.5965	2.1918	1.6294
23	0.3950	0.0856	0.1228	0.0693	0.4071	0.0978	0.1503	0.1070	0.3712	0.0624	0.1729	0.1303
24	0.8830	0.5732	0.4970	0.3391	1.5525	1.2426	1.1726	0.9927	1.6828	1.3749	1.2722	1.0527
25	0.6880	0.3786	0.3308	0.2733	0.8777	0.5683	0.5728	0.4775	0.8623	0.5547	0.6563	0.6158
26	0.6321	0.3227	0.2950	0.1817	1.0001	0.6906	0.6905	0.5895	0.9717	0.6628	0.6999	0.6085
27	0.4217	0.1123	0.1251	0.0403	0.4389	0.1296	0.1463	0.0642	0.4034	0.0945	0.1421	0.0567
28	0.7232	0.4136	0.3828	0.2620	1.0231	0.7135	0.6957	0.5743	1.0444	0.7372	0.7094	0.5822
29	0.8367	0.5271	0.3691	0.1281	1.1848	0.8751	0.7274	0.4575	1.2399	0.9339	0.7217	0.4426
30	0.5197	0.2104	0.2022	0.0974	0.5666	0.2572	0.2553	0.1520	0.5319	0.2233	0.2443	0.1427
31	0.6395	0.3301	0.2467	0.1206	0.8059	0.4964	0.4585	0.3145	0.7818	0.4733	0.4620	0.3053
32	0.5943	0.2849	0.2209	0.1100	0.6763	0.3669	0.3380	0.2042	0.6509	0.3426	0.3514	0.2101
33	0.7309	0.4213	0.3523	0.1892	0.9470	0.6374	0.5801	0.4135	0.9603	0.6532	0.5588	0.3906
34	0.8375	0.5279	0.5536	0.5034	2.1803	1.8704	1.9017	1.8390	2.4714	2.1619	2.2790	2.2925
35	0.8512	0.5416	0.5613	0.5073	2.1012	1.7914	1.8392	1.7937	2.2468	1.9374	2.0912	2.1362

Table B6. Validation and Test response data at Monitoring Location #2, Table S9 provides the remainder of the datasets.

Simulation	Time 1: 0.05 years ΔP [MPa]				Time 2: 0.5 years ΔP [MPa]				Time 3: 5.0 years ΔP [MPa]			
	IZL	**IZU**	**SF**	**AZ**	**IZL**	**IZU**	**SF**	**AZ**	**IZL**	**IZU**	**SF**	**AZ**
1	0.4537	0.1443	0.1211	0.0163	0.5153	0.2059	0.2018	0.0960	0.5237	0.2143	0.2059	0.0946
2	0.5621	0.2526	0.2308	0.1309	1.0156	0.7060	0.6847	0.5597	1.0930	0.7833	0.7362	0.5814
3	0.6129	0.3034	0.2047	0.0721	1.2139	0.9043	0.8368	0.6607	1.2536	0.9440	0.8697	0.6814
4	0.5719	0.2624	0.2248	0.1083	0.9812	0.6716	0.6352	0.4926	1.0496	0.7399	0.6786	0.5075
5	0.5544	0.2449	0.2122	0.0974	0.8442	0.5347	0.5130	0.3871	0.8822	0.5726	0.5346	0.3891
6	0.3860	0.0766	0.1047	0.0638	0.4188	0.1094	0.1579	0.1111	0.4123	0.1029	0.1914	0.1764
7	0.5460	0.2365	0.1957	0.0733	0.7869	0.4774	0.4487	0.3147	0.8254	0.5159	0.4696	0.3156
8	0.3844	0.0751	0.0757	-0.0144	0.4062	0.0968	0.1093	0.0225	0.4056	0.0963	0.1084	0.0187
9	0.5349	0.2255	0.2354	0.2608	1.1590	0.8495	0.9054	0.8670	1.2056	0.8961	1.0406	1.0774
10	0.4993	0.1899	0.1546	0.0423	0.6206	0.3112	0.3003	0.1868	0.6220	0.3126	0.3067	0.1961
11	0.6263	0.3169	0.2517	0.1125	1.5021	1.1924	1.1638	1.0322	1.5649	1.2556	1.2281	1.0888
12	0.5055	0.1961	0.2289	0.1752	0.7301	0.4207	0.4609	0.4059	0.7504	0.4410	0.4801	0.4234
13	0.5615	0.2520	0.2056	0.0846	0.8403	0.5308	0.4986	0.3606	0.8797	0.5702	0.5220	0.3655
14	0.4437	0.1344	0.1522	0.0769	0.5193	0.2099	0.2381	0.1692	0.5191	0.2100	0.2384	0.1682
15	0.4819	0.1725	0.1403	0.0383	0.5770	0.2676	0.2627	0.1562	0.5764	0.2671	0.2753	0.1815
16	0.5615	0.2520	0.1951	0.0707	0.8427	0.5332	0.4972	0.3554	0.8571	0.5476	0.5167	0.3780
17	0.5587	0.2492	0.2227	0.1181	0.9484	0.6388	0.6149	0.4868	1.0105	0.7008	0.6596	0.5108
18	0.5260	0.2166	0.2487	0.2048	0.8882	0.5788	0.6220	0.5704	0.9155	0.6062	0.6957	0.6847
19	0.4735	0.1642	0.1675	0.0972	0.5791	0.2697	0.2940	0.2208	0.5899	0.2805	0.3012	0.2229
20	0.6403	0.3308	0.1800	0.0234	2.0474	1.7375	1.5010	1.1469	2.4009	2.0908	1.8041	1.3758
21	0.5796	0.2702	0.2597	0.2036	1.6397	1.3300	1.3676	1.3146	1.7652	1.4556	1.5587	1.5594
22	0.6248	0.3153	0.1867	0.0683	2.0158	1.7059	1.5339	1.2548	2.3772	2.0672	1.8501	1.5014
23	0.3238	0.0145	0.0577	0.0094	0.3335	0.0242	0.0789	0.0374	0.3333	0.0245	0.0919	0.0509
24	0.5476	0.2381	0.2573	0.2024	1.1439	0.8343	0.8621	0.7931	1.2275	0.9179	0.9394	0.8628
25	0.4962	0.1868	0.1733	0.1338	0.6579	0.3485	0.3803	0.3159	0.6622	0.3528	0.4258	0.3993
26	0.5519	0.2425	0.2289	0.1311	0.9082	0.5987	0.6099	0.5217	0.9134	0.6040	0.6201	0.5360
27	0.3430	0.0336	0.0648	0.0010	0.3569	0.0476	0.0827	0.0216	0.3584	0.0496	0.0887	0.0208
28	0.5294	0.2200	0.2269	0.1475	0.7983	0.4888	0.5089	0.4308	0.8252	0.5157	0.5299	0.4450
29	0.5684	0.2589	0.2015	0.0693	0.8744	0.5649	0.5181	0.3635	0.9185	0.6089	0.5423	0.3649
30	0.4024	0.0930	0.1128	0.0392	0.4411	0.1317	0.1588	0.0886	0.4427	0.1334	0.1591	0.0865
31	0.5089	0.1995	0.1661	0.0882	0.6603	0.3509	0.3584	0.2662	0.6714	0.3620	0.3628	0.2611
32	0.4418	0.1325	0.1269	0.0690	0.5106	0.2013	0.2249	0.1511	0.5192	0.2099	0.2329	0.1579
33	0.5155	0.2060	0.1979	0.1019	0.7022	0.3927	0.3967	0.3002	0.7242	0.4147	0.4075	0.2975
34	0.5496	0.2402	0.2847	0.2510	1.8199	1.5102	1.5625	1.5206	2.1075	1.7979	1.8836	1.8690
35	0.5550	0.2456	0.2890	0.2556	1.7303	1.4207	1.4811	1.4464	1.9056	1.5961	1.7094	1.7189

Table B7. Validation and Test response data at Monitoring Location #3, Table S9 provides the remainder of the datasets.